J-PARC 50-GeV PS Experimental Proposal

Measurement of T-violating Transverse Muon Polarization in $K^+ \to \pi^0\mu^+\nu$ Decays

K. Paton, R.E. Pywell and C. Rangacharyulu

Department of Physics, University Saskatchewan,
Saskatoon, Canada

M. Hasinoff

Department of Physics and Astronomy, University of British Columbia,
Vancouver, BC, Canada

P. Depommier

Laboratoire de Physique Nucléaire, Université
de Montréal, Canada

J. Doornbos

TRIUMF, Vancouver, Canada

K. Dow, D. Hasell, J. Kelsey, M. Kohl, R. Milner, M. Plesko,
F. Simon, S. Steadman and B. Surrow

MIT Laboratory for Nuclear Science and Bates Linear Accelerator Center.
Massachusetts Institute of Technology, Cambridge, Massachusetts, USA

S. Strauch and C.Djalali

Department of Physics and Astronomy, University of South Carolina,
Columbia, SC, USA

E.W. Anderson

Department of Physics, Iowa State University, Ames, Iowa, USA

K. Horie and S. Shimizu

Department of Physics, Osaka University, Osaka, Japan

T. Matsumura

National Defense Academy, Yokosuka, Japan

H. Yamazaki

Laboratory of Nuclear Science, Tohoku University, Sendai, Japan

Y. Igarashi, J. Imazato[1], G.Y. Lim, S. Sawada and H. Shimizu

High Energy Accelerator Research Organization (KEK), Tsukuba, Japan

April 28, 2006[2]

---

[1]Contact person

[2]Revision on August 4, 2006 after the submission to J-PARC

Abstract

As a precision-frontier experiment at J-PARC, we propose a search for time reversal invariance violation by measuring the transverse muon polarization in the $K^+ \rightarrow \pi^0 \mu^+ \nu$ decays of stopped K^+ mesons. The physics potential in terms of discovery of new physics along with the power to constrain the exotic models is shown to be competitive with other experiments being planned or prepared. A beamline of 0.8 GeV/c, as a branch off from the K1.1 beamline is designed. The detector system is an upgraded version of the KEK-PS E246 experiment. Major changes in the hardware are: i)improved charged particle tracking by incorporating the state-of-the-art GEM detectors, ii) new readout system of the CsI(Tl) calorimeter, iii) introducing active polarimeters for the muon decay positrons, and iv) a new magnet for the uniform muon field. This arrangement, with increased beam intensities ($\approx 3 \times 10^6$ kaons/sec) and a runtime of 10^7 seconds, will improve the E246 result by a factor of 20, bringing the discovery potential to $\delta P_T < 2 \times 10^{-4}$ in our quest for new physics.

Contents

1 Introduction

"..... one could have $P_T(\mu) \cong O(10^{-3})$ without violating any constraints inferred form ϵ_K, ϵ' and d_N! Since such a scenario is consistent with present phenomenology, it serves at least as a useful imagination stretcher– a commodity not to be belittled. For it illustrates that a detailed analysis of $K \rightarrow \mu\nu\pi$ could reveal a source of CP violation that would escape detection in $K \rightarrow 2\pi, 3\pi$. ...."

I.I. Bigi, A.I. Sanda, and N.G. Urlatsev [1]

Time reversal (T) symmetry has long been a subject of interest from pre-modern physics times, since it implies microscopic reversibility of motion - for instance, an identical trajectory of an object when time runs back in classical mechanics. In modern quantum field theories it has received renewed attention as a discrete symmetry of space/time along with charge conjugation (C) and parity reflection (P) [2]. Although C and P are each maximally violated in weak interactions, T (and CP) are almost exact symmetries in all the interactions including the weak interaction. The violation of T would have a great impact [3] since it would mean that the physics laws in the time-reversed world are different from ours.

The observation of CP violation in the neutral K^0 [5] meson and B^0 [6, 7] meson systems means that T should be also violated to the same extent according to the CPT theorem [8]. This theorem asserts that a Lorentz-invariant field theory should be invariant under the combined CPT operation and hence CPT is always conserved. Therefore, a number of experiments have long been performed in e.g. detailed balance tests in particle or nuclear reactions [9], searches for non-vanishing T-odd observables in decays [10], or searches for T-odd static properties such as electric dipole moments (EDM) of particles and atoms [11]. However, it was only recently that the first observation of T asymmetry was reported from the CPLEAR experiment of a Kabir test [12] in 1998. They found a slightly different time differential conversion rate between $K^0 \rightarrow \bar{K}^0$ and its time-reversed process $\bar{K}^0 \rightarrow K^0$ [13]. This discovery was followed by an observation of a large T-odd angular correlation asymmetry in $K_L \rightarrow \pi^+\pi^-e^+e^-$ in the KTeV experiment [14]. These two asymmetries in the neutral kaon system were the first direct observations, but are interpreted as relating to "indirect CP violation ϵ" of $K \rightarrow \pi\pi$ in terms of state mixing. As for the validity as the "direct observation" of T violation without relevant assumptions, some ambiguities have been pointed out [15].

The transverse muon polarization (P_T) in $K \rightarrow \pi\mu\nu$ ($K_{\mu3}$) with T-odd correlation was suggested by Sakurai [16] about 50 years ago to be a clear signature of T violation. Unlike other T-odd channels in e.g. nuclear beta decays, P_T in $K_{\mu3}$ has the advantage that the final state interactions (FSI), which may mimic T violation by inducing a spurious T-odd effect, are very small. This argument applies most particularly to $K_{\mu3}^+$ decay with only one charged particle in the final state where the FSI contribution is only from higher order loop levels and is calculable. Thus, it is not surprising that, over the last two decades, dedicated experiments have been carried out in search of non-zero P_T in $K_{\mu3}$ decays [17]. An important feature of a P_T study is the fact that the contribution to P_T from the Standard Model (SM) is nearly zero ($\sim 10^{-7}$). Therefore, in a P_T search we are investigating new physics beyond the SM. As is discussed below there are unique advantages in looking for CP violation in P_T.

The most recent research of P_T has been performed at KEK as the KEK-E246 experiment. This experiment was carried out by an international collaboration whose core members are also authors of the current proposal. The E246 result was consistent with no T violation but provided the world best limit of $P_T = -0.0017 \pm 0.0023 \; (stat) \pm 0.0017 \; (syst)$ [18] and constrained the parameter spaces of several contender models. It was, however, statistics limited, mainly due to insufficient accelerator beam intnsity in spite of smaller systematic errors.

Now we intend to continue the P_T experiment further at J-PARC where higher accelerator beam intensity will be available and a higher experimental sensitivity is promised, in order to search for new physics beyond SM. We aim for a sensitivity of $\delta P_T \sim 10^{-4}$.

In this proposal we first present some compelling theoretical reasons to search for CP violation beyond the SM and the meaning of P_T physics in Section 2. The $K_{\mu 3}$ decay and muon polarization formalism are summarized in Section 3 together with model descriptions of P_T. The proposed experimental arrangement is an upgrade of the setup employed in the KEK-E246 experiment. After reviewing the current experimental status in Section 4, we describe in detail the proposed experiment in Section 5 and the planned upgrades and improvements of each detector element in Section 6. The installation of a low-momentum beamline with a high quality kaon beam is proposed (Section 7). These detector upgrades will provide an improvement of the total systematic error down to the 10^{-4} level which is comparable to the expected statistical error. The detailed experimental procedure to ensure these accuracies is discussed in Section 8. Finally, in Section 9 we present the expected sensitivity of this experiment and the detailed methods we plan to use to control the systematics of the measurement.

2 Physics Motivation

2.1 P_T in the Standard Model

In order to formulate physics motivation for this experiment, we look first at what is predicted in the SM for P_T. A T-violating (or CP-violating) amplitude arises from the relative phases between diagrams or complex coupling constants in a diagram. Since only a single element of the CKM matrix V_{us} is involved for the W- exchanging semi-leptonic $K_{\mu 3}$ decay in the SM, no CP violation appears in the first order. As is discussed in [19] this is a general feature for vector (and axial vector) type interactions. The SM contribution comes from only higher order effects. The possible size of its contribution was once suggested qualitatively in [20] to be less than $P_T < 10^{-6}$. An actual value based on the lowest-order vertex radiative corrections to the $\bar{u}\gamma_\mu(1 - \gamma_5)sW^\mu$ vertex (Fig. 1) was presented in the textbook of Bigi and Sanda [2]. This has been estimated to be less than 10^{-7}. This fact constitutes the main motivation of the physics background for P_T experiment as a search for new physics. Since the effect arising from FSI is known to be of the order of 10^{-5} [52] and it is calculable as is shown below (in Section 3), an observation of a non-zero P_T implies unambiguously the existence of CP violation mechanisms beyond the SM, namely new physics. Assuming 10^{-6} for the ability for the FSI estimation, there is a large window to explore from the current limit of $P_T \sim 10^{-3}$, while several new physics models allow the appearance of P_T in the ranges of P_T $10^{-4} \sim 10^{-3}$ level at any time (Fig. 2). This situation
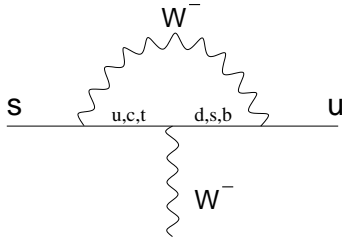
Figure 1: Radiative corrections in the $K_{\mu 3}$ decay which provides a Standard Model contribution to P_T [2].
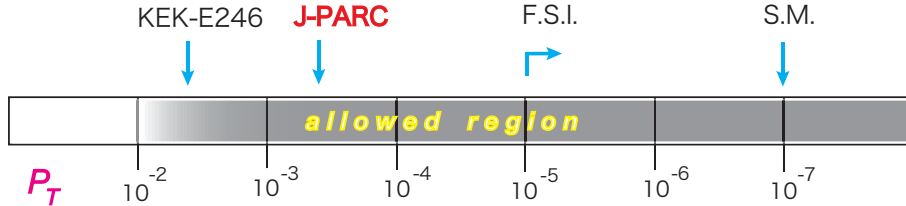
Figure 2: Experimental status of $K_{\mu 3}$ P_T physics relative to the SM prediction is illustrated. The experimental limits are in 90% confidence limits. "Allowed region" means that some of the non-SM CP violation models allow $P_T < 10^{-2} \sim 10^{-3}$ without conflicting with other experimental limits.

is very similar to the study of the neutron electric dipole moment (n-EDM) which is also a T-violation quantity, in which the current experimental limit of $d_n = 3.1 \times 10^{-26} e$ cm [21] is slowly approaching the SM prediction of $d_n \sim 10^{-31} e$ cm.

2.2 Need for CP violation beyond the Standard Model

The SM with three generations of quarks and leptons along with the three gauge interactions is an aesthetically appealing picture of physics, and it appears to be a very good effective theory at the electroweak scale. All of the observed phenomena including the processes of CP violation or flavor changing neutral currents are consistently explained by the quark flavor mixing CKM matrix. However, it has been argued that some theoretical aspects of the SM are simply unsatisfactory, since it is based on many arbitrary assumptions and it has too many parameters to be fine-tuned. It also cannot provide any rationale for why the fermions have the observed masses. The hierarchy problem associated with the electroweak symmetry breakdown strongly suggests that new physics should exist at the TeV mass scale. The presence of the dark matter in the universe, which is not explained by the SM particles, also suggests new particles. These theoretical considerations and possible new particles lead necessarily to new interactions or new physics beyond the SM - such as supersymmetric models (SUSY). Since new CP phases are in general associated with new interactions, new physics can reveal itself in CP violating processes, thus making CP violation studies extremely important along with direct observation of new particles at colliders.

A very strong argument for CP violation beyond the SM comes also from cosmology. The observed universe is almost entirely composed of matter, namely baryons, with no primordial antimatter, namely anti-baryons [22]. The present quantity η to characterize the baryon asymmetry of the universe (BAU) is estimated from the cosmological abundances of light elements and nucleosynthesis theories to be

$$\eta = \frac{n_B}{n_\gamma} = (4 \sim 7) \times 10^{-10} \tag{1}$$

where $n_B = n_b - n_{\bar{b}}$ (difference between the number densities of baryons and antibaryons) and n_γ is the photon number density. The standard cosmological model, however, can predict the equilibrium abundance of only $n_b/n_\gamma \sim n_{\bar{b}}/n_\gamma \sim 10^{-18}$ after the baryon anti-baryon annihilation process has frozen out if $\eta = 0$ is supposed at the Big-bang. Therefore, it seems that the universe has a fundamental asymmetry of matter-antimatter as a consequence of asymmetric interactions ("baryogenesis").

Sakharov [23] prescribed three necessary conditions to account for baryogenesis - (1) baryon number non-conservation, (2) C and CP violation, and (3) departure from thermal equilibrium. The amount of CP violation in the SM via the δ phase in the CKM matrix, however, falls short of this amount. Thus, many candidate scenarios of baryogenesis have been proposed in the literature [24, 25]. In the framework of the Grand Unified Theories, or supersymmetric models many possible sources of CP violation as well as B non-conservation are provided. Another candidate scenario is the so-called electroweak baryogenesis, in which Sakharov's criteria are implemented into the SM by typically requiring a first-order phase transition. It has been further suggested that baryogenesis may proceed also through leptogenesis [26] or in terms of the Affleck-Dine mechanism [27].

Thus, cosmology (or baryogenesis) certainly requires some new sources of CP violation and baryon number non-conservation. Hence, it is essential to look for their signature in laboratories and to find a candidate theory.

2.3   CP violation and physics of P_T

Today there are intensive studies underway at accelerator laboratories searching for CP violation beyond the SM. In addition to the direct search for new particles at high energy colliders, there are also many precision measurements to search for small deviations from the SM predictions. In B meson decays e.g. the observation of a slight difference between the CP asymmetry of the $B \rightarrow J/\psi K_S^0$ process and that of the penguin diagram processes [28] might be a hint for new physics. In the kaon sector, the CP violating $K_L \rightarrow \pi^0 \nu \bar{\nu}$ rare decay study is in progress at KEK [29] and this will also be proposed at J-PARC. It is attempted to measure possible difference of the unitarity triangle from that of the B physics, but it can only be achieved with sufficient event statistics. Considering the current situation of our understanding of CP violation, we believe that the importance of a P_T search is increasing. There are several important characteristics of P_T physics. They are briefly summarized as follows.

- If P_T is found at the level of 10^{-4} which cannot be explained as FST, it will correspond to direct "direct CP violation" in contrast to "indirect CP violation" due to the K_1^0-K_2^0 state mixing in the case of the K_0 system. The amount of direct CP violation in neutral kaons is found as the ratio $\varepsilon'/\varepsilon (\sim 1-^{-3})$ which is consistent

with SM predictions [30]. However, one should note that the agreement between the experiment and the theory, while good, still leaves large theoretical uncertainties. Therefore, the observation of CP violation in the charged kaon system is very much desired.

- Since the $K_{\mu 3}$ is a semi-leptonic process with W exchange in the SM resulting in a significant branching ratio, even a small amplitude of a new-physics diagram with large mass scale can contribute to P_T through interference with this W exchange process with a consequence of a relatively large effect. This is in strong contrast to new physics contribution to flavor changing neutral current rare decay processes in which the effect appears from loop diagrams. In terms of the effective Lagrangian, $P_T \sim 1/\Lambda^2$ with the mass scale Λ, while the direct detection of rare decays, such as $K_L^0 \to \pi^0 \nu \bar{\nu}$ should scale as $1/\Lambda^4$.

- Since the three Higgs doublet may allow a sizable value [31, 32], P_T can probe CP violation through the Higgs sector, of which very little is known with regards to the structure and dynamics [2]. There is no constraint even on the number of Higgs doublets so far inferred theoretically. Models with an extended Higgs sector with more than one SM Higgs doublet allow many new sources of CP violation.

- In general (even when the Higgs sector might not be relevant), P_T is sensitive to exotic scalar interactions as seen from the generic four fermion interaction Lagrangian (Eq. 15 below). P_T can determine the imaginary part of the scalar coupling coefficient $\mathrm{Im}(G_S^*)/G_F$ or set an upper limit in a most stringent manner. According to the recent analysis based on the effective Lagrangian, P_T scales as $P_T \sim 0.38 \, \mathrm{Im} C_S^K (\frac{\mathrm{TeV}}{\Lambda})^2$ [33] (here, C_S^K is the Wilson coefficient for the scalar interaction), making this mode a very sensitive probe of the large mass scale.

- There are several theoretical models which can accommodate a sizable P_T (within the reach of our experiment) without conflicting with other experimental constraints. Multi-Higgs doublet models, R-parity violating [34] or strong s-quark mixing [35]) SUSY models are among them. A P_T measurement offers more stringent constraints on the parameter spaces of these models. Descriptions of P_T in those models are briefly given in the next section.

- Once a non-zero P_T is observed in $K_{\mu 3}$, we can extend the study to other channels of kaon decays with a muon. Although these experiments with smaller branching ratio are more difficult, they will be feasible in the phase 2 operation of J-PARC with full intensity. The comparison of P_T with those observables will help discriminate among various models. P_T in $K^+ \to \mu^+ \nu \gamma$ is one typical example [36].

2.4   Relevance of a P_T experiment in the LHC era

Since the proposed experiment will yield the first result only after the start of LHC operation, it is necessary to ask whether the P_T result can still be meaningful in the presence of these other high energy data. The Super B Factory might also be in operation. Needless to say that such comparisons are model dependent and have only limited justification as a merely qualitative discussion.

- If LHC finds the charged Higgs boson, the P_T measurement will become even more important to look for associated CP violating couplings. It is expected that a MSSM Higgs boson should be discovered with 5σ significance after an integrated luminosity of 30/fb if the condition of $\tan\beta/m_{H+} \geq 0.06$ (GeV)$^{-1}$ is satisfied. If this limit is applied to the lightest charged Higgs boson in the context of the multi-Higgs model, the P_T corresponds to $|P_T| < 3 \times 10^{-4}$. This roughly corresponds to the aim of the proposed experiment of δP_T (one σ limit) $\sim 10^{-4}$.

- The deviation of the branching ratio of $B \to X\tau\nu$ from the SM estimate provides a constraint on a charged Higgs boson. Although the error of the branching ratio is still large, it will become more precise in the future e.g. at the Super B factory. A constraint of $\tan\beta/m_{H+} < 0.14$ (GeV)$^{-1}$ (90 % C.L.) after 5/ab of integrated luminosity can be expected. This again can be converted to P_T giving a corresponding limit of $|P_T| < 1.4 \times 10^{-3}$.

- A real competitor in the Super B Factory will be the same transverse polarization of τ leptons in $B \to D\tau\nu$. Rough estimate of its ratio to P_T^μ in $K_{\mu 3}$ is [37]

$$\frac{P_T^\tau}{P_T^\mu} \sim \frac{m_B m_\tau}{m_K m_\mu} \sim 10^2. \tag{2}$$

Although the τ production rate might be far lower, it may be feasible to extract P_T at the 10^{-2} level. Both data are complementary and be used to confirm the model. The exact comparison might lead to a favorable model.

2.5 Other experimental T-violation studies

A brief overview of the other experimental studies of T violation are worthwhile. Besides P_T, electric dipole moments (EDM) of particles or atoms are regarded as the most sensitive search for new physics at low energy. Intensive efforts over 6 decades of experimentation have pushed the EDM limit steadily down. The latest improved value of neutron EDM [21] of $d_n = 3.1 \times 10^{-26} e$ cm is compared to the SM prediction of $\sim 10^{-31} e$ cm. Bounds on the EDMs of other elementary particles such as the electron [39], muon [49], and neutrino [50] are also being lowered. Measurements of atomic EDMs, for example that of Hg^{199} [40], are being carried out with the present-day results being consistent with zero. As for d_n the next generation experiments are now being prepared [41] aiming at $10^{-28} e$ cm. We can anticipate further improvements in the EDM measurements, constraining the model parameter space and/or discovering new physics. While the current experiment of P_T also searches for new physics, the parameter space spanned by these experiments are complementary (as is discussed e.g. in multi-Higgs models). The neutron and atomic EDMs are also related to $\bar{\theta}_{\text{QCD}}$ which is not relevant in P_T.

Several T-odd correlation experiments have been carried out at both low energies and higher energies. Recent T-odd beta decay parameter measurements yielded $D = [-2.8 \pm 6.4(stat) \pm 3.0(syst)] \times 10^{-4}$ for the neutron decay [42], and $R = (0.9 \pm 2.2) \times 10^{-3}$ for the ^{8}Li decay [43]. Also the recent measurement of transverse e^+ polarization with T-odd character in polarized μ^+ decay gives no T violation $P_{T_2} = (3.7 \pm 7.7 \pm 3.4) \times 10^{-3}$ [44]. They are all consistent with zero value with no hint of T violation. The nuclear beta decay

physics analysis is complicated by the large final state interactions, and the nuclear-model dependence of the complex many-body nuclear wave functions.

A very promising channel for T violation in high energy experiments is the EDM of the τ lepton. Due to the larger mass compared with muons an enhanced effect is expected, which could be $d_\tau \sim 10^{-19} e$ cm in some new physics models. The measured observables are the spin correlations in τ-pair production in e^+e^- colliders. The recent result from KEK-B Belle was $\text{Re}(d_\tau) = (1.15 \pm 1.70) \times 10^{-17} e$ cm and $\text{Im}(d_\tau) = (-0.83 \pm 0.86) \times 10^{-17} e$ cm [45]. As for P_T in semi-leptonic B meson decays, there are several theoretical papers [37, 46] predicting significantly large values (see the previous discussion on the mass dependence), but so far no experimental result has been presented.

3 $K_{\mu3}$ decay and transverse muon polarization

3.1 Phenomenology of $K_{\mu3}^+$ decay

In this section the phenomenology of the $K_{\mu3}$ decay is briefly introduced. The decay matrix element based on the V-A theory can be written as [47, 48]

$$M = \frac{G_F}{2}\sin\theta_c \Big[f_+(q^2)(p_K^\lambda + p_\pi^\lambda) + f_-(q^2)(p_K^\lambda - p_\pi^\lambda) \Big] \cdot \Big[\overline{u}_\nu \gamma_\lambda (1 - \gamma_5) v_\mu \Big]. \tag{3}$$

with two form factors $f_+(q^2)$ and $f_-(q^2)$ of the momentum transfer squared to the lepton pair, $q^2 = (p_K - p_\pi)^2$. Here, G_F is the Fermi constant, θ_c the Cabibbo angle, p_K, p_π, p_μ and p_ν are the four-momenta of the kaon, pion, muon and antineutrino, respectively. Using $p_K = p_\pi + p_\mu + p_\nu$, this amplitude can be rewritten as

$$M = \frac{G_F}{2}\sin\theta_c f_+(q^2) \Big[2p_K^\lambda \cdot \overline{u}_\nu \gamma_\lambda (1 - \gamma_5) v_\mu + (\xi(q^2) - 1)m_\mu \overline{u}_\nu (1 - \gamma_5) v_\mu \Big]. \tag{4}$$

where the parameter $\xi(q^2)$ is defined as

$$\xi(q^2) = f_-(q^2)/f_+(q^2). \tag{5}$$

The first term of Eq.4 corresponds to the vector (and axial vector) amplitude, and the second term corresponds to the scalar (and pseudoscalar) amplitude. The parameters f_- and f_+ depend on q^2 as

$$f_\pm(q^2) = f_\pm(0)\Big[1 + \lambda_\pm(q^2/m_\pi^2) \Big], \tag{6}$$

Both f_+ and f_- can, in general, be complex. If time reversal (T) is a good symmetry, the parameter ξ is real. Any non-zero value of $\text{Im}\xi$ would imply T violation. As we show below, an experimentally observed T-violating muon polarization P_T is directly proportional to $\text{Im}\xi$. The currently adopted values [48] are $\lambda_+ = 0.0284 \pm 0.0027$, $\xi(0) = -0.14 \pm 0.05$, and $\lambda_- = 0$. The Dalitz distribution for $K_{\mu3}$ decay is given by [48]

$$\rho(E_\pi, E_\mu) \propto f_+^2(q^2)\Big[A + B\xi(q^2) + C\xi^2(q^2) \Big], \tag{7}$$

11
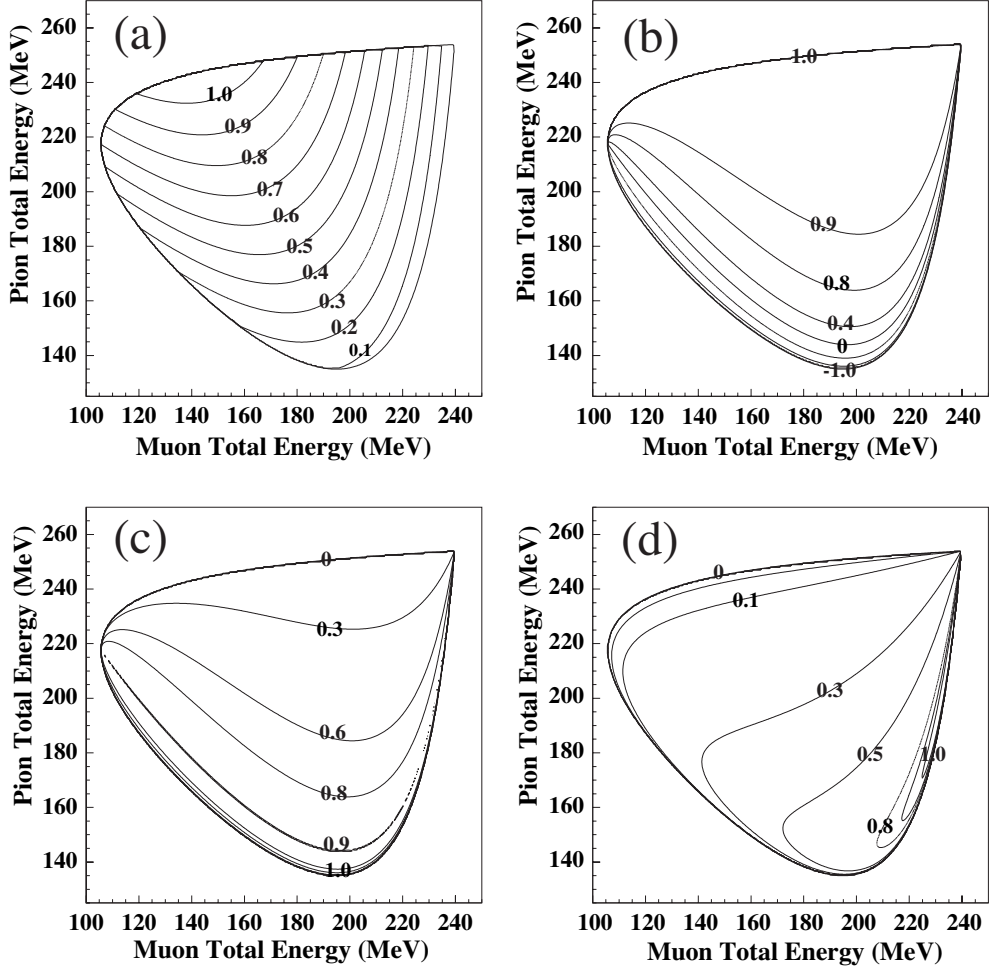
Figure 3: The intensity distribution (a), and the three components of the muon polarizations: (b) the longitudinal component P_L, (c) the normal component P_N, and (d) the transverse component $P_T/\mathrm{Im}\xi$.

with

$$A = m_K(2E_\mu E_\nu - m_K E'_\pi) + m_\mu^2(\frac{1}{4}E'_\pi - E_\nu) \tag{8a}$$

$$B = m_\mu^2(E_\nu - \frac{1}{2}E'_\pi) \tag{8b}$$

$$C = \frac{1}{4}m_\mu^2 E'_\pi \tag{8c}$$

$$E'_\pi = (m_K^2 + m_\pi^2 - m_\mu^2)/(2m_K) - E_\pi. \tag{8d}$$

Here, E_π, E_μ and E_ν are the energies of the pion, muon and neutrino in the kaon center-of-mass frame, and M_K, m_π and m_μ the masses of the kaon, pion and muon, respectively. M_K is the kaon-mass. The Dalitz plot is shown in Fig. 3a.

3.2 Transverse polarization P_T

In three body decays such as $K_{\mu 3}$, one defines three orthogonal components of the muon polarization vector: the longitudinal (P_L), normal (P_N) and transverse (P_T) as the components parallel to the muon momentum $\vec{p}_\mu$, normal to P_L in the decay plane, and normal to the decay plane, respectively. They are scalar products of the polarization vector ($\vec{\sigma}_\mu$) with three corresponding combinations of the unit momentum vector as expressed below:

$$P_L = \frac{\vec{\sigma}_\mu \cdot \vec{p}_\mu}{|\vec{p}_\mu|}, \tag{9a}$$

$$P_N = \frac{\vec{\sigma}_\mu \cdot (\vec{p}_\mu \times (\vec{p}_\pi \times \vec{p}_\mu))}{|\vec{p}_\mu \times (\vec{p}_\pi \times \vec{p}_\mu)|}, \tag{9b}$$

$$P_T = \frac{\vec{\sigma}_\mu \cdot (\vec{p}_\pi \times \vec{p}_\mu)}{|\vec{p}_\pi \times \vec{p}_\mu|}. \tag{9c}$$

As can be seen, the P_T changes sign under the time reversal operation, thus making it a T-odd observable. Using the decay probability (Eq. 7) one can write the muon polarization in the kaon rest frame as [47,48]

$$\vec{\sigma}_\mu = \vec{P}/|\vec{P}|, \tag{10}$$

where $\vec{P}$ is determined as follows

$$\vec{P} = \left\{ a_1(\xi) - a_2(\xi)[(m_K - E_\pi) + (E_\mu - m_\mu)(\vec{p}_\pi \cdot \vec{p}_\mu)/|\vec{p}_\mu|^2] \right\} \vec{p}_\mu$$
$$- a_2(\xi)m_\mu \vec{p}_\pi + m_K m_\mu \text{Im}(\xi)(\vec{p}_\pi \times \vec{p}_\mu). \tag{11}$$

with

$$a_1(\xi) = 2m_K^2 \left[E_\nu + \text{Re}(b(q^2))(E_\pi^* - E_\pi) \right], \tag{12a}$$

$$a_2(\xi) = m_K^2 + 2\text{Re}(b(q^2))m_K E_\mu + |b(q^2)|^2 m_\mu^2, \tag{12b}$$

$$b(q^2) = \frac{1}{2}[\xi(q^2) - 1], \quad \text{and} \tag{12c}$$

$$E_\pi^* = (m_K^2 + m_\pi^2 - m_\mu^2)/(2m_K). \tag{12d}$$

These three polarization components are shown in Fig. 3b-d. One has to look for P_T in the presence of the predominant in-plane component of the polarizations, P_L and P_N. P_T (Eq. 9c) can be further rewritten in terms of Imξ and a kinematical factor as

$$P_T = \text{Im}\xi \cdot \frac{m_\mu}{m_K} \frac{|\vec{p}_\mu|}{[E_\mu + |\vec{p}_\mu|\vec{n}_\mu \cdot \vec{n}_\nu - m_\mu^2/m_K]}. \tag{13}$$

The quantity Imξ, sensitive to the T-violation, can be determined from a P_T measurement. The advantage of $K_{\mu 3}$ over K_{e3} ($K^+ \rightarrow \pi^0 e^+ \nu$) is apparent as P_T is proportional to the lepton mass. The kinematic factor as a function of the π^0 energy ($2E_{\pi^0}/m_K$) and μ^+ energy ($2E_{\mu^+}/m_K$) is the contour shown in Fig. 3d which has an average value of ~ 0.3 yielding a full detector acceptance relation of

$$< P_T > \sim 0.3 \, \text{Im}\xi. \tag{14}$$

13

It is of interest to establish the connection between the $\text{Im}\xi$ and effective parameters of new physics appearing in the coefficients of generic exotic interactions. To this end, an effective four fermion Lagrangian can be used:

$$
\begin{aligned}
L = \quad & - \quad \frac{G_F}{\sqrt{2}} \sin\theta_C \, \bar{s}\gamma_\alpha(1-\gamma_5)u \, \bar{\nu}\gamma^\alpha(1-\gamma_5)\mu \\
& + \quad G_S \, \bar{s}u \, \bar{\nu}(1+\gamma_5)\mu + G_P \, \bar{s}\gamma_5 u \, \bar{\nu}(1+\gamma_5)\mu \\
& + \quad G_V \, \bar{s}\gamma_\alpha u \, \bar{\nu}\gamma^\alpha(1-\gamma_5)\mu + G_A \, \bar{s}\gamma_\alpha\gamma_5 u \, \bar{\nu}\gamma^\alpha(1-\gamma_5)\mu + \text{h.c.}.
\end{aligned}
\tag{15}
$$

Here, G_S and G_P are the scalar and pseudo-scalar coupling constants and G_V and G_A are the exotic vector and axial-vector coupling constants, respectively. Tensor interactions are neglected. $\text{Im}\xi$ is found to be caused only by the interference between the SM term and the scalar term, namely by the complex phase of G_S [36,37], which can be written as

$$
\text{Im}\xi = \frac{(m_K^2 - m_\pi^2)\text{Im}G_S^*}{\sqrt{2}(m_s - m_u)m_\mu G_F \sin\theta_C}
\tag{16}
$$

where m_s and m_u are the masses of the s-quark and u-quark, respectively. Thus, P_T can constrain the exotic scalar interactions.

3.3 Final state interactions

Strictly speaking, a measured non-zero value of a T-odd observable does not automatically mean T violation. P_T^{FSI} can be induced by final-state interactions (FSI). This has been a concern in P_T experiments for quite some time. In the case of $K_{\mu 3}$ decays, the FSI are mainly due to electromagnetic interactions. Since the FSI contributions to P_T in the present case are much smaller than those in $K_{\mu 3}^0$ decay, which has two charged particles interacting in the final state and $P_T^{FSI}(K_{\mu 3}^0) \sim 10^{-3}$, the FSI in $K_{\mu 3}^+$ has been extensively investigated. The single-photon contribution to P_T^{FSI} in this decay is due to the imaginary part of the two-loop diagrams. An example is shown in Fig. 4a. It was estimated more than 20 years ago to be $P_T^{FSI} \leq 10^{-6}$ [51]. Quite recently two-photon exchange contributions to P_T^{em} have been studied in Ref. [52], where the transverse polarization is proportional to the imaginary parts of the diagrams shown in Fig. 4b. The value of P_T^{em} averaged over the Dalitz plot was deduced to be less than 10^{-5}. Thus, a non-zero P_T in the range of $10^{-3} \sim 10^{-4}$ will constitute a clear signal of a new physics contribution.

3.4 Theoretical model descriptions of P_T

In this section we briefly describe several models which might lead to a sizable P_T value. We also give a more general discussion based on the effective field theory to clarify the difference of P_T physics from other T and CP violating observables.

3.4.1 Multi-Higgs doublet model

As the minimum and natural extension of the SM with one Higgs doublet, multi-Higgs doublet models have been considered, and a number of papers [31,32,38] have applied this model to P_T as one of the promising candidate theories. In the class of models without tree-level flavor changing neutral current, new CP violating phases are introduced in the
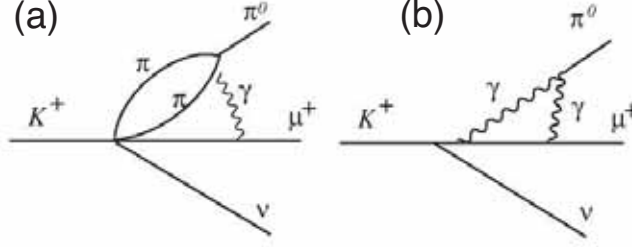
Figure 4: (a) One of the diagrams of the final state interactions contributing to P_T^{FSI}; from one photon exchange calculated in [51] and also (b) one of the diagrams from two photon exchanges calculated in [52].

charged Higgs mass matrix if the number of doublets is more than two. The coupling of quarks and leptons to the Higgs boson is expressed in terms of the Lagrangian [31, 32]

$$L = (2\sqrt{2}G_F)^{\frac{1}{2}} \sum_{i=1}^{2} \{\alpha_i \bar{u}_L V M_D d_R H_i^+ + \beta_i \bar{u}_R M_U V d_L H_i^+ + \gamma_i \bar{\nu}_L M_E e_R H_i^+\} + \text{h.c.}, \quad (17)$$

where M_D, M_U, M_E are diagonal mass matrces, V is the CKM matrix, and α_i, β_i and γ_i are the new complex coupling constants associated with the charged Higgs interactions. For the three doublet case a natural flavor conservation can be arranged. In this model CP symmetry can also be broken spontaneously due to complex phases of the vacuum expectation values of the Higgs fields. The coefficients, α_i, β_i and γ_i can have complex phases, and P_T is calculated as

$$\text{Im}\xi = \frac{m_K^2}{m_H^2}\text{Im}(\gamma_1 \alpha_1^*) \quad (18)$$

where α_1 and γ_1 are the quark and lepton couplings to the lightest charged Higgs boson. The E246 result [71] yielded $|\text{Im}(\gamma_1 \alpha_1^*)| < 544(m_H/\text{GeV})^2$ as the most stringent limit for this parameter. It is also constrained by the semileptonic decay of the B meson [55], $B \to \tau\nu X$ but the result is less stringent than the P_T constraint. Regarding the recent result of $B \to \tau\nu$ [54], its impact on this model in now being checked. Other constraints to this model come from the neutron EDM (d_n), $b \to s\gamma$ [55] and $b \to sl\bar{l}$ [56] complementing the P_T result in a different manner, since these channels limit $\text{Im}(\alpha_1\beta_1^*)$. These two parameters are related as $\text{Im}(\alpha_1\beta_1^*) = -(v_3/v_2)^2\text{Im}(\gamma_1\alpha_1^*)$ through the ratio of the vacuum expectation values v_2 and v_3. An interesting scenario assumed in [31] is $v_3/v_2 \sim m_\tau/m_t \sim$

1/80 thus making P_T the most sensitive test of the three Higgs doublet model over d_n and $b \to s\gamma$. The important feature of this model is the prediction of P_T in the radiative decay $K^+ \to \mu^+ \nu \gamma$ $(K_{\mu\nu\gamma})$. The following expression was obtained [36],

$$P_T(K_{\mu\nu\gamma}) \cong -0.1 \frac{m_K^2}{m_H^2} \text{Im}(\gamma_1 \alpha_1^*), \tag{19}$$

with the same sign as $P_T(K_{\mu 3})$ but with different size. E246 provided a result [57], however it lacked good statistics. Although the final state interaction is large and on the order of 10^{-3} we may pursue this mode also at J-PARC in the future.

3.4.2 SUSY models

A number of other models also allow P_T at observable level without conflicting with other experimental constraints. In other words, non-observation of P_T can constrain those models. Some models of Minimal Super-symmetric Standard Models (MSSM) allow sizable values. One interesting case is the model discussed by G.-H. Wu and J.N. Ng [35]. In this model the complex coupling constant between the charged Higgs boson and strange- and up-quarks is induced through squark and gluino loops. Then, the P_T value when the muon and neutrino momenta are at right angles, is given as

$$P_T^{H^+} \approx 3.5 \times 10^{-3} I_{H^+} \frac{p_\mu}{E_\mu} \frac{(\mu + A_t \cot \beta)}{m_g}$$
$$\frac{(100 \text{ GeV})^2}{M_H^2} \frac{\text{Im}[V_{33}^{H^+} V_{32}^{D_L^*} V_{31}^{U_R^*}]}{\sin \theta_c}. \tag{20}$$

for $\tan \beta \approx 50$. (For the meanings of various symbols see Ref. [35] except to note that we assumed the top quark mass to be 180 GeV.) If we allow large flavor mixing coupling in the squark-quark vertices, there is an allowed parameter region for large P_T. The E246 P_T upper bound corresponds to $M_H > 140$ GeV. In view of several assumptions made, this bound should be considered as a qualitative estimate [34]. It is noteworthy that $P_T(K_{\mu 3})$ and $P_T(K_{\mu\nu\gamma})$ have opposite signs in this model.

Another interesting SUSY model is the R-parity violating one [34]. In this model the interactions are described by the Lagrangian using the λ_{ijk}, λ'_{ijk} and λ''_{ijk} coefficients of the super potential as

$$L = \frac{1}{2}\lambda_{ijk}[\bar{\nu}_{L_i}^c e_{L_j} \tilde{e}_{R_k}^* + \bar{e}_{R_k} \nu_{L_i} \tilde{e}_{L_j} - (i \leftrightarrow j)]$$
$$+ \lambda'_{ijk}[\bar{\nu}_{L_i}^c d_{L_i} \tilde{d}_{R_k}^* + \bar{d}_{R_k} \nu_{L_i} \tilde{d}_{R_j} + \bar{d}_{R_k} d_{L_j} \tilde{\nu}_{L_i}$$
$$- \bar{e}_{R_i}^c u_{L_j} \tilde{d}_{R_k}^* - \bar{d}_{R_k} e_{L_i} \tilde{u}_{L_j} - \bar{d}_{R_k} u_{L_j} \tilde{e}_{L_i}] \tag{21}$$

by assuming $\lambda''_{ijk} = 0$ because of the non-observation of proton decays. Here the subscripts $i(k)$ are the slepton (squark) family indices. There are two kinds of contributions to P_T; one is from slepton exchange and the other is from down-type squark exchange. They are given, respectively as

$$\text{Im}\xi^l = \sum_i \frac{\text{Im}[\lambda_{2i2}(\lambda'_{i12})^*]}{4\sqrt{2}G_F \sin \theta_c (m_{\tilde{l}_i)^2}} \cdot \frac{m_K^2}{m_\mu m_s} \tag{22a}$$

16

$$\mathrm{Im}\xi^d \;=\; \sum_i \frac{\mathrm{Im}[\lambda'_{21k}(\lambda'_{22k})^*]}{4\sqrt{2}G_F \sin\theta_c (m_{\tilde{d}_k})^2} \cdot \frac{m_K^2}{m_\mu m_s}. \tag{22b}$$

Thus, the parameters of $\mathrm{Im}[\lambda_{2i2}(\lambda'_{i12})^*]/m^2$ and $\mathrm{Im}[\lambda'_{21k}(\lambda'_{22k})^*]/m^2$ are constrained. There are many experimental constraints for λ_{ijk} and λ'_{ijk} [58], but for the relevant four combinations of $\lambda(\lambda')^*$ and $\lambda'(\lambda')^*$ the constraints from other experimental limits are not stringent enough, thus P_T determines their limits as a function of their mass scale m.

3.4.3 Effective operator analysis

In a recent paper [33] Chang and Ng analyzed P_T in terms of effective field theory. In this theory the effective Lagrangian is a sum of the SM term and non- renormalizable ones resulting from integrating out the unknown degrees of freedom of new physics above a cut-off scale Λ. Then the operators are expanded by their dimensions and the higher dimensional ones are suppressed by higher powers of Λ, such as $L^{eff} = L_{SM} + L_5/\Lambda' + L_6/\Lambda^2 + \cdots$. The operators relevant to our new physics studies are the dimension 6 operators L_6, and the charged-current terms at the electroweak scale in the mass eigen-basis are

$$\begin{aligned}
-L_6^{CC} \;=\;\; & C'_{V_2}(\bar{u}^i\gamma^\mu \hat{L}d^i)(\bar{e}^i\gamma_\mu \hat{L}\nu^i) + C_{S_1}^{ij.kl}(\bar{u}^i\hat{R}d^j)(\bar{e}^k\hat{L}\nu^l) \\
& - C_{S_2}^{ij.kl}(\bar{d}^i\hat{R}u^j)(\bar{\nu}^k\hat{R}e^l) - C_T^{ij.kl}(\bar{d}^i\sigma^{\mu\nu}\hat{R}u^j)(\bar{\nu}^k\sigma_{\mu\nu}\hat{R}e^l) + \text{h.c.} \tag{23}
\end{aligned}$$

Here, C_V, C_S and C_T are the Wilson coefficients for the vector, scalar and tensor terms. Since they are in general complex, they can give rise to novel CP violation effects via interference with a SM amplitude from L_{SM}. P_T is

$$\vec{P_T} \sim \left[0.38\,\mathrm{Im}C_S^K - 0.27\,\frac{p_K\cdot(p_\nu - p_\mu) + m_\mu^2/2}{M_K^2(f_+/f_T)}\,\mathrm{Im}C_T^K \right] \left(\frac{\mathrm{TeV}}{\Lambda}\right)^2 \frac{\vec{p_\mu}\times\vec{p_\nu}}{\Phi}, \tag{24}$$

thus making it clear that scalar and tensor interactions are responsible for P_T. The second term in the bracket shows that the tensor term has a peculiar kinematical dependence, namely it is largest for large $E_\mu - E_\nu$. The E246 result yields

$$|\mathrm{Im}C_S^K|,\; |\mathrm{Im}C_T^K| \leq 2\times 10^{-3}(\Lambda/\mathrm{TeV})^2 \tag{25}$$

corresponding to the 90% confidence limit assuming that $f_T \sim f_+$.

4 Experimental status

4.1 History of $K_{\mu3}$ P_T experiments

The measurement of P_T in $K_{\mu3}$ decays has a long history. Early measurements of P_T were carried out at the Bevatron [59] and Argonne [60] in $K_{\mu3}^0$ decays but they lacked statistical significance. More advanced experiments prior to our work were done at the 28 GeV AGS at the Brookhaven National Laboratory (BNL). Morse *et al.* [61] measured P_T of muons from in-flight decay of $K_{\mu3}^0$. From a data sample of 12 million events, they deduced $\mathrm{Im}\xi = 0.009 \pm 0.030$. This result, while consistent with zero, has a central value compatible with a prediction of 0.008, from the T conserving final state interactions. As mentioned above, the final state interactions in $K_{\mu3}^0$ decays obscure the real value of P_T.

Table 1: Previous experiments and their Imξ results

Laboratory	Decay	Year	Imξ	Ref.
Bevatron	$K^0_{\mu3}$	1967	-0.02 ± 0.08	[59]
Argonne	$K^0_{\mu3}$	1973	-0.085 ± 0.064	[60]
BNL-AGS	$K^0_{\mu3}$	1980	0.009 ± 0.030	[61]
BNL-AGS	$K^+_{\mu3}$	1983	-0.016 ± 0.025	[17]
KEK-PS	$K^+_{\mu3}$	2004	-0.005 ± 0.008	[18]

Table 2: Experimental condition of E246

Parameter	Value	Expectation at J-PARC
K^+ beamline	K5 with 660 MeV/c	K0.8 with 800 MeV/c
Proton intensity	1.0×10^{12}/s	0.54×10^{14}/s
K^+ beam intensity	1.0×10^5/s	3×10^6/s
π/K ratio	~ 8	< 0.5
Beam duty factor	$0.7\,\mathrm{s}/2.0\,\mathrm{s}^3$	$> 0.7\,\mathrm{s}/3.5\,\mathrm{s}$
Net run time	~ 5200 hours (1.8×10^7s)	1.0×10^7s

At the same facility, Blatt *et al.* [17] measured P_T of $K^+_{\mu3}$ for the first time by detecting neutral particles from the in-flight decay of an unseparated 4 GeV/c K^+ beam. From a data sample of 21 million events, they deduced Im$\xi = -0.016 \pm 0.025$, consistent with T invariance. The most recent result was from the KEK-PS E246 experiment, on which the current proposal is based. The details of this experiment are presented in the next section. Table 1 presents the world data as of today.

4.2 KEK E246 Experiment: Results and limitations

The most recent and highest precision experiment was performed at the KEK proton synchrotron. Several authors of the current proposal were members of this collaboration. The experiment used the stopped K^+ beam at the K5 low-momentum beam channel [62] with the Superconducting Toroidal Spectrometer [63] setup (Fig. 7). An elaborate detector consisting of a large-acceptance CsI(Tl) barrel, tracking chambers, an active target and muon polarimeters were constructed and the data were taken between 1996 and 2000 for a total of 650 shifts (5200 hours) of beam time. A precise field mapping was made [64] before the measurements. Since K5 was equipped only with a single electrostatic separator stage, the channel provided a beam with substantial π^+ contamination with a π/K ratio of about 8 for a 660 MeV/c beam. (At J-PARC we expect $\pi/K < 0.5$.) The performance of the CsI(Tl) calorimeter was limited by this π^+ contamination with a halo resulting in accidental hits. The relatively low K^+ intensity of typically 10^5/s was a consequence of the maximum available proton beam intensity of 10^{12}/s from the slow extraction of the accelerator. The main parameters of the experiment are summarized in Table 2. Current estimates of these parameters at J-PARC are also shown.

The details of the detector have already been presented in [65] and they will not be repeated here. Also, some individual elements have been documented in the literature,

e.g. the CsI(Tl) calorimeter [66], its readout electronics [67], and the target ring counter system [68]. The features of the $K_{\mu3}$ detection are 1) μ^+ (charged particle) detection by means of a tracking system with 3 MWPC and a fiber bundle target with the momentum analysis by the Toroidal Spectrometer, and 2) π^0 detection as two photons or one photon with relatively large energy by the CsI(Tl) calorimeter. The muon polarization measurement relied on the sensitivity of the decay positron emission asymmetries in a longitudinal magnetic field with $< \mathbf{B} > \parallel \vec{P_T}$ using "passive polarimeters", where $< \mathbf{B}$ is the average of muon magnetic field vectror. The total acceptance of the detector for $K_{\mu3}$ when a π^0 was detected as two photons is shown in Fig. 5 calculated in a Monte Carlo simulation compared with the figure of merit $A\sqrt{N}$ distribution on the Dalitz plane. The measurements ran smoothly with a few months of beam time each year for over four years. Two independent teams separately carried out careful data analyses and the two results were combined at the end. Thanks to the stopped beam method which enabled a so-called forward (fwd) and backward (bwd) symmetric measurement with regard to the π^0 emission direction, and the high rotational symmetric structure of the toroidal spectrometer system, the systematic errors could be substantially suppressed. The analysis was done essentially in the following scheme, although a weighted analysis regarding the muon stopping position was adopted in a detailed analysis. The T-odd asymmetry was deduced as

$$A_T = (A_{fwd} - A_{bwd})/2 \tag{26}$$

where the fwd and bwd asymmetries were calculated using the "clockwise" and "counterclockwise" positron emission rate N_{cw} and N_{ccw} (red arrows and green arrows in Fig. **??**(left), respectively) as

$$A_{fwd(bwd)} = \frac{N_{fwd(bwd)}^{cw} - N_{fwd(bwd)}^{ccw}}{N_{fwd(bwd)}^{cw} + N_{fwd(bwd)}^{ccw}}. \tag{27}$$

Then, P_T was deduce using the analyzing power α and the average kinematic attenuation factor $< \cos\theta_T >$ to be

$$P_T = A_T/\alpha < \cos\theta_T > . \tag{28}$$

The first result was reported in 1999 [70] and the final result in 2004 [18]. A full description of the experiment is contained in reference [71].

The final result was

$$P_T = -0.0017 \pm 0.0023\,(stat) \pm 0.0011\,(syst) \tag{29a}$$
$$\mathrm{Im}\xi = -0.0053 \pm 0.0071\,(stat) \pm 0.0036\,(syst) \tag{29b}$$

corresponding to the upper limits of $|P_T| < 0.0050\,(90\%\,C.L.)$ and $|\mathrm{Im}\xi| < 0.016\,(90\%\,C.L.)$, respectively. This was a factor of 3 improvement over the previous BNL experiment. The progress of the $K_{\mu3}$ P_T results over the last forty years is shown in Fig. 6. The result of the E246 experiment constrains the three-Higgs doublet model parameter to be $|\mathrm{Im}(\alpha_1\gamma_1^*)| < 544(M_{H_1}/\mathrm{GeV})^2$ as the most stringent constraint of the model. Other theoretical implications of this result were discussed in [71]. The E246 result was statistics limited, i.e. the total systematic error was less than half of the statistical error. Table 3 lists the contributions from the various sources of systematic errors. A remarkable point here is that most of the systematic error sources cancelled out after the 12-gap summation due to the rotational symmetry of the system and the fwd-bwd ratio due to its symmetry.
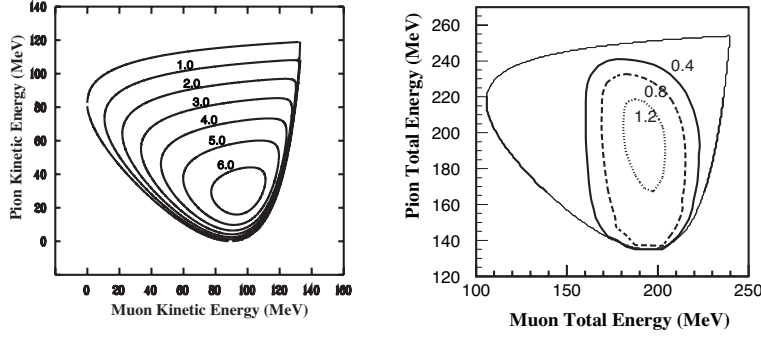
Figure 5: Acceptance contour of the detector for $K_{\mu 3}$ when a π^0 is detected as two photons (right) compared with the FoM $(= A\sqrt{N})$ distribution without the detector. The acceptance characteristics are same for the proposed J-PARC experiment.
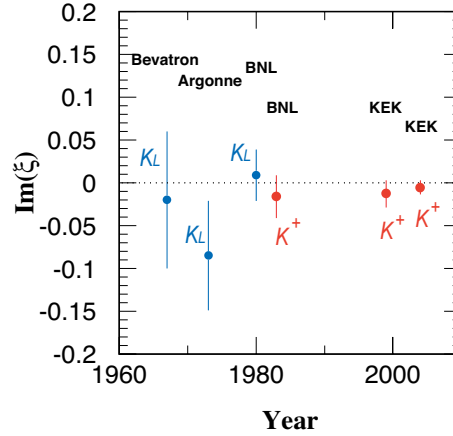
Figure 6: History of $K_{\mu 3}$ P_T experiments with their results for K_L^0 as well as K^+.

The largest error in the table is the effect of multiple scattering of muons through the Cu degrader of the polarimeter[4]. The J-PARC experiment, the subject of the current proposal, will be free from this error as we will employ an active polarimeter (see below). There were two items which were not cancelled out by any of the two cancellation mechanisms, the effect from the decay plane rotation, θ_z and the rotation of the muon magnetic field, δ_z, which will remain as the most serious errors in the J-PARC experiment.

4.3 Status at other laboratories

There is no immediate serious competition for this experiment. The proposals by us and also another Brookhaven National Laboratory group at the now defunct AGS were highly rated in 1998 for both scientific and technical aspects as E936 [72] and E923 [73], respectively. However, these projects were not realized due to the policy of the BNL

---

[4]This multiple scattering effect is essentially statistical in nature, but it was included in the systematic errors since it contributes to an error in muon stopping positions.

Table 3: Summary of major systematic errors. The cancellation capabilities of the 12-gap summation and *fwd-bwd* subtraction are shown. There are two systematics which are not cancelled by any of them, i.e. magnetic field rotation and decay plane rotation about the z axis. The result is in principle correctable for those δP_Ts, but are treated here as systematic errors. In the proposed J-PARC experiment, related systematic errors arise from the errors of the corrections. The largest error of μ^+ multiple scattering is irrelevant in the J-PARC experiment.

	Canceled by		
Source	Σ_{12}	fwd/bwd	$\delta P_T \times 10^4$
e^+ counter r-rotation	yes	yes	0.5
e^+ counter z-rotation	yes	yes	0.2
e^+ counter ϕ-offset	no	yes	2.8
e^+ counter r-offset	yes	yes	< 0.1
e^+ counter z-offset	yes	yes	< 0.1
$\vec{B}$ offset (ϵ)	no	yes	3.0
$\vec{B}$ rotation (δ_r)	no	yes	0.37
$\vec{B}$ rotation (δ_z)	no	no	5.3
μ^+ counter y-offset	no	yes	< 0.1
CsI(Tl) misalignment	yes	yes	1.6
K^+ stop distribution	yes	yes	< 3.0
MWPC y-offset (C4)	no	yes	2.0
K^+-dif background	yes	no	< 1.9
$K_{\pi 2}$-dif background	no	yes	0.6
μ^+ multiple scattering	yes	no	7.1
e^+ time spectrum	no	yes	0.8
Decay plane angle (θ_r)	no	yes	1.2
Decay plane angle (θ_z)	no	no	0.66
Uncertainty of α	-	-	1.3
$< \cos \theta_T >$ uncertainty	-	-	3.3
P_T gradient	-	-	0.3
Analysis	-	-	0.9
Total			11.4

laboratory at that time. There are several contenders searching for new T or CP violating physics at the LHC, Super B factory, neutron EDM *etc.*, whose finding should be related to those of our experiment. In order to contribute to the world-wide efforts to look for new sources of T or CP violating physics, the experiment should be conducted as soon as possible.

5 Proposed J-PARC experiment

5.1 The E246 upgrade experiment

Considering the current experimental situation of direct CP violation studies and searches for new physics as discussed in Section 2, we believe that it is essential to perform a P_T measurement in $K_{\mu 3}^+$ at J-PARC, which offers a far superior experimental environment as compared to E246. It is our view that this experiment ranks high among the particle physics research program at low energy. It would be a great loss for the CP violation physics if this experiment would not be pursued beyond the level of 10^{-3} of E246. We strongly feel that it is our obligation to carry out this measurement at J-PARC.

The 40 year history of P_T experiments shows a rather slow improvement in the upper limit. This is due to two reasons: the first point is that the statistical sensitivity of asymmetry measurements scales as $1/\sqrt{N}$, while the single event sensitivity in rare decay experiments scales as $1/N$. The second reason is the nature of this high precision experiment which must be conducted and analyzed very carefully. The understanding and reduction of systematic errors can only be achieved step-by-step. We prefer to follow this approach for the J-PARC experiment and to proceed in a steady way to improve the sensitivity. We plan a long-range strategy to attain the goal of SM+FSI signal region of 10^{-5} in a few steps.

The E246 result was essentially statistics-limited. The largest systematic error in the error table, which was due to multiple scattering, is statistical in nature and it could have been improved as $1/\sqrt{N}$. This result was foreseen at the start of the E246 experiment. We propose to improve the E246 result by at least a factor 20, $(\delta P_T < 2 \times 10^{-4})$, by improving both statistical and systematics uncertainties. This sensitivity puts the experiment well into the region where new physics effects can be discovered, and even a null result would set tight constraints on thoretical models. If warranted, further sensitivity improvement towards 10^{-5} will be proposed in the next stage after we have been convinced of the possibility to pursue this experiment to such a high precision region. In that sense, the current proposal may be considered as a prelude to precision frontier experiments at J-PARC.

5.2 Experiment design

In the Letter of Intent LOI-19 [74], submitted in 2003, we proposed a new detector, which may be useful in the second stage as we aim for the precision down to 10^{-5}. However, further detailed studies revealed that there are several critical design points which are difficult to solve. They are:

- The muon spin motion cannot be controlled without a magnetic field. An absolute zero-field condition (less than 10^{-4}T) is not attainable over the large volume of the muon stoppers.

- The event selection only by π^0 spectroscopy and charged particle range measurement without magnetic analysis need careful studies regarding its feasibility. The acceptance estimate must be rechecked accordingly.

- Since the polarimeter is exposed to the target/beam region, more careful studies are

End view

$$A = \frac{N_{CW} - N_{CCW}}{N_{CW} + N_{CCW}}$$

+ STOPPER

e+ COUNTER

IRON POLE

GAP

COIL

TARGET

CsI(Tl)

π^0 forward

π^0 backward

Side view

Polarimeter Trigger Counte

e+ Counter

Target Fiber

C4

C3

TOF

C2

Ring Counter

Muon Stopper

Muon Degrader

π^0FWD

π^0BWD

P_T

P_T

+

+

+

Z

X

Y

Cryostat

Iron Pole

Lead Shield

Cherenkov

(CsI(Tl))
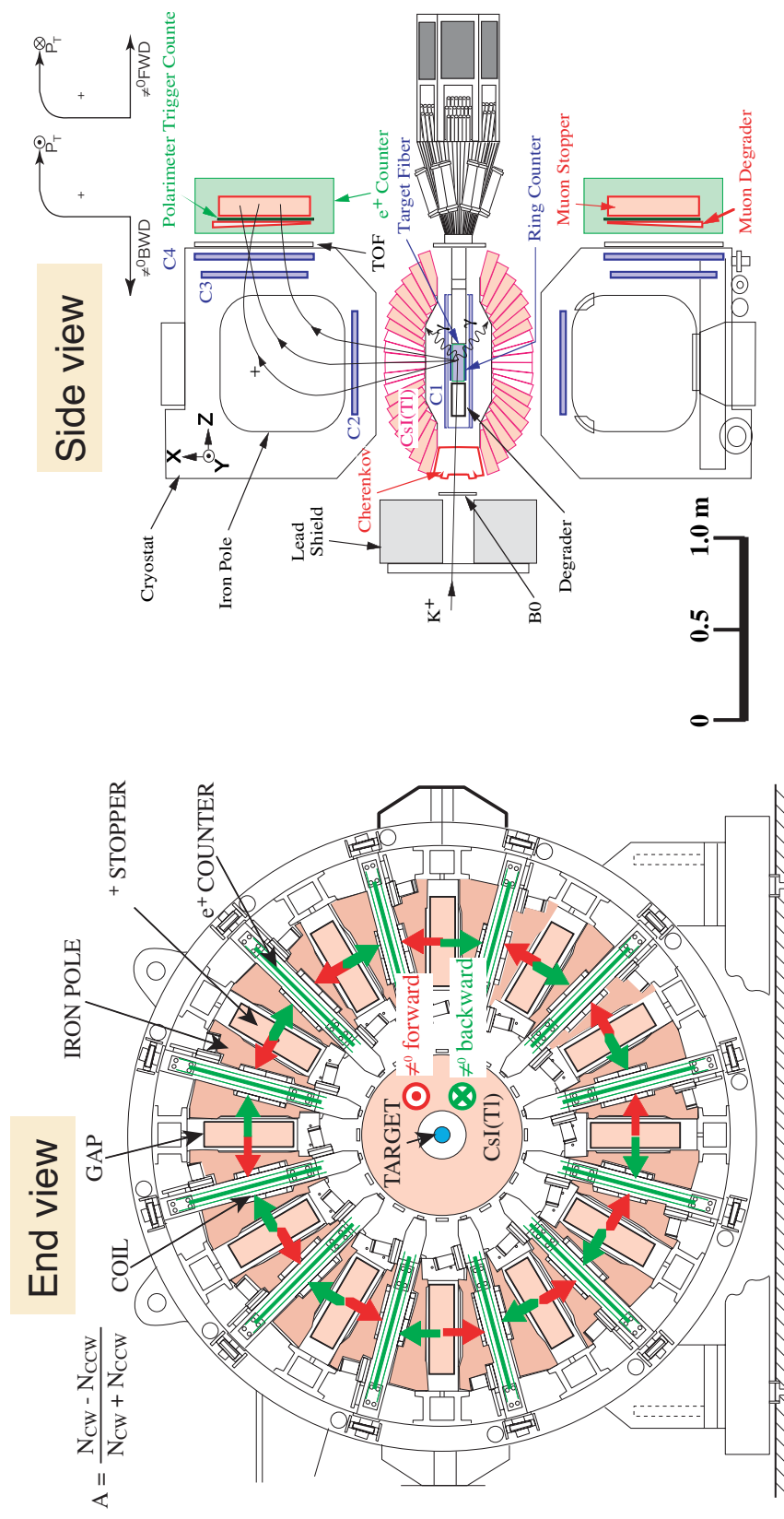
C1

Degrader

K+

B0

0   0.5   1.0 m

24

Figure 7: E246 setup

needed to demonstrate its performance under the high rates and a high background environment.

These difficult issues brought us to the conclusion that we should perform a step-1 experiment by upgrading the E246 detector. The idea of a new detector construction was motivated mainly for two reasons; one was the intention to strengthen the $K_{\pi2}$-dif ($K^+ \to \pi^+\pi^0$ with π^+ decay in flight) rejection capability and the other was the necessity to meet the high rate condition of the J-PARC beam. The first concern is less problematic if we use only the 2-photon events of the $K_{\mu3}^+$ sample and the latter turned out not to be a serious problem in Phase 1 of J-PARC, when only the production target T1, which is shared by 3 secondary beamlines, will be installed. The current beamline design for the stopped beamline at the T1 target gives only a few times 10^6/s of beam intensity, namely only a few 10 times larger than that at E246, far lower than 10^7/s which was supposed in the letter of intent. Hence, an upgrade version of E246 becomes a reasonable choice.

5.2.1 Advantage for stopped beam method

The salient feature of the E246 experiment was the use of a stopped beam and it was conceptually distinct from the previous BNL-AGS experiments where in-flight K^+ decays were adopted for the K^+ decay. The advantages of using decays at rest have been elucidated on several occasions: at the beginning of E246 [70], in the proposal for the BNL experiment [72] as well as in the final paper of E246 [71]. They are briefly summarized below:

- Isotropic decay of K^+ at rest involves all the kinematic conditions covering the full decay phase space. By using a symmetric detector like E246 one can look for the T-odd asymmetry effect in its positive value Dalitz-plot region as well as in its negative region. In E246 a double ratio measurement, namely the comparison scheme between forward-going pion events and backward-going pion events was possible. Such a double ratio measurement is essential for high precision experiments.

- The kinematical resolution is determined in the CM system in at-rest decays. The energy regions extend up to about 250 MeV and the energies acn be easily measured with sufficiently high resolution. The decay particle are detected in the entire 4π sr solid angle region and the relative angles of the particles are measured with good accuracies, limited only by the detector resolutions.

- The isotropic decay at rest, with large solid angle coverage ensures that the count rates are distributed over many segmented detectors, thus keeping the count rates low enough to minimize the pile-up problems. This is an important feature, especially for the electromagnetic calorimeter.

- For a stopped beam experiment, we need not be concerned about the beam history nor the finite emittance of the K^+ beam. The latter is usually large in the case of a low momentum beam and can cause severe problems in the case of in-flight decay experiments. The kaon stopping distribution is a consequence of the the beam emittance in this experiment. Asymmetries in the stopping distributions, however, involve only 3 parameters of coordinates and they are easy to handle.

25

- Most parts of the detector are located outside the beam region. Hence, the beam related pileup effects or background problems are less serious.

5.2.2 Advantages of the E246 setup

The superconducting toroidal spectrometer (E246 setup) offers many advantages in addition to those enumerated above.

- The relatively large bending power for charged particles in the field of 0.9 T provides sufficiently good resolution for charged particle analysis. Although this was not fully utilized in the E246 geometry, an upgraded charged particle tracking system can make a full use of it.

- The bending of nearly 90 degrees by the edge pole magnet creates a quasi-focal plane with large dispersion at the exit of the magnet. This arrangement effectively prevents most of the background channels such as $K_{\mu 2}$ and $K_{\pi 2}$ from entering the polarimeter.

- The presence of a quasi-focal plane enables a relatively small muon stopping volume when a wedge-shape momentum degrader is inserted. This is a rather important condition since the relevant momentum range of $K_{\mu 3}$ is wide – 100 to 200 MeV/c.

- The toroid was assembled with very high precision and the 12-fold rotational symmetry of the system is well ensured. The 12 gap median planes were checked to cross each other at the virtual central axis within an accuracy of 0.3 mm when the magnet was assembled lying on the floor. After it was set upright a vertical diameter change of 2 mm was observed, but the consistency of the median planes remained within 2 mm.

5.2.3 Lessons from the E246 experiment

The E246 experiment was statistics limited and the contributions of the systematic errors was not significant. However, we conducted very thorough studies of the systematics, which proved to be very useful for the design of the J-PARC experiment. The systematic errors, arising from an admixture of P_N causing spurious effects, are discussed in the next subsection. Here, we summarize other points which are regarded as disadvantages if the E246 detector system was to be used without modifications for this experiment.

- Small acceptance for charged particles including positrons. In particular, the solid angle coverage of the positron counters was about 10% in each side. This was an inevitable consequence of the adoption of the passive polarimeter and the asymmetry measurement scheme by means of the left/right counters. To suppress systematic errors, each positron counter served as the detector for clockwise (cw) emission and counterclockwise (ccw) emission from the stoppers on its two sides. Thus the solid angle coverage was inevitably small. The spectrometer acceptance for charged particles was also small (about 10%) but this can be regarded as the cost one has to pay for the bending and tracking performance.

- Admixture of $K_{\pi 2}$ pion decay-in-flight background. This was significant in the case of π^0-1γ events. Since these background muons have a transverse polarization component, they cause spurious effects. These effects should be symmetric in each gap across its median plane and the integration over the gap should average out. The fractional contamination at a few % level was tolerable in E246 but this is not acceptable for the J-PARC measurement.

- Large accidental backgrounds in the CsI(Tl) calorimeter. This was caused by the non-ideal beam condition at K5 which had a rather large π^+ to K^+ ratio and the associated pion beam halo and rather poor structure of the extracted proton beam from the synchrotron. Although this background should have produced no bias or spurious effects, an improvement in the beam condition is very much desired. And also a modification of the CsI(Tl) readout scheme should be pursued.

- The muon magnetic field distribution was not uniform in its strength and flux direction. The curved flux line diminished the analyzing power and also resulted in a relatively large systematic error.

- Alignments of the detector elements were done by the actual geometry measurement and the estimate of the systematic errors due to misalignments relied upon the accuracy of the measurement. The maximum precision obtained in this way was not better than the 10^{-3} level which was sufficient for E246. However, this has to be improved in the new J-PARC experiment.

5.2.4 Strong arguments for the E246 upgrade experiment

Despite these observations, there are strong arguments which favor performing an experiment in the J-PARC phase 1 with the toroidal spectrometer system by upgrading the E246 detector system. We present them below:

- The basic performance of the spectrometer is well known to us. Although some upgrades are required in the charged particle tracking, the motion of charged particles in the E246 magnet is well understood and reproduced well in our simulation. We have carried out, over a period of many years, intensive studies of the CsI(Tl) calorimeter response incorporating its complex geometry of the muon hole and the entrance/exit holes. This system is very well understood.

- The spectrometer magnet as well as the CsI(Tl) calorimeter are the components which were designed and manufactured with high precision. They were assembled very carefully in order to ensure their performance in a high precision experiment, and have been proven to work without any problem.

- We have full knowledge of the overall performance of the total system including the beam collimation, kaon stopping target, muon slowing-down, and the polarimeter system. For example, we can utilize the existing wedge-shape muon degrader system which has been well tuned. We know the sources of systematic errors very well and we are able to design the upgrade detector based on the experimental data.

- Finally, the relatively low cost for starting the step-1 experiment as early as possible also favors an upgrade of the E246 detector.

Also, as mentioned above, the fact that the beam intensities in the phase 1 of J-PARC will not be very high, makes it unnecessary to develop a completely new calorimeter. If we increase the speed of the readout scheme by changing to a faster system based on recent technical developments, we will be able to handle a few times 10^6 per second kaon beam.

Our aim is to perform an experiment which, in comparison to E246, will have about ten times more acceptance (using active polarimeter described below), about ten times the integrated beam flux, and a few times higher analyzing power, to achieve nearly a factor of 20 improvement in the sensitivity, i.e. δP_T (one sigma limit)$\sim 10^{-4}$. We feel confident that we can accomplish this task with the following modifications.

5.2.5 Necessary detector upgrades

In order to overcome the above mentioned limitations of the E246 experiment and to optimize the performance of the Toroidal Spectrometer System, several improvements in the detector system must be undertaken. These are described briefly below and in detail, item by item, in the next section. We will keep the principal concept of the experiment, namely the application of the muon magnetic field in the azimuthal direction parallel to the P_T component, and the object of the measurement in this experiment is primarily the *cw-ccw* positron asymmetry in the azimuthal direction, i.e., we keep the fwd/bwd scheme. As for the π^0 detection we cannot use 1γ events anymore since this gives rise to significant background contamination. It is expected that the statistics from the 2γ events only is sufficient to achieve the goal of our experiment in the phase 1.

1. **Target:** As described in Section 7, we may expect a smaller kaon beam spot in the stopping target. The diameter of the cylindrical fiber bundle target is a critical parameter because of the scattering and energy loss of the charged particles. The interactions such as the conversion of photons or annihilation of positrons are significant. We will adopt $d = 6$ cm, much smaller than the E246 target with $d = 9.3$ cm. The active length of the fibers will only extend within the necessary region, thus leaving the fiducial counter only as the TOF start counters. The segmentation will also be optimized.

2. **Charged particle tracking:** In E246 we had only 3 chambers of C2, C3 and C4 as high resolution tracking elements without redundancy and as a consequence the χ^2 resolution necessary for $K_{\pi2}$-dif background rejection was poor. Two more element will be added to improve this situation. A GEM (Gas Electron Multiplier) detector will be used as the innermost chamber where we have to accept a very high counting rate. The material thickness in total will be balanced to ensure the background rejection ability.

3. **Muon polarimeter:** An active polarimeter will be employed. The muon decay vertex will be localized with a high position resolution. The energies and emission angles of the decay positrons will be measured under a magnetic field. These measurements will increase the analyzing power very significantly. By using a muon stopper of sufficiently large volume, the detection of positrons with a 4π solid angle will be possible, producing a 10 times larger detector acceptance compared with E246. A parallel plate drift chamber with the planes parallel to the spectrometer gap median plane is adopted as the muon stopper.

4 **Muon magnetic field:** A new magnet system will be added to apply the field on stopped muons parallel to the P_T component. The field strength is designed to be the minimum field ensuring the stray-field decoupling capability and the performance of energy determination in the decay positron tracking. This is at least 300 Gauss. We now have fairly well developed ideas about the ways to ensure good alignment in installation of the system. A precise field mapping will be performed.

5 **CsI(Tl) readout:** We will keep the CsI(Tl) crystals, but we will replace the E246 readout system consisting of a PIN photo-diode, a charge-sensitive preamplifier, a shaping amplifier and a peak-hold ADC by a faster system. A reverse-type avalanche photodiode (APD) with large surface area is a candidate. The self-amplification of 50 makes the amplifier system simpler. An increase in the counting rate capability of a factor ~ 10 is expected.

6 **Readout electronics and data taking:** All the readout electronics will be replaced with the J-PARC standard system (COPPER/VME) developed by the KEK electronics shop. The rate performance will be greatly improved. Flash ADCs (FADC) and pipeline TDCs will be fully used.

Needless to say, the elements of 1) beam hodoscope, 2) beam Cherenkov counter, 3) collimator system, 4) veto counter system *etc.* will be retuned or remade for the new experimental condition. The basic experimental conditions and planned upgrades are summarized in Table 4 in comparison with E246.

5.2.6 Possible improvements in the analysis

In E246 the simplest analysis scheme was chosen for the sake of ease of control the systematics. It consisted of 1) integral analysis of the π^0 emission direction (namely forward region and backward region), as well as the 2) integral analysis in regard to the positron emission direction (left and right counters). The introduction of an active polarimeter in the proposed experiment enables the event-by-event positron asymmetry measurement relative to the decay plane of each event. Although the most important analysis will, as in E246, be based on the *fwd* and *bwd* regions with $A_T = (A_{fwd} - A_{bwd})/2$ because of the adoption of a chamber structure with parallel plates, the analysis in terms of $A_T = (A_{left} - A_{right})/2$ becomes possible and can be used not only in the control measurements but also for the main data.

5.3 Suppression of systematic errors

As was mentioned in the introduction, the proposed experiment aims for a one sigma P_T precision of 10^{-4}. As shown below, a one year (10^7s) run at J-PARC should provide a statistical accuracy of 10^{-4} with the upgraded detector. Roughly speaking, the gain of the positron detection efficiency with a nearly 4π solid angle and the weighted analysis along with the 10 times higher beam intensity will result in a sensitivity of about 20 higher than in E246. Hence, the total systematic error has to be suppressed to the same level of 10^{-4}. As was listed in Table 3, E246 ended with a total systematic error of 1.1×10^{-3}. In E246 it was not necessary to reduce the systematic error down to the 10^{-4} region, since the statistical accuracy was known to be at the level of 10^{-3}. It is a prerequisite of this

Table 4: Outline of the proposed experiment in comparison with E246

	This proposal	E246
Methodology		
Beam	stopped K^+	stopped K^+
Detector setup	Toroidal Spectrometer with upgraded E246 setup	Toroidal Spectrometer with E246 setup
Asymm. measurement Polarimeter	Active polarimeter	Passive polarimeter
Field method	Longitudinal $\mathbf{B} \parallel P_T$ $B = 300$ Gauss by dipole magnets	Longitudinal $< \mathbf{B} > \parallel P_T$ $B = 150\text{-}300$ Gauss by SC toroidal magnet
π^0 selection	primarily in fwd and bwd integral or event-by-event option of event by event in L/R $< \cos\theta_T >$ correction for integral	integral in fwd and bwd correction by $< \cos\theta_T >$
e^+ detection	event-by-event with E_{e^+}, θ_{e^+} measurement	integral in the e^+ counter
P_T deduction	weighted analysis	use of analyzing power α $P_T = A_T/(\alpha < \cos\theta_T >)$
π^0 detection	2γ	$2\gamma + 1\gamma$
μ^+ tracking	5 chambers + target	3 chambers + target
Alignment	10^{-4} by positioning and using data	10^{-3} by positioning
Main upgrades		
Tracking	C0(GEM)+C1(GEM)+C2+C3+C4 in He gas bag	C2+C3+C4 in air
Target	~ 60mmϕ with 2.5×2.5mm Sci.fiber (L=0.2m) SiPMT readout	93mmϕ with 5×5mm Sci.fiber (L=1.85m) 1/2" PMT readout
π^0 detection	CsI(Tl) with APD readout with FADC	CsI(Tl) with PIN readout with PH-ADC
e^+ detection	active stopper with DWPCs	plastic counters
Data taking	KEK-VME, COPPER system	TKO+FASTBUS, UNIDAQ

proposal that the systematic error be pushed down to 10^{-4}. In other words, the success of the proposed experiment depends heavily on the improvement of the systematic errors.

As mentioned above, the largest contribution to the systematic error (see Table 3) is the ambiguity of the real muon stopping point since it gets obscured due to multiple scattering through the Cu momentum degrader. This is not relevant in the new experiment where the muon stopping position is exactly determined by the introduction of an active stopper. The decay plane rotations, namely the mean values of the decay plane angle distributions, had non-negligible contributions. Although they were treated as errors, they are essentially the quantities for which the P_T result is corrected exactly. To obtain the 10^{-4} accuracy in the new experiment, these corrections will be required.

Thus, the muon field alignment remains the most serious source of systematic error. Once a parallel field is realized, it is not necessary to consider the small shift of the distribution in the field direction. The parameter ϵ is accordingly no longer relevant. The rotation around the y axis also has no influence in the new polarimeter system as in E246. The small rotation around the r axis, if any, is $fwd\text{-}bwd$ canceling and rather harmless. The rotation around the z axis is troublesome because its effect cannot be canceled in the $fwd\text{-}bwd$ subtraction scheme. In fact, E246 suffered from this error. This effect of δ_z seems to be an inherent systematics in any P_T measurement using a magnetic field.

However, the final P_T result can be corrected for this effect as well as the decay plane rotation $< \theta_z >$. This was not done in E246 because the precision of the field angle measurement (1mr) with a Hall element was not sufficient to give an error to the correction of similar size. In the new experiment is a δ_z measurement will be done using data. The way to measure δ_z also involves the determination of δ_r and two rotation angles of the polarimeter itself. This is described in detail in Section 8. It is concluded that the determination of δ_z and accordingly its correction can, in principle, be done with the statistical accuracy of the data. The detailed estimate of the actual error will be done in a Monte Carlo simulation.

Among other sources of errors in E246, the items related to the shifts of positron counters in E246 and no longer relevant for the active polarimeter, where the shifts and rotations are measurable and can be corrected as described in Section 8. The errors associated with the analysis are not essential and they will be improved in the new experiment. The changes of the major systematic errors due to detector misalignments from E246 are summarized in Table 5. The detailed estimates of the errors for the new sources in the new detector system are based on Monte Carlo simulations and they will be given in Section 8.

Table 5: Possible improvements of systematic errors from E246

Source in E246	δP_T in E246	this proposal
μ^+ multiple scattering	7.1×10^{-4}	of no consequence
Decay plane angle (θ_r)	1.2×10^{-4}	corrected
Decay plane angle (θ_z)	0.7×10^{-4}	corrected
$\vec{B}$ offset (ϵ)	3.0×10^{-4}	not existing
$\vec{B}$ offset (δ_r)	0.4×10^{-4}	measured by data and corrected
$\vec{B}$ offset (δ_z)	5.3×10^{-4}	measured by data and corrected
e^+ counter shifts and rotations	2.9×10^{-4}	not existing
Shifts of other elements	3.2×10^{-4}	measured by data and corrected

6 Detector upgrade

6.1 Target

6.1.1 Necessity for a new target

The existing E246 target consists of an array of 256 plastic scintillation fibers, each with a square cross section of 5×5 mm^2. Twelve fiducial counters with individually matching shapes surround the fiber array give it an almost cylindrical surface. The dimensions of the target were chosen according to the conditions of the kaon beam at the KEK 12-GeV proton synchrotron. The transverse extension of 9.3 cm was designed to completely cover the kaon stopping distribution. The momentum spread of the kaon beam required the length of the fiducial zone to be 20 cm, which was defined by the fiducial counters attached on the target. In addition, the target cylinder is surrounded by an array of scintillating ring counters, with each ring 6 mm wide. The ring counter hit provides information of the z position of the outgoing charged track. At J-PARC, a new target is needed due to the following reasons.

- The kaon beam parameters will allow for a reduced width of the target. The expected vertical and horizontal K^+ profile of the planned K0.8 beamline at J-PARC is shown in Fig. 27. At the same time it will be necessary to make a system which can work under the high beam rate condition. Although the contaminant π^+ flux should be relatively smaller, it is preferable to have a finer segmentation.

- The fibers of the E246 target are exposed to the beam with their 1.8 m lengths. To reduce accidental hits under the high rate condition, we prefer to have an active zone only long enough to stop the kaon beam, i.e, 20 cm.

- In the proposed experiment we pursue a higher performance for charged particle tracking. In order to attain better momentum resolution, a smaller target is essential. More useful trajectory information will also be obtained from finer segmentation.

6.1.2 Requirements for the target

Due to the emittance and multiple scattering during the stopping process the resulting vertical and horizontal kaon stopping distributions will be somewhat wider than the beam

profile in Fig. 27, however they will still be much narrower than in the E246 experiment. However, a reduction of the target width from 9.3 cm to 6.0 cm is proposed. The momentum spread of the kaon beam allows all kaons to be stopped within the 20 cm long active target region.

The main disadvantage of a large target diameter is that it results in significant conversion probabilities for the outgoing photons from the π^0 decay that can obscure the performance of the CsI calorimeter. Processes such as photon pair production and bremsstrahlung as well as e^+ annihilation influence the observed photon yields and are sources of backgrounds that scale with the width of the target. Another disadvantage of a large target width is the deflection of outgoing charged particles due to multiple scattering. Also, the Landau straggling in the target material causes a momentum spread of the outgoing charged kaon decay products. While the multiple scattering smears the orientation of the $K_{\mu3}$ decay plane, the momentum spread due to the target material decreases the ability to identify the two-body decay channels $K_{\pi2}$ and $K_{\mu2}$ in the spectrum of charged-particle momentum.

Both multiple scattering and Landau straggling are symmetric with respect to the acceptance, hence neither process would affect the measured result for the average asymmetry. Possible average acceptance offsets due to an asymmetric kaon stopping distribution are canceled by averaging the 12 sectors of the spectrometer. The precision with which the orientation of the $K_{\mu3}$ decay plane is determined depends on the angle resolution of both the reconstructed π^0 and the charged muon track. While the angle resolution for the γ detection and hence for the π^0 reconstruction is given by the size of the CsI crystals amounting to a few degrees, the angle uncertainty of the charged track is limited by the multiple scattering in the target and detector materials. However, for the error of the P_T measurement only the uncertainty of the average decay plane rotation matters and this is reduced by $1/\sqrt{N}$ where $N \simeq 10^8$ is the number of acquired events. Given the large statistics of the J-PARC experiment this error becomes negligible.

6.1.3   Optimum fiber thickness

The thickness of the target fibers sets the precision with which the average (or most likely) energy loss can be determined and accounted for in the charged track reconstruction process. At the same time, the total energy loss of the charged track in the target is accompanied by an energy spread following a Landau distribution. The optimum thickness of the target fiber and thus the best required vertex resolution is given when the former uncertainty on the average energy loss is balanced with the latter energy resolution due to Landau straggling. In order not to limit the resulting momentum resolution by the original fiber thickness, it is desirable to reduce the fiber width at least in the same proportion like the total target width[5].

Another reason for a higher segmentation of the target is motivated by the ability to suppress muon events from the $K_{\pi2}$ channel where the pion decays in flight ($K_{\pi2}$-dif). Such events show a kink in their track at the location of the in-flight decay vertex. By

---

[5]Here we assume that the resolution of reconstructed momenta due to the intrinsic resolution of the tracking elements and the presence of material along the tracking path does not exceed the momentum broadening in the target. With the proposed improvement on the charged particle tracking capability (see Sec. 6.2) this is a realistic assumption.

comparing the closest distance from the target of the fitted charged track with the radial position of the target fiber in which the K^+ was stopped one can identify events that have a kink in their track between the target and the nearest tracking element. Likewise, a kink in the track for decays within the target can be observed from the pattern of the fiber hits by the outgoing pion and muon track.

On the other hand, it is clear that the scintillating fibers cannot be made infinitely thin. A critical quantity is the light output for a given fiber thickness. A lower limit while still maintaining sufficient gain is typically reached at 2 mm thickness taking the attenuation over the length of the lightguides into account. It is therefore proposed to reduce the present target fiber thickness of 5 mm in the E246 target to 2.5 mm in the new target.

6.1.4 Proposed target design

The 6 cm diameter scintillating fiber stopping target will consist of 432 square fibres (2.5 mm on a side) as shown in Fig. 8. Each fiber will be read out using four 1 mm diameter double clad clear fibers (BC-98 or Kuraray clear-PSM) into individual ADCs after suitable amplification. The exact type of scintillating fiber (BCF-12 or Kuraray SCSF-38) will be determined after extensive testing. The clear readout fiber will be glued to the scintillating fiber. Figure 9 shows the fiber readout schematically. For E246 we obtained $\simeq 17$ photo electrons per MeV for minimum ionizing particles by coupling each 1.85 m long scintillating fiber (BCF-12) directly to a Hamamatsu H3164 PMT using an air gap. For the proposed experiment we plan to evaluate the new SiPMTs currently being developed by MRS-CPTA in Moscow before making our final decision. Such small solid state PMTs offer the advantages of compactness and lower cost but they have not yet been proved to be as reliable as conventional PMTs. However, the test results of Rykalin [75] and the T2K group of Kudenko *et al.* [76] look very promising. As for the photo-electron yield we might be able to expect ∼10 for each SiPMT calculating from the current number $17p.e.$/MeV taking into account 1) a photon production of 50%, 2) no attenuation through the clear fiber, 3) good quantum efficiency even with 4) a bad transmission from the fiber to the clear fiber of $\sim 10\%$.

If we decide to use conventional PMTs we would test and recycle as many of the existing E246 target PMTs as possible. Given the high rates expected in the scintillating

Table 6: Main parameters of the new target

Parameter	Value	E246 (reference)
Diameter	≈ 6 cm	9.3 cm
Active length	20 cm	180 cm
Fiber size	2.5 mm × 2.5 mm	5mm × 5mm
Number of fibers	432	256
Light readout	4 clear fibers for each fiber	SciFi itself
Light conversion	SiPMT for each clear fiber	1/2" PMT (H3164PX)
Number of photo-electrons	≈ 10 / SiPMT for MIP	17/MIP on the average
SciFi/clear fiber coupling	gluing	-
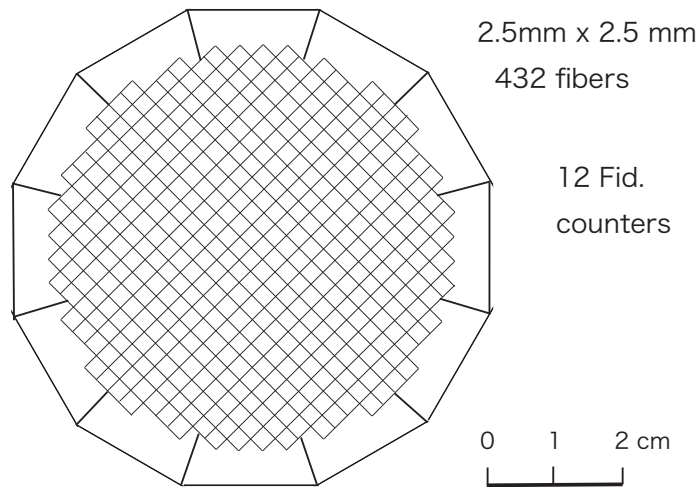
Figure 8: Scintillating fiber target for the proposed experiment. The active zone has a length of 20 cm and a diameter of 6 cm. Each of the 432 scintillating fibers has a 2.5×2.5 mm^2 square cross section. The fiber bundle is surrounded by 12 fiducial counters.

target we do not envisage being able to use multi-anode PMTs.

As in E246 there will be 12 fiducial counters (thickness $\simeq 5$ mm) surrounding the target fibres for triggering and TOF measurement to separate the outgoing muons and electrons. These fiducial counters would interlock with the outer layer of scintillating fibers as shown in Fig. 8.
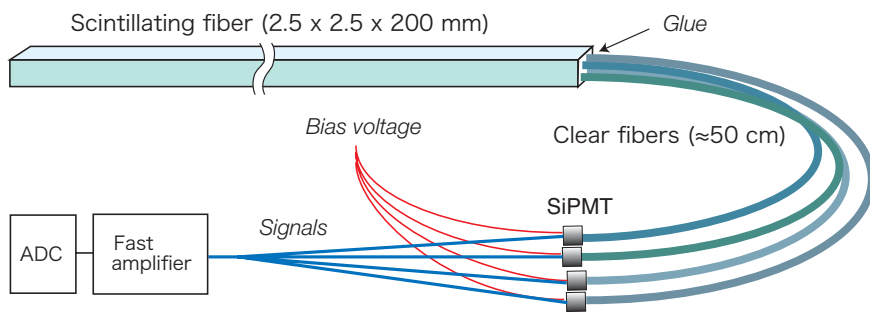
Figure 9: Schematic readout for each of the 432 fibers in the target bundle for the proposed experiment.

6.2 Tracking

In the proposed experiment, the systematic errors on P_T need to be suppressed to the 10^{-4} level. In E246 the systematic error due to background events and limited accuracy of alignments was at 10^{-3} level. In order to achieve such an improvement in the systematic errors, a significant upgrade of the tracking system has to be pursued. The capability to perform high-resolution tracking (momentum, angle, and vertex) of the charged particles from K^+ decay in a momentum range of 100–250 MeV/c, and background rejection capability present essential and powerful aspects of the proposed experiment:

- High momentum resolution is needed to distinguish the two-body decay channels $K_{\pi2}^+$, $K_{\mu2}^+$ from three-body decays and serves to suppress background in the $K_{\mu3}^+$ event sample.
- A well defined angle of the charged track along with the angle of the π^0 reconstructed by the CsI calorimeter is important to obtain a good $K_{\mu3}^+$ kinematical resolution. Good angle resolution is also required to select back-to-back $K_{\pi2}^+$ events for calibration.
- Excellent vertex and angle resolution is required to identify events from pion decay in flight ($K_{\pi2}^+$-dif). While these events present a background that needs to be sufficiently suppressed, this event type will be selected for the calibration of the polarimeter alignment. Additional and elaborate tracking capability is required to locate the kink and detect the deflection angle of the muon from the original pion track.

6.2.1 Tracking in E246

In E246, five different tracking elements have been employed, three planar multiwire proportional chambers (MWPC) C2, C3, and C4, a cylindrical drift chamber C1, a scintillating fiber target and ring counters surrounding the target. (Fig. 10) For each of the 12 sectors, positively-charged tracks leaving the target in the transverse direction pass through the gap of the CsI calorimeter and are bent in the toroidal magnetic field by about 90°. The track reconstruction has been based on the three planar chambers C2, C3 and C4 and the ring counters. The C2 element is located at the entrance gap of the magnet, while the C3 and C4 chambers reside near the focal plane at the exit gap of magnet in front of the muon polarimeter. Near the target, another element, C1 drift chamber with cylindrical geometry was installed. However, due to its imperfect high rate performance, the C1 chamber was not been included in the final analysis. Thus, only the ring counter was used for tracking in the source vicinity, but it had a much worse resolution (width was 6 mm) compared with the other chambers. The momentum of the charged particle was deduced from the reconstructed momentum corrected for the energy loss in the target. The backgrounds were rejected in the momentum spectrum as well as in the χ^2 cuts of the track fitting. The part of $K_{\pi2}$ background which fell in the same momentum range was removed by the latter.

The limitations of the E246 tracking system relevant for the proposed experiment are summarized as follows.

- The momentum resolution was 3.6 MeV/c or 1.8% for the 205 MeV/c $K_{\pi2}$ peak. It was sufficient for E246, but is certainly not good enough for the J-PARC experiment.

The reasons for this rather bad resolution were 1) incomplete energy loss correction in the target due to Landau fluctuation, and 2) the intrinsic tracking resolution determined by the short distance between C3 and C4.

- Since there was no redundancy for the number of tracking elements with high resolution, the χ^2 resolution necessary for $K_{\pi 2}$-dif removal was not very high. The remaining background from $K_{\pi 2}^+$-dif events was up to 2.4% of the $K_{\mu 3}^+$ yield. The effect of this background on the transverse polarization mostly cancels in the gap acceptance integration and fwd/bwd asymmetry scheme. Although the remaining contribution to the systematic error on P_T turned out to be small ($\simeq 6 \cdot 10^{-5}$), it had the potential to be larger, and it would be better to keep the $K_{\pi 2}$-dif fraction at the 10^{-3} level to ensure a spurious $P_T < 5 \times 10^{-5}$.

- The material presented by the tracking elements causes energy loss fluctuations and angle deflections due to multiple scattering. The space between the tracking elements was filled with air which also contributes significantly to the material budget.

6.2.2 New tracking system

At J-PARC, two sources of systematic errors dominate. While one source is given by the background contamination from $K_{\pi 2}^+$-dif events, the other source of systematics is due to misalignments of the setup, in particular of the muon polarimeter. With the proposed upgrade of the tracking system, the errors from both background and the alignment will be improved to meet the requirement of 10^{-4} for the systematic error in P_T. These performance goals will be achieved both by reducing the material budget along the track and by rearranging existing and adding new tracking elements in replacement of the previous C1 chamber. The momentum uncertainty of 3.6 MeV/c in E246 can be reduced by at least a factor of ten 1) by employing a 6 cm instead of 9.3 cm wide target with a segmentation of 2.5×2.5 mm^2 fibers instead of 5×5 mm^2, 2) by replacing the air volume in the magnet between C2 and C3 and before the C2 chambers with helium bags and by increasing the distance between the C3 and C4 elements to 30 cm. For sufficient identification and suppression of $K_{\pi 2}^+$-dif events we need to build a cylindrical tracking chamber ("C0") with a radius of 10 cm and a spacial resolution of <0.1 mm. The new C0 chamber will replace the previous cylindrical C1 chamber of the E246 setup. In order to increase tracking redundancy we propose to add a new planar tracking element (again named "C1") with <0.1 mm resolution to cover each of the 12 gaps at the outer surface of the CsI calorimeter. By adding these additional elements to the track fitting procedure, the resulting χ^2 per degree of freedom will be much more effective to distinguish tracks from $K_{\pi 2}^+$-dif from regular tracks which do not have a kink along their path. In combination with the higher segmentation of the fiber target this will be sufficient to suppress the $K_{\pi 2}^+$-dif /$K_{\mu 3}^+$ ratio below 10^{-3}, rendering a spurious $P_T < 5 \cdot 10^{-5}$.

The proposed modifications are in summary:

1) Thinner target, higher segmentation

2) Helium bags in the magnet between C2 and C3 and before C2

3) Increase of the distance between C3 and C4 to 30 cm
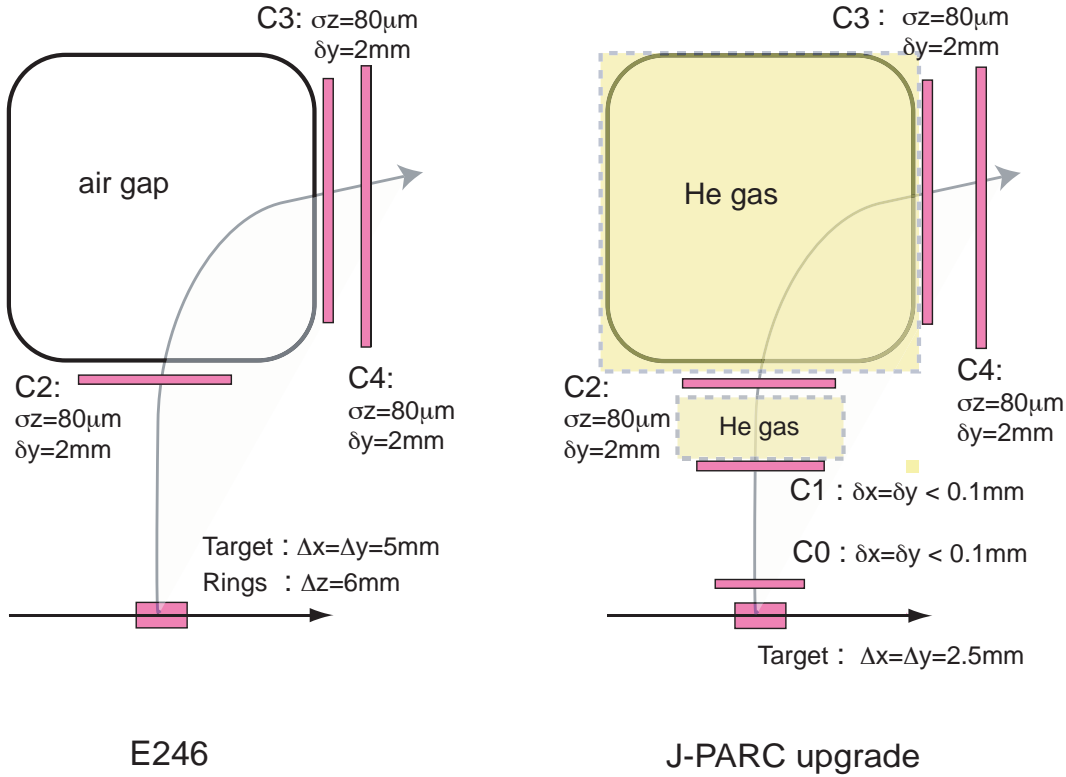
Figure 10: Schematics of the tracking system in the E246 setup (left) and the proposed setup for the J-PARC experiment (right).

4) Addition of new tracking elements: "C0" and "C1" chambers based on GEM technology

Figure 10 shows a comparison of the tracking system in E246 and the proposed experiment. Each item is described below.

- First of all, the material budget of both the target and the detector (tracking elements and air volume) has to be reduced. A slimmer target reduces the momentum spread due to the Landau straggling and the effect of multiple scattering. As discussed before, the expected kaon stopping distribution allows a reduction of the target width from 9.3 cm to 6.0 cm.

- To make use of these benefits on the achievable angle and momentum resolution the material budget of the detector volume and tracking elements needs to be optimized. In order to significantly reduce the material along the track from the target to the C4 plane, it is proposed to replace the air volumes in the magnet gaps between C2 and C3 and in front of C2 with helium bags. The average multiple scattering angle in 2 m of air $(0.66\% X_0)$ amounts to $0.9°$ which can be almost completely suppressed with the He bags.

- With a slimmer target and the air volume replaced by helium, the momentum resolution would be limited by the short distance between the C3 and C4 chambers which

Table 7: Main parameters of the charged particle tracking

Item	Value	E246 (reference)
High resolution elements	C0, C1, C2, C3 and C4	C2, C3 and C4
Scintillator elements	Target	Target + Rings
C0 chamber	cylindrical GEM chamber	C1 drift chamber
C1 chamber	planar GEM chamber	-
C2 chamber	MWPC (not changed)	MWPC
C3 chamber	MWPC (not changed)	MWPC
C4 chamber	MWPC (not changed)	MWPC
C3-C4 distance	30 cm	15 cm
Magnet gap	air	He gas bag
Total material thickness	$\sim 7 \times 10^{-3} X_0$	$6.6 \times 10^{-3} X_0$

is only 15 cm in the current E246 setup. With the new design of the active muon polarimeter and the planned magnet configuration in the focal plane region, the C4 chamber no longer needs to be so close to C3. It is therefore proposed to increase the distance between C3 and C4 to 30cm by moving C4 closer to the polarimeter.

6.2.3 Background rejection

An important aspect of the new tracking system in the proposed experiment is the ability to cleanly select event types such as π^+ from the $K_{\pi 2}^+$ or μ^+ from the $K_{\pi 2}^+$-dif decay channel for calibration and alignment purpose. A high momentum resolution makes it possible to identify events from the two-body decay channels $K_{\pi 2}^+$ and $K_{\mu 2}^+$ from the respective peaks in the momentum spectrum. The selection of such events from two-body kaon decay becomes even cleaner when the back-to-back opening angle with respect to the reconstructed π^0 is considered. The identification of $K_{\pi 2}^+$-dif events relies on the ability to detect a kink in the track of the π^+ where it decays into a μ^+. The kink manifests itself in both a poor χ^2 value of the fitted charged track as well as in a deviation of the reconstructed track vertex from the measured vertex position with a tracking element near the target. For a high sensitivity of this vertex consistency check multiple scattering of the track along its path has to be minimized and the element near the vertex needs to have a high spacial resolution. After replacing the air volumes with He bags the remaining dominant source of multiple scattering along the track will be the C2 element whose thickness of 0.27 %X_0 causes an rms deflection of 0.2° (0.6°) for 200 (100) MeV/c μ^+ tracks. In absence of further tracking elements between the target and the C2 element the multiple scattering in C2 would limit the possible vertex resolution to $\sim 0.5(1.5)$ cm, respectively, similar to what was obtained in E246.

The contribution of the $K_{\pi 2}^+$-dif background to P_T is odd in C4y and thus tends to largely cancel in the *fwd/bwd* asymmetry analysis scheme. Assuming a maximum transverse polarization component of the muons from $K_{\pi 2}^+$-dif of order unity and a conservative cancellation power of a factor 20, with a fraction of $K_{\pi 2}^+$-dif events of a few percent of the $K_{\mu 3}^+$ yield, the resulting spurious P_T would be on the order of 10^{-3}. In order to reduce

the $K_{\pi 2}^+$-dif contribution to P_T below $5 \cdot 10^{-5}$ at J-PARC, the background fraction of $K_{\pi 2}^+$-dif events in the final $K_{\mu 3}^+$ event sample can not exceed 10^{-3}.

6.2.4 New GEM chambers, C0 and C1

It is proposed to replace the existing C1 chamber with a new cylindrical chamber around the target ("C0") and to add new planar tracking elements ("C1") at the outer surface of the CsI calorimeter to cover the 12 gaps. The required reduction of $K_{\pi 2}$-dif contamination can be achieved if the fitted track vertex resolution at the location of the C0 element is on the order of 0.1 mm (it was about 1cm in E246). As the pion decay probability decreases exponentially, most pion decays appear close to the target. Hence, for an optimized sensitivity to the track consistency, the C0 chamber should have a radius as small as possible. For the proposed chamber a radius of 10 cm appears to be an appropriate choice. Both C0 and C1 will be based on recently developed GEM technology. GEM detectors for charged-particle tracking present a new generation of position-sensitive counters which are reasonably cheap, radiation-hard and well suited to be operated in high-rate environments. For further details, see Appendix B.

The number of $K_{\pi 2}^+$-dif events within a radius of 10 cm is still about 1% of the $K_{\mu 3}^+$ yield. It is therefore necessary to also identify $K_{\pi 2}^+$-dif events that decay between the target and C0 or even within the target. In order to suppress $K_{\pi 2}^+$-dif events from between the target and C0, a transverse track consistency test will be employed. By comparing the closest distance from the target of the fitted charged track with the radial position of the target fiber in which the K^+ was stopped one can identify events that have a kink in their track between the target and the nearest tracking element. Likewise, a kink in the track for decays within the target can be observed from the pattern of the fiber hits created by the outgoing pion and muon track. Another feature of a C0 chamber surrounding the target inside the CsI barrel is its function as a charged (software) veto for the CsI analysis.

The main parameters of the C0 and C1 chambers are summarized in Table 8 and Table 9, respectively.

Table 8: Main parameters of the C0 chamber.

Parameter	Value
Outer radius (readout layer)	10 cm
Inner radius (drift layer)	8 cm
Common He-filled volume with target	
Thickness as standard TGEM	0.70 %X_0
Thickness as light TGEM	0.20 %X_0
2D spiraling strip readout, pitch	635 μm
Number of channels	~ 1400
Position resolution	50-100 μm
Number of elements	1

Table 9: Main parameters of the C1 element.

Parameter	Value
Area	15×45 cm^2
Thickness as standard TGEM	0.70 %X_0
Thickness as light DGEM	0.11 %X_0
2D strip readout, pitch	635 μm
Number of channels	~ 1000
Position resolution	50-100 μm
Number of elements	12

6.3 CsI(Tl) readout

6.3.1 The CsI(Tl) barrel and current performance

The photon calorimeter of the E246 setup is a barrel of 768 CsI(Tl) crystals surrounding the target region (Fig. 11). There are 12 so-called muon holes to let the charged particle enter the spectrometer. The solid angle coverage is therefore not 4π but about 3π including also the losses due to the beam entrance and exit holes. The size of the muon hole was optimized for the $K_{\mu 3}^+$ acceptance to be maximum [66]. As is shown in Fig. 7 the barrel structure is symmetric for the upstream (backward) and the downstream (forward) side, which is essential in the present experiment. The barrel was assembled very carefully ensuring a local as well as a global precision of better than 1mm. This high precision was enabled by 1) an accurate dimension of each crystal model, 2) an accurate fabrication of the crystal housing made of Al sheets, and 3) a support structure with high precision and strong rigidity. The main parameters of the barrel are summarized in Table 10.

The calorimeter worked well in E246 and its performance has been reported elsewhere [66]. First of all, the high light yield of each crystal (11.000 $p.e.$/MeV) and the relatively low noise ($ENL = 70$ keV) enabled measurements with a low photon energy threshold, even though a PIN photo-diode readout was employed. Timing information could be also extracted and used in the analysis. The energy response function had a significant tail on the low energy side mainly due to shower lateral leakage into the muon holes, but the intrinsic energy resolution of the spectrum main part is reasonably good. The angular response for a photon was intensively studied with $K_{\pi 2}$ events. If only the "central events" with photon hits away from the muon holes are selected, an angular resolution of 2° is obtained. For all kinds of events it is about 2.4°. These angular characteristics become more important in the proposed experiment. The main performance parameters are summarized in Table 11 and Fig. 12 shows the typical response measured in the E246 data. The performance related to energy might be different after modifying the readout scheme, but the angular characteristics will remain almost the same.

6.3.2 Current conditions

Although this calorimeter suffered from the beam halo hits from the pion contamination in the beam for the forward innermost part (the π^+/K^+ ratio at K5 was nearly 10), a much better performance is expected at J-PARC, since the beam quality at the K0.8 channel is
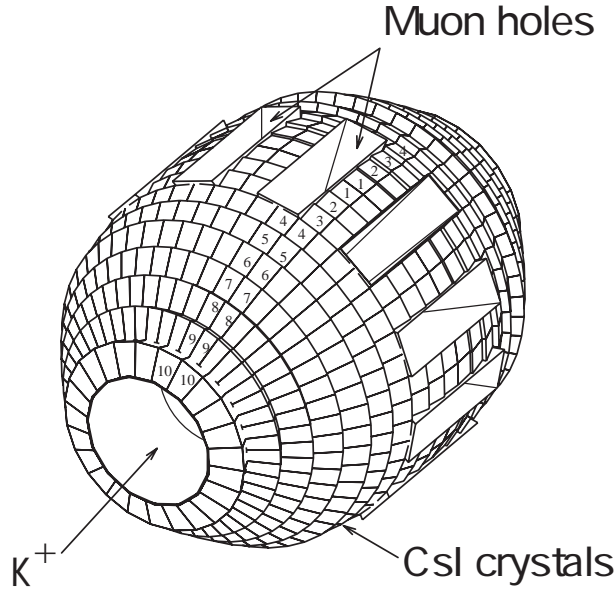
Figure 11: CsI(Tl) barrel with 768 crystal modules. There are 12 muon holes.

Table 10: Main parameters of the CsI(Tl) calorimeter.

Parameter	Value
Number of CsI(Tl) crystals	768
Segmentation	$\Delta\theta = \Delta\phi = 7.5°$
Inner /outer diameter	41 / 90 cm
Detector length	141 cm
Solid angle coverage	$\sim 75\%$
Crystal length	25 cm (13.5 X_0)
Typical size of crystals	$3 \times 3 - 6 \times 6$ cm^2
Wave length at peak	560 nm
Light decay time	~ 900 ns

Table 11: Performance of the CsI(Tl) detector in E246

Parameter	Value
Energy threshold for a cluster	5 MeV
Energy resolution (σ_E/E)	4.3% at 100 MeV, 2.8% at 200 MeV
Number of crystals of a shower	3×3
Angular resolution (rms)	$2 - 2.4°$
Spatial resolution (rms)	7.6 mm at 200 MeV
Time resolution of a cluster	3.5 ns at 100 MeV

predicted to be much better with a π^+/K^+ ratio of less than 0.5. Thus, there is no reason why the present barrel cannot be used in the proposed experiment from the point of view of its structure. Only the rate performance of the CsI(Tl) modules with a decay constant of 900 ns becomes relevant.

The barrel has been kept in a clean environment under a constant ambient temperature $(20 \pm 0.5°)$ and at low humidity of less than 15% since the time of its commissioning and also after the last run in 2001. There should be no concern about the degradation of crystal surface condition[6].

6.3.3 Current readout scheme and its limitations

Because of space constraints and the presence of a stray magnetic field from the superconducting toroidal magnet, a conventional photomultiplier tube could not be used. Instead we employed the PIN photodiode readout. The E246 readout scheme is shown in Fig. 13 and details are described elsewhere [67]. Large sized PIN diodes of 18×18 mm^2 or 28×28 mm^2 which were developed by Hamamatsu were successfully used in conjunction with a charge sensitive preamplifier based on CS507 (Clear Pulse Co.). The output of the preamplifier was fed to a main amplifier in which two outputs are made; one is a shaping amplifier output with a time constant of e.g. 1μs providing a pulse height signal to a peak-hold ADC, and the other is a timing-filter-amplifier output providing a timing signal to a discriminator. This readout scheme, however, does not work at the higher counting rate of the J-PARC experiment for the following reasons:

- The maximum acceptable rate of the charge preamplifier was determined by its output dynamic range and signal gain, which is calculated as $r_m = V_m/(QR_f)$ with the maximum voltage V_m, the average input charge Q, and the feedback resistance R_f. Because it is only 34 kHz, a higher rate would cause a loss of events with a high probability.

- The width (including the tail) of the shaping amplifier output pulse is nearly 10μs for a shaping time constant of 1μs. Higher rate results in a pileup of events degrading the energy resolution or even spoiling the event identity.

It is first checked which kind of improvements in the rate performance we may achieve if we construct a new amplifier system by keeping the present PINs. To solve the above

---

[6]In case the surface degradation will turn out significant, it is possible to re-polish the surface without losing much dimension accuracy.
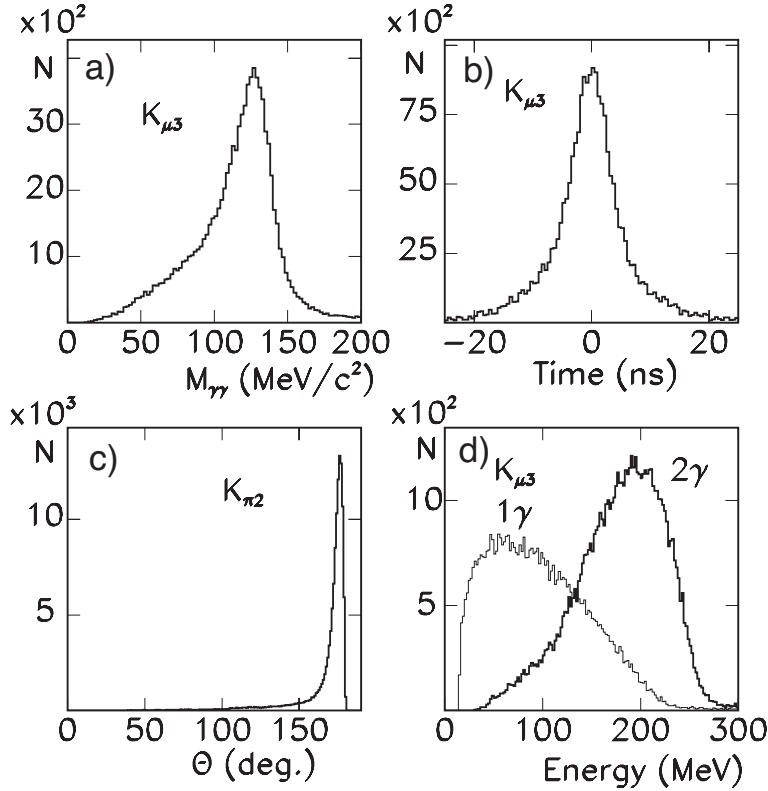
Figure 12: Performance of the CsI(Tl) detector for $K_{\mu 3}$ and $K_{\pi 2}$ in E246. a) Invariant mass spectrum of two photons of $K_{\mu 3}$, b) cluster timing distribution also of $K_{\mu 3}$ showing the time resolution, c) opening angle distribution of $K_{\pi 2}$ showing the angular resolution, and d) two-photon and one-photon energy spectra of $K_{\mu 3}$ events.

mentioned problems, both of the preamplifier decay constant and the shaping time constant should be shorter e.g. by a factor 10. A rough estimate is given in Table 12. Here an important point is the increase of the dark current in the course of E246 operation. This was 30 nA at the beginning but became more than 100 nA in 2001. Taking this factor into account the equivalent noise level (ENL) will be larger that 500 keV and nearly 10X higher than it was at the start of E246. Although the energy resolution of a π^0 is still dominated by shower leakage and not by ENL, it would not be a preferable situation to have larger noise when forming a photon cluster.

6.3.4 Avalanche photo-diode readout

Considering such limitations in the PIN + preamplifier scheme for high rate operation, we plan to adopt another CsI(Tl) readout method. One possibility is to use magnetic-field resistant photo-multiplier tubes now available with fairly large multiplication. However, the space limitation will still be a problem. There is also a cost question. Thus, we are led to consider avalanche photo-diodes (APD) of reverse type. Such APDs with multiplication factors of about one hundred with reasonably large sensitive areas are commercially
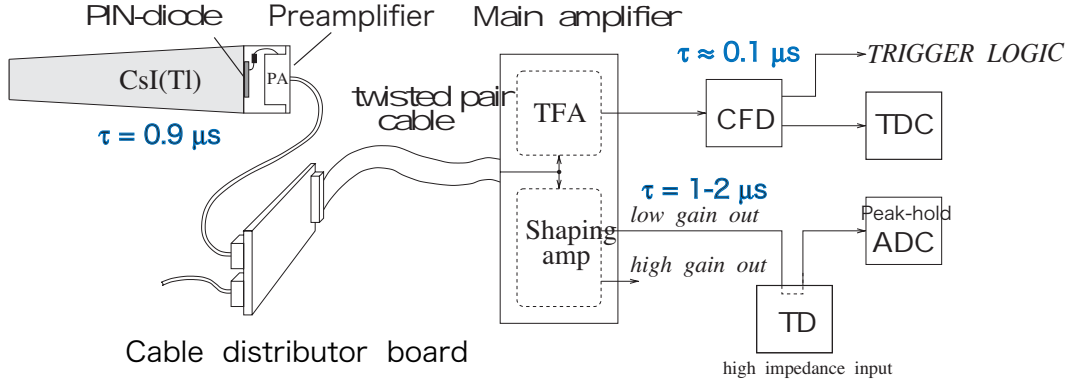
Figure 13: Current readout scheme of the CsI(Tl) calorimeter.

Table 12: Comparison of noise level and rate performance when keeping the PIN diodes.

Parameter	E246 (1995)	E246 (2000)	PIN+ new Preamp.
PIN diode	S3204-03	same	same
Photo-electron /GeV	1.1×10^7	same	same
Preamplifier	CS507	same	new preamplifier
Feedback C_f	2pF	same	same
Feedback R_f	330 MΩ	same	33 MΩ
Output decay time	$660\mu s$	same	$66\ \mu s$
Preamplifier gain	2V/pC for 100Ω	same	same
Dark current	30 nA	> 100 nA	> 100 nA
Shaper time constant	$1.5\mu s$	$1.0\mu s$	$0.1\mu s$
Noise (ENC)	640 e	$\sim 1000e$	$\sim 1800e$
Noise (ENL)	70 keV	$\sim 110 keV$	> 500 keV
Maximum rate (r_m)	34 kHz	same	340 kHz
Maximum rate $(1/10T_p)$	~ 100 kHz	same	~ 1000 kHz

45

Table 13: Readout scheme using APDs compared with the E246 PIN readout.

Parameter	E246-PIN	APD readout
Diode	1×S3204-03	4×S8148 (equiv.)
Total area	18×18mm^2	10×10mm^2
Quantum efficiency	∼ 0.70	> 0.80
Photoelectron /GeV	1.1×10^7	4.0×10^6
Diode gain	1	50
Electron yield@ 100MeV	1.1×10^6	2.0×10^7
Preamplifier	Charge sensitive	Current amplifier

available [77]. Several applications to calorimeters in high energy physics experiments are being prepared. One notable example is the adoption in the CMS experiment [78] for readout of PbWO$_4$ scintillators. The matching wave length (peak wave length = 430 nm) is nearly optimum for the Hamamatsu S8148 and two such APD diodes with 5×5mm^2 on each crystal should yield 10^7 electrons for a 100 GeV photon after a gain of 50. The wave-length matching of the CsI(Tl) with the peak wave length of 560 nm is much better and an average quantum efficiency greater than 80% can be expected. The readout of CsI(Tl) by an APD has already been studied in Ref. [79] by using Hamamatsu S8664 for a small crystal and it was found that it works well.

Although the photon energies of our interest are much lower than at CMS, the larger scintillating photon yield of CsI(Tl) compensates. Assuming that 1) 4 APDs are attached on each crystal with an area of 10×10mm^2 realized by the 2) the same amplification of 50 as the S8148, and 3) an average quantum efficiency of 0.80, we might expect 2×10^7 electrons for a 100 MeV photon. This one-order-of-magnitude larger electron yield than the PIN (E246) with 10^6 /100 MeV, allows us to use a current preamplifier with high gain in place of the costly charge preamplifier which would also encounter the rate limitation due to the output voltage dynamic range. For better operation we might have to cool the APDs, but that will be no problem. The conceptual scheme of the APD readout is shown in Fig. 14, and the relevant parameters are compared with the PIN (E246) readout in Table 13.

6.3.5 Expected high-rate performance

The output from the amplifier system will be read by FADCs (65 MHz sampling with 12 bits) recently developed by the KEK electronics shop and now available for J-PARC experiments. FADCs are very powerful to resolve pulse pileup. If the photon statistics are large enough, one may in principle analyze pileup events up to the time range of the rise time of the FADC input pulse, namely the rise time of a photon signal determined by the light emission mechanism, shower development in the crystal and the light propagation/collection in the crystal. In contrast to PbWO$_4$ with the light decay time of 15 ns, we deal with longer light pulses with a 900 ns decay constant. If we apply a simple current amplifier, the relative noise is more serious. This point which might lead to pulse height uncertainty will be solved by the integration (hardware or off-line) of the signal over the comparable time window as 900 ns at the cost of pileup resolving capability. In this case

Table 14: Expected performance with the APD readout.

Parameter	Value
Max. count rate /module[8]	∼100 kHz
Max. decay particle rate from the target	∼20 M Hz
Noise level (ENL)	not known (to be tested)
Energy resolution	not known (to be tested)
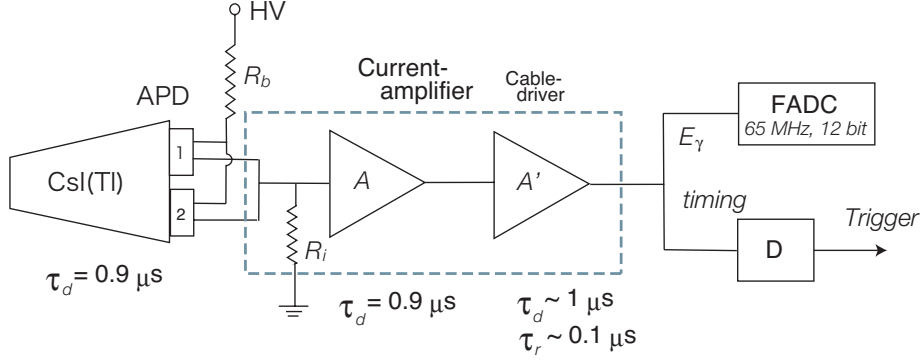
Figure 14: Readout scheme of the CsI(Tl) calorimeter using APD.

also, we may expect the pulse separation for a pileup with a time difference larger than half of the decay time (400 ns) is not spoiled. A crude estimate tells us that we may perform a counting of 0.1 MHz average rate signal in each crystal with a loss of 4%, which is marginally tolerable. Since a photon cluster involves $3 \times 3 = 9$ crystals[7], the maximum rate of 0.1MHz in each crystal corresponds to a total decay particle rate into the total solid angle of 4π of about 20 MHz, which is large enough for the proposed beam intensity of the experiment.

6.3.6 Detailed design of the readout scheme

The above mentioned conceptual design has yet to be confirmed by a prototype test. It is essential to specify the most suitable APD and to confirm its performance with respect to the gain, noise characteristics, and temperature effects, *etc.* Design of a good amplifier is also important. The overall test of the CsI(Tl) + APD + Amplifier + FADC readout should be performed as soon as possible. The schematic drawing of the readout electronics is shown in Fig. 14.

---

[7]For charged particles, the cluster size is typically one or two crystals.

6.4   Muon polarimeter

6.4.1   Implementation of an active polarimeter

The most important feature of the proposed experiment is the adoption of an active polarimeter in contrast to E246 where a passive polarimeter with a separate system of a muon stopper and positron counters was used. The advantage of this passive system was the simplicity of the analysis with the consequence of very small systematic errors associated with the analysis. The systematic cancellation scheme when the asymmetry was summed over the 12 sectors was also based on the use of positron counters as clockwise and counter-clockwise counters at the same time. However, this was done at the cost of e^+ detection acceptance and polarization analyzing power. We now aim for higher detector acceptance and higher sensitivity by introducing an active polarimeter. The suppression of the systematic errors ensured in the E246 passive polarimeter will be guaranteed by a different method. The active polarimeter should have the following functions and advantages.

- An active polarimeter determines the muon stopping position for each event, which in turn, renders the experiment free from the systematic error associated with the ambiguities in the muon stopping distribution. As the decay positron tracks are measured, the decay vertices will be determined event-by-event. In contrast to the situation in E246, where the positron signals were associated with non-negligible constant background events, the active polarimeter data will be relatively background free.

- Detection of decay positrons in all directions by a polarimeter with a large acceptance with nearly 4π solid angle. In E246 the positron counter solid angle was limited to about 10% on each side. The detector acceptance becomes 10 times larger, even though the sensitivity does not scale by this factor. The ability to measure positron emission provides the possibility to use not only the fwd/bwd pion scheme but also the $left/right$ pion scheme which was not possible in E246.

- Measurement of the positron energy as well as its emission angle. The asymmetry changes as the positron energy varies. A weighted analysis brings about a significant increase in the analyzing power resulting in higher sensitivity. It is of interest to note that this superior performance is achieved with only moderate energy resolution.

Needless to say the stopper should have a large muon collection/stopping efficiency and the ability to preserve the polarization. In order to ensure 1)preservation of muon spin polarization, in particular the P_T component, 2) to decouple stray fields such as the earth field, and 3) to facilitate the positron energy measurement, a magnetic field with a strength of at least 300 G is applied at the stopper. As in E246 the azimuthal field arrangement is adopted favoring the fwd/bwd scheme. The muon field magnet which produces a uniform field distribution on the stopper is described in next subsection.

6.4.2   Structure of the stopper

In designing the stopper (or polarimeter) structure, the following considerations are relevant.

Table 15: Main parameters of the muon stopper

Parameter	Value
Number of plates	33
Plate material	Al, Mg or other light metal alloy
Plate thickness	typically 2 mm
Plate gap	typically 8 mm
Average density	0.24 ρ_{Al}

- A large muon stopping efficiency in relatively small volume requires higher average material density, and the structure enabling clean detection of positrons without interactions such as bremsstrahlung or annihilation in flight requires a material with lower average density and the use of low mass elements.

- A structure enabling chamber arrangements. A drift chamber is the unique choice as a detector. The cell structure is primarily determined by the fine structure of the stopper. Thus, the stopper has to be designed taking this point into account.

- Optimization for the azimuthal field arrangement, namely to the fwd/bwd pion scheme. The primary choice of the polarimeter is the muon magnetic field in the azimuthal direction setting the highest priority to the fwd/bwd pion analysis. The stopper structure must be optimum for the left/right (or cw/ccw) asymmetry measurement giving this the minimum inaccuracy in the measurement.

- Internal cancellation mechanism of any local inefficiency in the positron detection. The cw/ccw inefficiency cancellation scheme of E246 is maintained by using the chamber. This scheme should work best for the cw/ccw asymmetry measurement.

Considering these conditions a parallel plate configuration will be adopted as shown in Fig. 15. The plates are made of light metal (alloy) such as Al or Mg providing the average density $1/4\rho_{Al}$. They are arranged in a parallel orientation to the spectrometer gap, namely parallel to the incident muon momentum. Due to the multiple scattering when passing through the Cu degrader in front of the polarimeter, the divergence of the incoming muon beam (in the y direction also) is significant ($\theta_0 \sim 0.1$) and there is no problem with the muon stopping. Fig. 16 shows a simulated muon stopping distribution for such parallel plates with the currently optimized dimension/material parameters. A stopping efficiency higher than 0.85 will be obtained. A drift chamber is constructed with these plates as ground potential forming cells with a size of the plate gap. Clearly, this is the best arrangement for the cw/ccw asymmetry measurement, as a single cell acts both as cw cell and a ccw cell for the two neighboring plates. The channel inefficiency cancellation works perfectly. The current parameters of the stopper are summarized in Table 16.

6.4.3   Choice of stopper material and plate thickness

Although the initial loss of the muon polarization during stopping as well as spin relaxation do not produce any serious effects in this experiment as long as they are not large, it is desirable to have a muon stopping material which preserves the polarization fully even
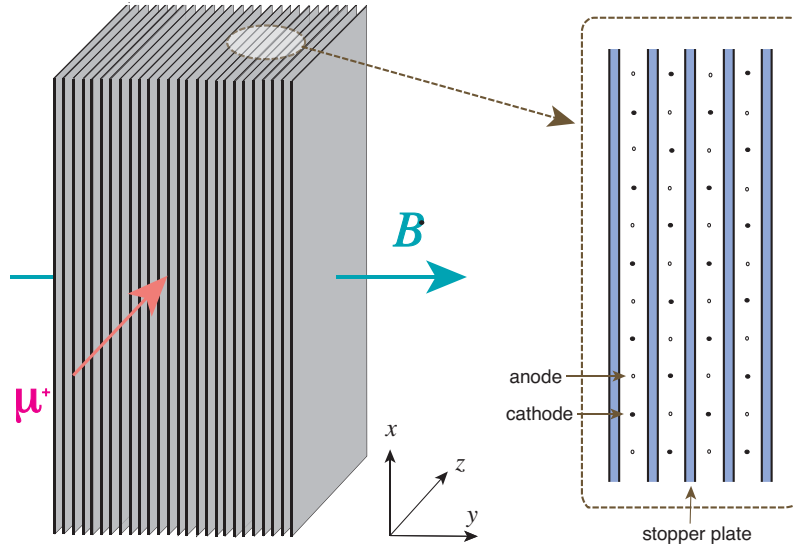
Figure 15: Muon stopper made of parallel plates which serve also as drift chamber cell structure.

under a small magnetic field at room temperature. In E246, highly-pure Al metal plates were used for this reason [80]. Magnetic impurities (Fe, Ni, *etc.*) in metals such as Al can cause significant relaxation [81]. Non-magnetic impurities of odd-A nuclei or that of Al nuclei themselves which have nuclear dipole moments also could result in depolarization when diffusing muons are trapped by the impurities, vacancies or dislocations. Those phenomena have been investigated in μSR metallurgy and are known to have only negligibly small effects for a small amount of impurities [82].

Pure Al might be not applicable for the new stopper because of its easy deformability. Contrary to the E246 stopper configuration self-weight deformation may be problematic when the plates sit horizontally, since we want to use thinner plates to suppress systematic errors. The stopper system should be fabricated precisely and assembled accurately with high precision which does not allow the self deformation of the plates. As a candidate material light metals like Be, Mg, Ti can be considered, which have a higher rigidity than Al. Some alloys of Al or Mg such as Mg(Zn) might also be candidate materials. Heavier materials like Ti have the advantage of allowing a thinner plate, but the positron interaction becomes worse. The actual selection of the material will be done after a test μSR measurement of the candidate materials.

As for the plate thickness, this will be optimized by taking into account the following conditions with the optimum average stopper density of $1/4$ ρ_{Al} given:

- Necessary gap to form the drift chamber cell, which prefers a thicker plate.

- Rigidity of the plate, which also prefers a thicker plate.

- Larger number of cells in the positron tracking, which prefers a thinner plate and gap.
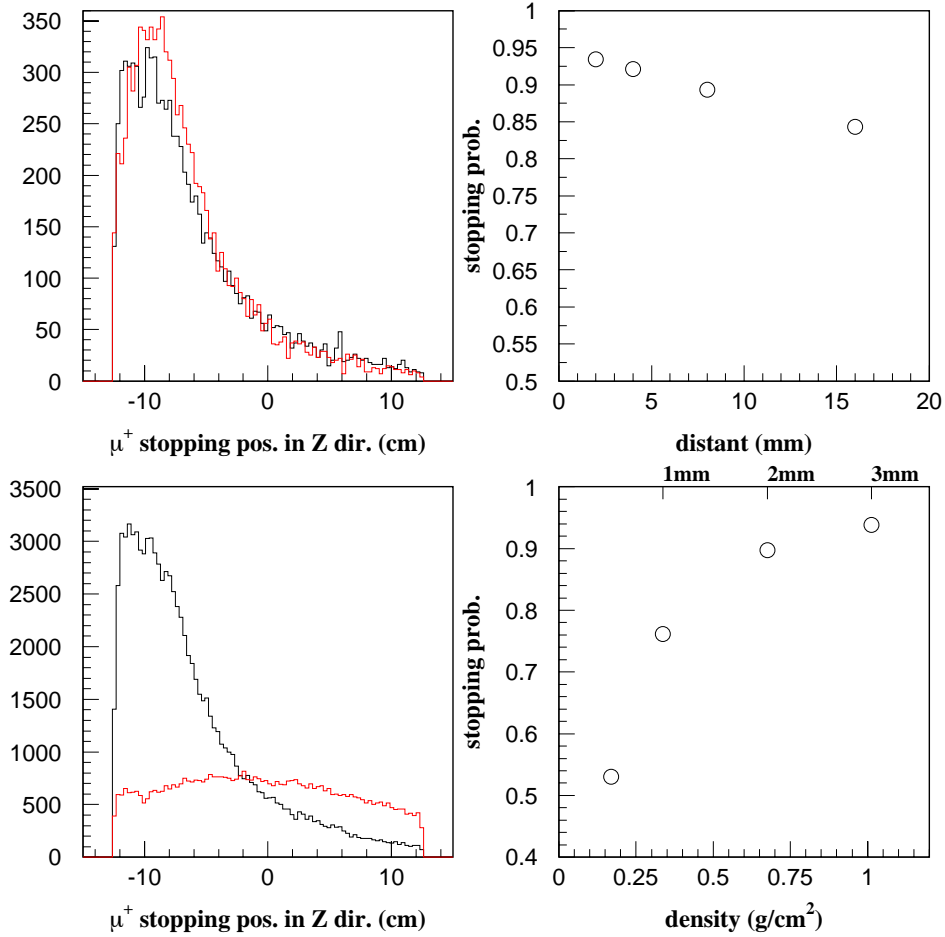
Figure 16: Muon stopping distribution (a)(c) in the parallel plate stopper calculated by a Monte Carlo simulation and stopping probability as a function of (c) plate distance (D) and (d) effective density (ρ). The muon stopping distribution are obtained with the condition of $\rho = 0.8$ in (a) for $D = 2$mm (red) and $D = 8$mm (black) and $D = 8$mm in (c) with $\rho = 0.2$ g/cm^2 (red) and $\rho = 0.8$ g/cm^2 (black). (b) and (d) are calculated by assuiming $\rho = 0.78$ g/cm^2 and $D = 8$mm, respectively.

- Smaller gradient of the muon stopping distribution in the plate, which prefers a thinner plate. A possible systematic error due to the gradient is mentioned below.

Monte Carlo studies are now in progress, but the final design must await a material choice based on the μSR measurements. As chamber gas we consider Ar-based gas or He gas. A non-negligible fraction of the muons will stop in the gas. The probability of muonium formation has been studied in noble gases. Although the data [83, 84] are somehow controversial, an application of a 300 Gauss field seems to be enough to decouple muonium. In any case, the muonium formation does not produce any spurious bias in A_T.

6.4.4   Drift chamber

As seen in Fig. 15 we prefer not to put any disturbing materials (such as electronics boards or even wire terminals) in the muon incident path, and thus the wire direction must be in the radial r direction. The basic concept of the cell structure is also shown. The coordinate along the wire is determined by charge division at both ends. The angular determination of a positron track is done with the best condition for events in the y-z plane with some degradation for the z direction. The positron measurements in the radial directions do not have good angular resolution, but it is sufficient for the present purpose. The presence of a magnetic field in the y direction not only deteriorates the r resolution but also creates some systematic shifts of r, which has to be carefully taken into account in the analysis. In first order there should be no serious bias for the A_T measurement. The detailed design of the cell structure will be chosen after detailed MC simulations, and the position resolution will be determined accordingly.

The positron energy will be analyzed using both the range in the stopper material and the trajectory curvature in the field. The tracking is done taking into account energy loss through each plate. In a design using Al plates, the total Al material widths are 13 g/cm^2 and 11 g/cm^2 for the z and y directions, respectively. These are compared with the range of e^+ of 5 g/cm^2 for 10 MeV and 15 g/cm^2 for 25 MeV. For the positrons going parallel to the field the energy measurement relies on the range. Although the stopper material alone is not thick enough to stop an e^+ from a muon near the surface, additional range stacks besides the stopper are useful to discriminate low energy e^+ with a negative asymmetry[9]. The too shallow muons cannot be analyzed in any case because the number of hit cells is not large enough. The fiducial volume and the real size of the stopper/chamber will be designed taking those factors into account. With regards to the magnetic analysis of the energy, the bending radius for a 25 MeV e^+ is 280 cm. A moderate position resolution of several 100μm will be good enough to determine the energy of positron with a 10 cm long track with an accuracy of some 20%. There is no way to install a t_0 trigger counter for the drift time analysis. This will be done by the muon incident trigger counter and the positron time measurement will be done by using a long time range high-resolution TDC.

---

[9]The installation of those range stacks may introduce a new systematic error since they have no cw/ccw cancellation capability. The detailed application method of energy information in the analysis might be an open question.
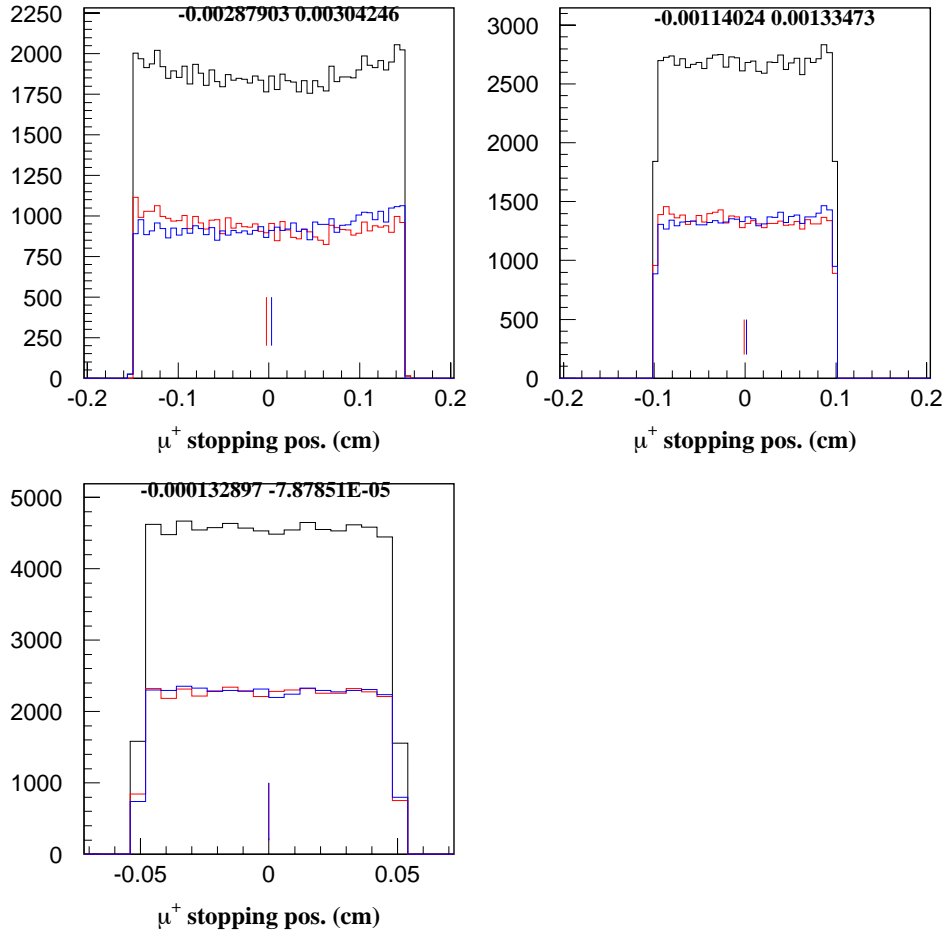
Figure 17: Muon stopping distribution across the cross-section of a plate calculated in a Monte Carlo simulation under a realistic muon incident condition. Slightly opposite gradients are seen between the two cases of left-hand side (red) and right-hand side (blue) incident muons. This difference may become a source of systematic error.

6.4.5 Analysis scheme and potential systematic errors

In principle an event-by-event analysis will be pursued by determining the decay plane with high sensitivity. The fwd/bwd scheme was adopted in E246 and the proposed experiment also places a priority on this method since 1) the field is longitudinal to P_T while P_N and P_L are precessing, and 2) asymmetry measurements are done with respect to the azimuthal direction. The stopper arrangement is optimized for this measurement. For positron emission into the radial direction for which the chamber performance is not the best, the analyzing power is zero anyway. The $left/right$ scheme, on the other hand, sets P_T in a transverse field condition, but the system is not optimized to measure the precession pattern and to determine a small phase shift from the dominant P_N precession; the position resolution of the drift chamber using charge division is not good enough.

A potential source of a systematic error in the fwd/bwd scheme is the gradient in the muon stopping distribution across the cross section of the Al plates. If it is significant a slightly different muon beam incident condition into the stopper between fwd and bwd may cause a spurious A_T when extracted as $(A_{fwd} - A_{bwd})/2$. Such a different muon incident condition may happen if the kaon stopping distribution in the target is tilted as it was in E246. Although this is a systematic which will be canceled out by the 12-gap summation, it is desirable to suppress this gradient effect as much as possible in each gap. This is the reason why thinner plates are preferable. Fig. 17 shows the stopping distribution in a 2 mm thick Al plate calculated in a realistic geometry and kinematic condition. Although one sees slightly opposite gradients for fwd and bwd, these effects are negligible.

6.5 Muon field magnet

A uniform muon field magnet with a large enough strength is essential in the proposed experiment, whereas a passive field was used by guiding and trimming the main field of the superconducting magnet in E246. The unavoidable consequence there was a non-uniform strength distribution and a curved flux distribution at the stopper. A uniform field parallel to the P_T component provides the maximum analyzing power.

Size: To accommodate the polarimeter with range stacks on both sides the parallel gap of the dipole magnet must be about 30 cm. The area is determined to produce a uniform field distribution in the stopper region.

Field strength: From the point of view of 1) spin relaxation suppression, 2) stray field decoupling, and 3) positron energy analysis, a stronger field is preferable. However, the field is limited by the interference with the toroidal magnet, in particular with its SC coils. Point 2) is regarded as the determining factor; assuming 0.3 Gauss of an unwanted component in the shielded magnet gap, a field strength of at least 300 Gauss is necessary to obtain a field alignment of 10^{-3}. Further alignment calibration is described in Section 8.

Field uniformity: The field symmetry across the median plane is important but a non-uniformity of 10^{-2} in strength as well as in the vector distribution is tolerable in the positron energy analysis. The conceptual arrangement of the magnet is shown in Fig. 19

Table 16: Main parameters of the muon field magnet

Parameter	Value
Gap×[pole face]	30 cm × [60 cm^H × 40 cm^W]
Field strength	0.03 T
Field uniformity	several % on the stopper
Alignment	a few ×10^{-3}
Number of coils	24
Magneto motive force	3.6×10^3 A·turn /coil
Total power consumption	6 kW
Cooling	indirect water cooling
Total weight	∼5 ton

for the anti-parallel field arrangement relative to the SC magnet. A parallel arrangement is also possible. The selection will be done after looking at the difference in the field uniformity and the force acting on the SC coils as calculated in a 3D field calculation. The main parameters of the total 12 magnet system are summarized in Table 16.

The main issue here is the alignment at installation. This will be done in the following order.

(1) First, the two pole pieces are assembled forming a gap with a precision of 50 μm.

(2) This gap is attached to the toroidal magnet gap with a precision of 200 μm.

(3) The neighboring magnets are then inter-connected with loose mechanical coupling.

If the force acting on the SC coils which are loosely suspended in the cryostat and not accessible from outside, exceeds a certain value it may destroy the coils. A counter balance might also be required on the upstream side of the magnet. Such a mechanical balance design will be done according to the 3D field calculations.

6.6 Electronics and data acquisition

6.6.1 Limits of the E246 system

In E246 data taking was performed primarily using the standard TKO and FASTBUS systems with some supplemental use of CAMAC systems. All the ADC and TDC data from TKO/FASTBUS modules were transferred to a memory on a VME-bus through the individual interfaces and further to a VME on-board computer for processing. The experimental data collected by a CAMAC system were also handled by the VME computer. E246 data taking was carried out with this scheme with a typical trigger rate of 200Hz and dead time of 10 to 15%, which was marginally tolerable for the KEK-PS accelerator beam intensity. For use with the higher beam intensity, however, this system has the following three bottlenecks.

- The conversion time of a TKO-ADC module is more than 150 μs because the conversion is done channel by channel for 32 inputs. This is far too long for J-PARC intensities.
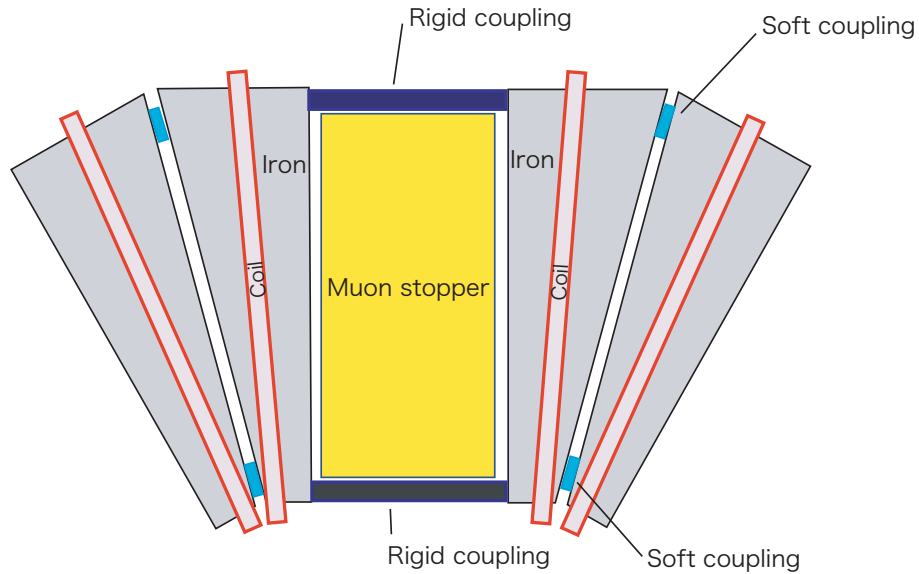
Figure 18: Schematic front view of the muon field magnet.

- Also it takes more than 200 μs to readout a TKO-TDC channel by channel for 64 inputs and transmit them to the VME bus.

- The speed of the FASTBUS master module is so slow that it takes about 1ms to read out one event.

It is also pointed out that channel extendability is very limited since all the data come together into one VME bus.

6.6.2 KEK-VME system at J-PARC

In order to overcome the above mentioned drawbacks of the old system, a much faster ADC system has to be pursued at J-PARC, possibly a system with 100 times faster speed. Currently the KEK-VME system is being developed at KEK to support this size of experiments at J-PARC. KEK-VME is based on the standard VME crate but it is equipped with a power supply for analog modules and digital signal nets for timing and trigger purposes. Readout modules are made as 9U type VME modules and called COPPER. An ADC module, for example, can acquire data using several kinds of ADC cards (FINESSE) on board with dead times of only several μs. The FADC COPPER with 65 MHz sampling and a 12-bit range has already been developed by the KEK electronics shop and they are ready for operation. This FADC will be used for the CsI(Tl) readout. A TDC COPPER/AMT-FINESSE with a resolution of 0.78 ns/bin with a dynamic range of 17 bits has also been completed and this will be used for the readout of the chambers and counters. A high-resolution TDC, a chip with 50 ps resolution and 1.8 ms range is now under development. This will be used for the TOF measurements. A multi-stop charge-sensitive ADC/ASIC is also being developed.
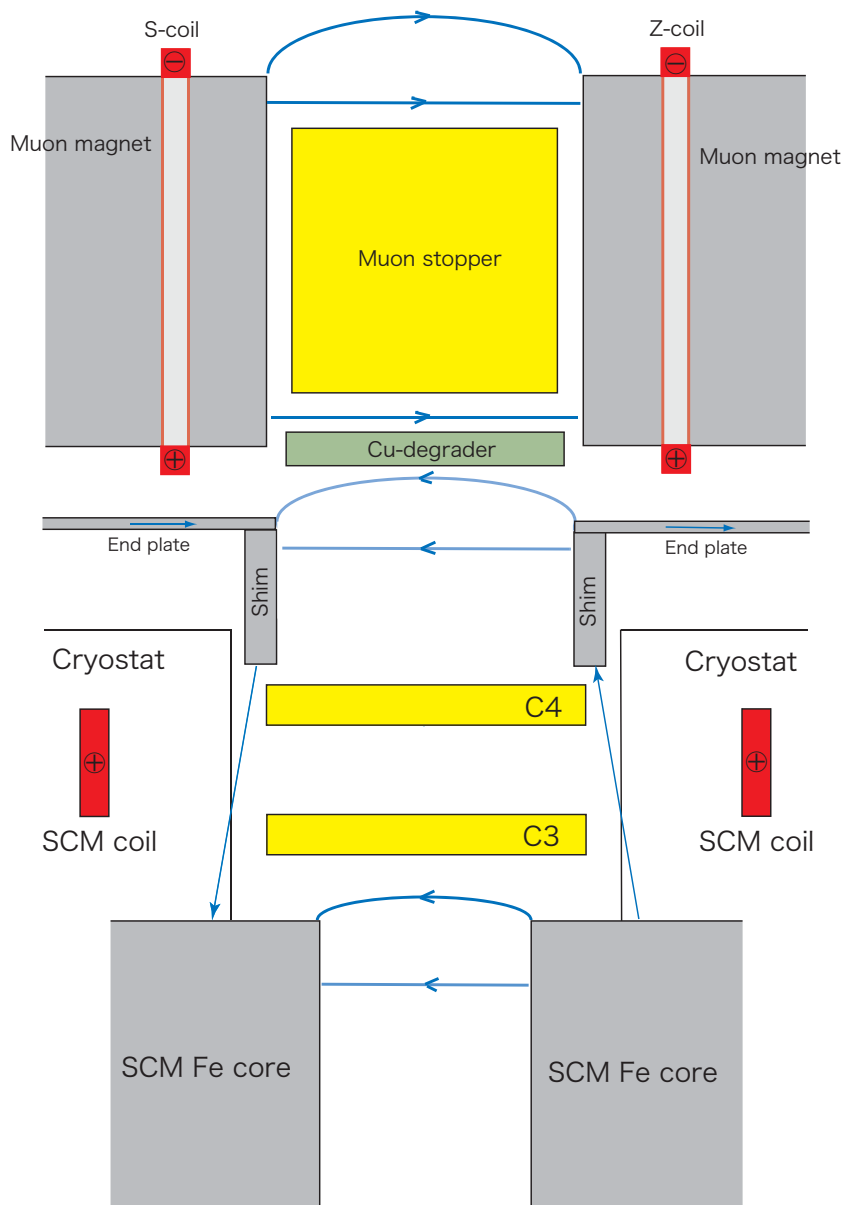
Figure 19: Schematic cross section of one sector with new muon field magnets.

Table 17: Readout devices and currently estimated number of channels

Detector element	Number of channels	COPPER/FINESSE
Counter + target	500	Q/T converter and pipeline TDC FINISSES
CsI(Tl) crystals	762	FADC FINESSE
MWPC	~ 1000	Q/T converter and pipeline TDC FINESSE
Active polarimeter	~ 3000	pipeline TDC FINESSE
TOF	48	high-resolution TDC
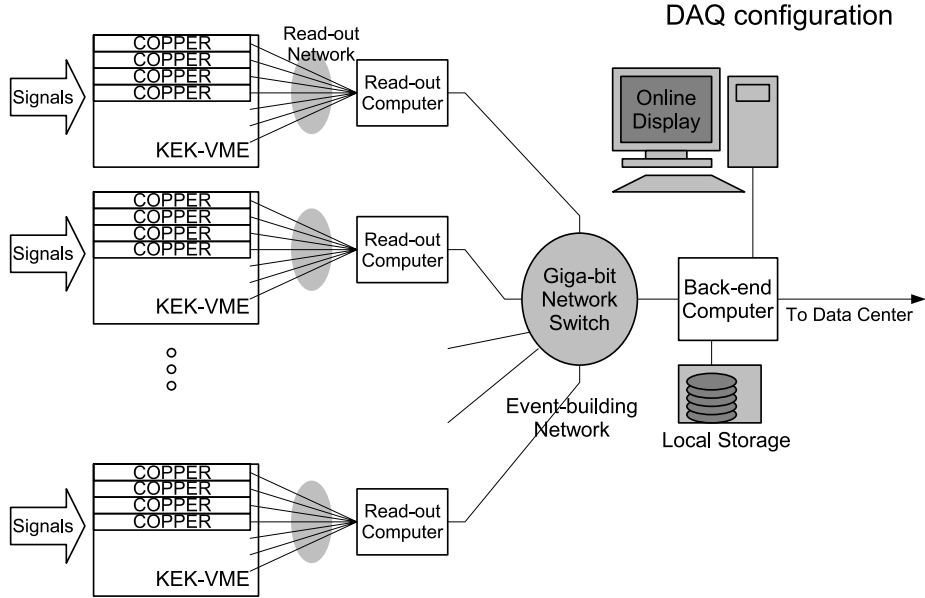
Figure 20: Data taking configuration with KEK-VME and COPPER scheme

6.6.3 Data taking in the proposed experiment

By using these COPPER and FINESSE modules and by constructing a tree scheme which also includes conventional TKO or CAMAC systems, we will be able to acquire data with a trigger rate of ~ 10 kHz and with a data flow of several ten Mbyte/s (Fig. 20). Since we estimate a trigger rate of 10 kHz, smooth data taking should be quite feasible. In Table 17 we summarize the used readout modules for each detector element with the current estimate of channel numbers.

As is shown in Fig. 20 the data acquired in COPPERs *etc.* are compiled into a data package by means of an event-builder based on the network and sent to the back-end computer in which the data are temporarily stored. Then the data are transferred to the central computer for permanent storage and analysis. Even at a trigger rate of 10 kHz, it is expected that the total dead time of the DAQ will be less than 5%. Assuming an average detector ADC/TDC occupancy of 5%, one event has a data size of 4.6 kByte and

Table 18: Summary of readout performance

Parameter	Value	Condition
One event data size	4.6 kByte	assuming 5% data occupancy in total
Acceptable trigger rate	10000/s	dead-time is less than 5%
Data flow rate	46 Mbyte/s	@ trigger rate of 10 kHz

the total data flow at 10 kHz of trigger rate is 46 Mbyte/s, which is quite feasible to handle and to store. The readout performance is briefly summarized in Table 18.

7 Beam line

7.1 Stopped K^+ beam at J-PARC

In order to perform the proposed experiment using stopped K^+, a separate low-momentum beamline with a good K/π ratio is required. In the Phase-1 experimental hall of J-PARC, however, there will be only one primary proton line, the A-line, and only one target station T1. All the secondary lines are going to be installed at this target. The construction of the beam facility is now proceeding according to the policy to accommodate the nuclear physics experiments which were nominated as "Day-1 experiments". Thus the K1.8 and K1.1 lines are most likely to be built at Day-1 (Fig. 21), and the structure of the target station and the front end of the channels are now almost fixed. Considering the high current operation of the facility, those designs with a very limited channel acceptance seem to be unique, and it will be difficult to modify the structure after starting full intensity operation. Even under such situation, we would like to pursue the possibility of a low-momentum beamline with a beam momentum of 0.8 GeV/c which is optimum for the proposed experiment (we call it hereafter K0.8.). We have found a good solution, which we propose to install. This is a branch line of the K1.1 line, and it can provide a high-quality low-momentum beam with a sufficiently good K/π ratio as described below, although the channel acceptance is determined by that of K1.1, namely by the front-end structure as shown in Fig. 22. The beam optics of this branch have been designed and documented as a J-PARC report [85]. The design of K1.1 line was reported in the series of J-PARC workshops [86].

7.2 A branch line of K1.1

The layout of a possible one stage separated 0.8 GeV/c kaon beam is shown in Fig.23. This beam coincides with the first stage of K1.1 up to B3 . The dipole magnet B3, which bends 29° counter-clockwise for the 1.1 GeV/c beam, is replaced with a 50° clockwise bend, followed by a quadrupole doublet. The important features of the 0.8 GeV/c beam are as follows.

- A vertical focus at IFY immediately after B2, where a slit defines the vertical source size for the separation stage.

- A 2 m long crossed field separator with 550 kV over a 10 cm vertical gap, which deflects pions.

- A vertical focus at MS1, where a vertical slit, the mass slit, removes most of the deflected pions.

- A dispersion free horizontal focus at HFOC, that plays a crucial role for removing any remaining pions.

- A final focus, 1.5 m downstream of the last quadrupole.

- The length of the beam is 19.0 m.

- A momentum acceptance of 4.6 percent $\Delta p/p$ FWHM and 7.0 percent $\Delta p/p$ FWQ(quarter)M.
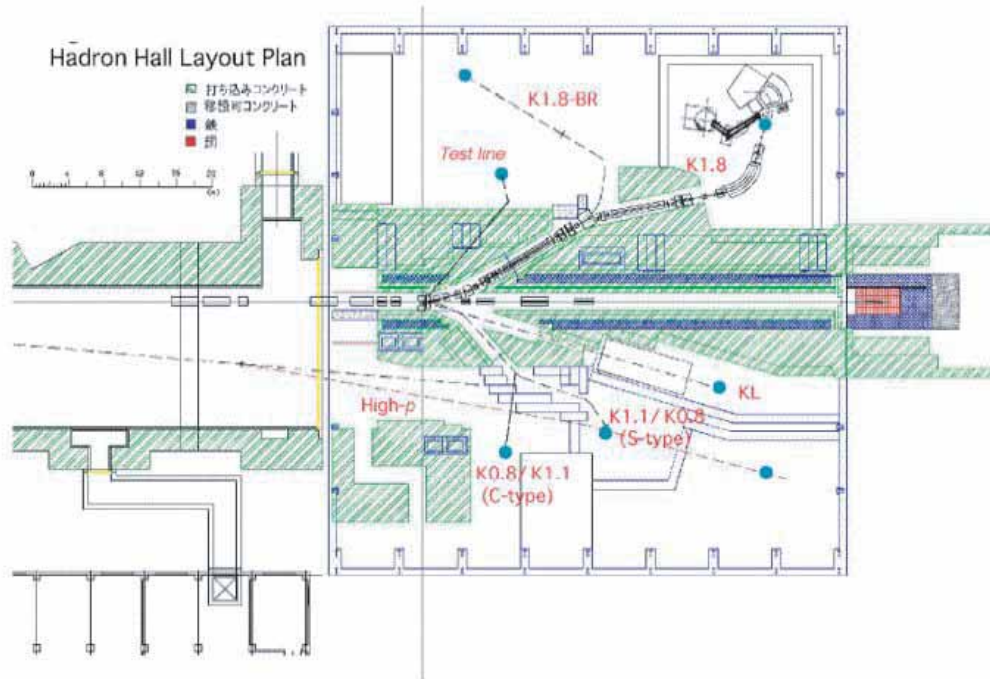
Figure 21: Layout of beamlines in the Phase-1 experimental hall

- A total angle momentum acceptance of about 6.0 to 6.5 msr.percent $\Delta p/p$, which compares to 48 msr% $\Delta p/p$ for the LESB3 beam at Brookhaven.

- A final full spot size smaller than 2.5 cm by 2.5 cm.

- A pion contamination less than half the intensity of the kaon beam.

7.3   Optics of the 0.8 GeV/c beam

The first order beam envelopes are shown in Fig. 24. The second order program REVMOC, similar to TURTLE, was used to investigate the effects of slit scattering, and cloud pions. The higher order program ZGOUBI traces particles through the magnets with realistic extended fringe field distributions. This is done for pions and kaons which are produced directly in the production target, and do not suffer slit scattering. The pion rejection is crucially dependent on higher order corrections for the vertical beam spot at the mass slit MS1. This is done with two sextupoles and one octupole, which limit the extent of the tail of the pion spot. On the basis of comparisons with beamline LESB3 at Brookhaven it can be deduced that there will be about 500 times as many pions as kaons at the final focus if the separator is turned off. Therefore, even a 0.2 percent transmission of pions will give as many pions as kaons at the final focus. That is not acceptable. The vertical beam spot at
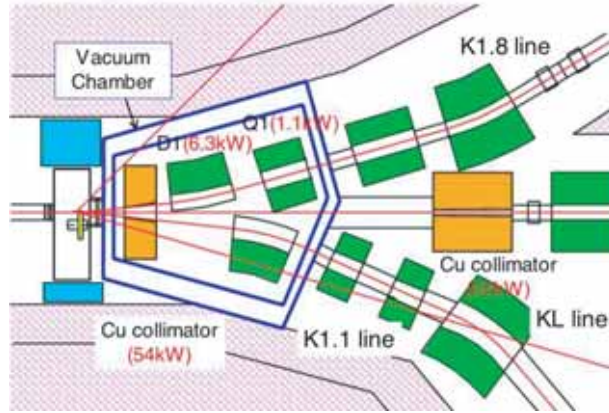
Figure 22: Almost fixed design of the target station T1 and front-end of secondary lines
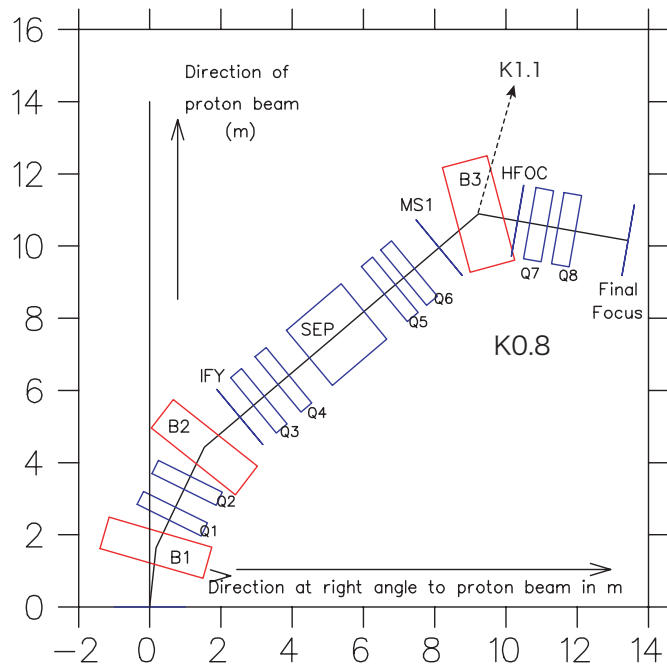
Figure 23: Layout of the 0.8 GeV/c beam.
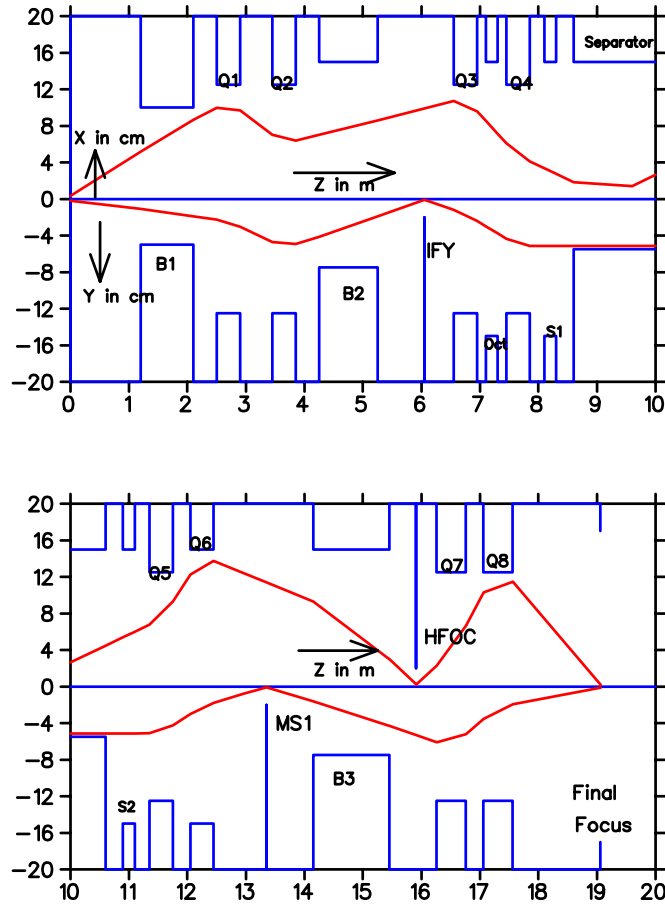
Figure 24: First order beam envelopes for the central momentum of the 0.8 GeV/c beam from TRANSPORT. The initial horizontal angle is 43 mr, the vertical angle is 9 mr. X is 3.5 mm and Y is 2 mm. All numbers indicate half widths.

S1 is shown in Fig. 25. The pion peak is 5.5 mm separated from the kaon peak. The blue peak assumes that there are an equal number of pions and kaons. The green curve takes into account that there are in fact 500 times as many pions as kaons. The separation is not perfect, but fortunately it is possible to close the horizontal slit at HFOC after B3 to a full width of 1.6 cm to eliminate most of the remaining pions at the expense of a few percent of the kaon intensity. Fig. 26 shows the momentum distribution for the kaons. It does not depend much on the slit widths. The FWHM is 4.6 percent $\Delta p/p$ and the FWQM is 7.0 percent $\Delta p/p$. Fig. 27 shows the final beam spot. The vertical beamspot is 0.52 cm FWHM and 1.04 cm FWQM. The horizontal beam spot has 0.47 cm FWHM and 0.78 cm FWQM. If the horizontal slit at HFOC is closed to 1.2 cm full width, the tails on the final horizontal spot are reduced.
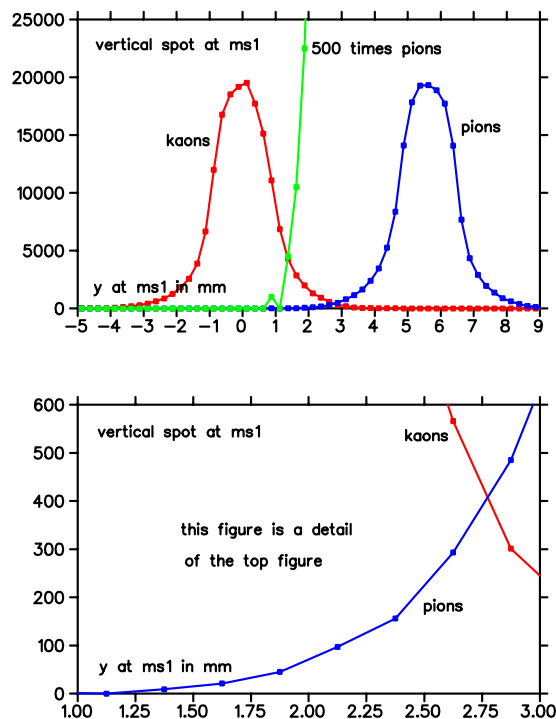
Figure 25: ZGOUBI result for the 0.8 GeV/c beam. The vertical beam spot at MS1 for kaons and pions. The green line shows the pion distribution multiplied by 500.

7.4 Removal of pion contamination

7.4.1 Cloud pions

The 0.8 GeV/c beam has only one stage of separation. An important cause of the pion contamination in a single stage separated beam is the presence of a so called cloud of pions near the production target due to the decay of neutral kaons, which presents a large vertical and horizontal source to the beam line. In a two stage separated beam the first mass slit has two functions. It removes most of the pions directly produced by the proton beam, and it defines a small source of cloud pions for the second stage. In a single stage separated beam, the second function can also be performed by creating a vertical focus in the beginning of the beam line before the separation takes place. The vertical focus at IFY can be used for that. On the basis of the measured performance of beamline LESB1 at Brookhaven, the predecessor of LESB3, and from calculations of the decay of neutral kaons it can be concluded that the cloud pion contamination in a 19 m long separated beam with only one mass slit closed is less than 5 times the kaon intensity.

Table 19 lists the cloud pion intensity as a function of the slit apertures. The REVMOC calculations started with a large source size at the production target. For the case with the mass slit MS1 closed to 5 mm and the other slits open, the transmitted pion intensity is arbitrarily set to 100 percent. Closing IFY reduces the transmission considerably. A

Table 19: Cloud pions as function of slits for the 0.8 GeV/c beam

IFY (mm)	MS1 (mm)	HFOC (cm)	N_π (%)
open	5	open	100.0
6	5	open	6.3
6	4	open	2.5
5	4	open	1.1
6	5	1.6	2.1
5	4	1.6	0.2
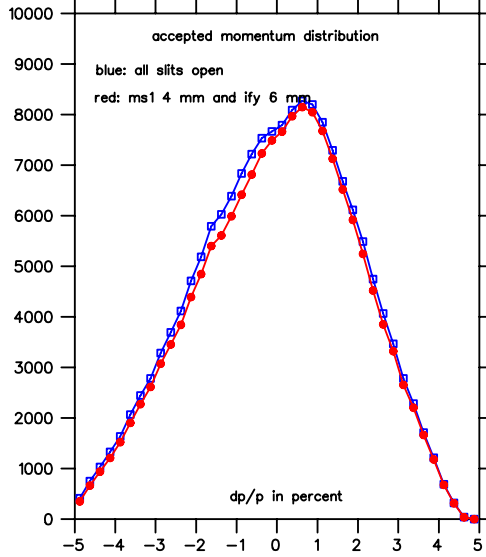
Figure 26: ZGOUBI result of the accepted momentum distribution for the 0.8 GeV/c beam.

combination of MS1 and IFY reduces the contamination to the few percent level. In addition, the horizontal slit at HFOC can be adjusted. In this way it is possible to reduce the cloud pion contamination by 2 orders of magnitude. Therefore, the cloud pion contamination will not be a problem.

7.4.2 Slit-scattered pions

In the ZGOUBI calculations mathematical slits of zero length are used both at IFY and at MS1. However, in reality the vertical slits at IFY and MS1 are 30 cm long, divided into three parts. The middle 10 cm has a flat surface. The first and last 10 cm have tapered surfaces. The taper angle is 20 mr at IFY and 15 mr at MS1. Calculations were done for slit scattering using REVMOC. Table 20 shows for a 4 mm full square width vertical source the number of pions and kaons arriving at the final focus as a function of the slit
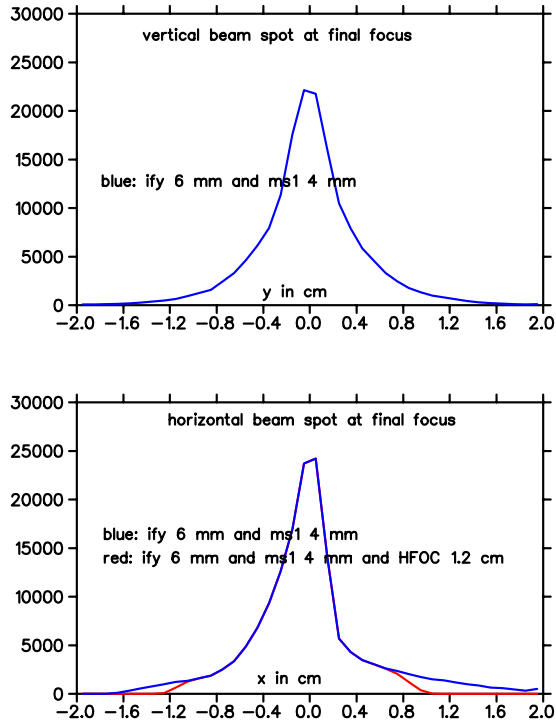
Figure 27: ZGOUBI result for the 0.8 GeV/c beam. Vertical and horizontal beam spots at the final focus.

widths. All calculations were started with the same number of pions and kaons. However, to obtain the actual π/K ratio the number of pions has to be multiplied by 500. The top part of the table shows that closing only IFY and MS1 is not sufficient to get the π/K ratio small. Slit scattering is obviously a major source of pion contamination. Closing MS1 is the most effective. The second part of the table shows a drastic improvement in the π/K ratio when the horizontal slit at HFOC is closed to a full width of 1.6 cm, at the expense of a minor amount of kaon flux. Figure 28 helps to understand the importance of HFOC. It shows the kaon and pion distributions at HFOC, on a logarithmic scale at the top and after renormaliztion on a normal scale at the bottom. The green line is the pion distribution multiplied by 500. It is clear that closing the horizontal slit to ±0.8 cm gives a huge reduction in the pion contamination.

7.5 K^+ intensity

As shown above, the quality of the 0.8 GeV/c separated kaon beam [K0.8], with a single stage of separation with a π^+/K ratio of less than 0.5, is very good for our purposes. This is achieved by the existence of a vertical focus IFY in K1.1 and also by the horizontal focus HFOC additionally designed for the K0.8 branch. The acceptance of K0.8 is, however, determined primarily by the upstream acceptance of K1.1, namely by the distance of the first focusing element from the target, which cannot be shorter. The calculated acceptance

66

Table 20: Kaon acceptance and pion contamination due to slit scattering as function of slit apertures for a 4 mm high vertical source

IFY (mm)	MS1 (mm)	HFOC (cm)	π^+/K^+	Acceptance (msr·%)
6	5	open	2.50	6.8
5	5	open	2.27	6.4
5	4	open	1.30	6.3
6	5	1.6	0.30	6.7
5	5	1.6	0.30	6.3
5	4	1.6	0.16	6.1
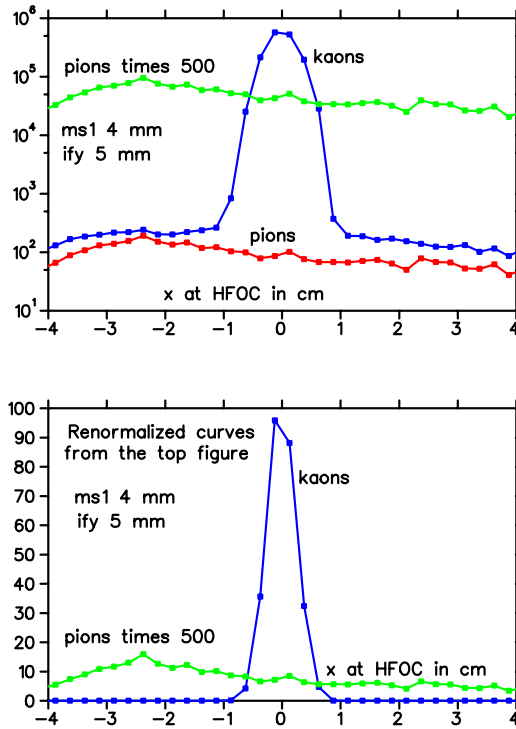
Figure 28: REVMOC result for the 0.8 GeV/c beam. Horizontal beam spots at HFOC for kaons and pions, logarithmic scale at the top and renormalized scale at the bottom. The pion distribution is wide due to scattering in the 30 cm long slits at IFY and MS1.

67

Table 21: Main parameters of the K0.8 beam

Parameter	Value
Momentum	800 MeV/c
Momentum bite	$\pm 2.5\%$
Channel length	19 m
Channel acceptance	6.5 msr%$\Delta p/p$
π^+/K^+ ratio	< 0.5
K^+ intensity	3×10^6 @ 9μA proton beam
Beam spot	$H = \pm 0.3\,(FWHM)$cm, $V = \pm 0.4\,(FWHM)$cm
	$H = \pm 1.6\,(total)$cm, $V = \pm 1.6\,(total)$cm
Dispersion at final focus	achromatic

of $\sim 6\%\cdot$msr is smaller by a factor of 8 than the C4(LESBIII) line at BNL-AGS of the nearly same length for 0.8 GeV/c operation. Although there might be some ambiguity due to the detailed target structure, we can roughly estimate the K^+ intensity to be 2×10^6/s at $I_p = 5.4 \times 10^{13}$/s (9μA) and $E_p = 30$ GeV by scaling the known LESBIII intensity at $E_p = 24$ GeV. The main parameters of K0.8 are summarized in Table 21.

Table 22: Two field maps

Map	Method	Deduce parameters	Precision
Toroid	3D calculation	Momentum	∼chamber resolution
Muon field	Hall probe measurement	δ_r, δ_z	∼1mr

8   Experimental method

8.1   Field measurement

The spectrometer field map will be necessary only for charged particle tracking purpose and its goal will be a good trajectory reconstruction with high momentum resolution. In E246 a map calculated with the 3D code TOSCA was used to provide the best momentum resolution rather than a measured one. This map can be used further but the exit volume which is affected by the new muon field magnet must be recalculated. This calculation will be necessary also for estimating the imbalance forces acting on the superconducting coils. The momentum resolution will be measured by the $K_{\pi 2}$ and $K_{\mu 2}$ monochromatic peaks using events with the K^+ stopping near the target surface with the condition of no energy loss.

More importantly the muon fields have to be mapped for all 12 gaps of the new magnet system. The determination of the field vector distribution will be performed in an actual high-precision measurement as was done in E246 by means of the "four Euler angle" technique of a 3D Hall element [64]. In this method the flux direction is determined with an accuracy of 1 mr regardless of the uncertainty of the planar alignment of the Hall element in the probe. This accuracy of 1mr will be the best value that one can obtain using a conventional Hall probe. Any further calibration of the flux angle has to rely on data using $K_{\pi 2}$-dif as described next. The mapping is performed for each sector in the local coordinate frame with a reference to the magnet gap. A new probe-scanning device will be constructed. The installation of the device is done with a good angular alignment of 1mr using a laser technique *etc*. Measurements exciting the superconducting toroidal magnet will take several months extending over a fairly large fraction of the preparation period. One has to work in the experimental area. The measured field distribution is fitted to a calculated ideal field to deduce the two relevant rotation parameters of δ_r and δ_z around the r and z axes, respectively, in each gap coordinate system with a precision of 1mr. The absolute strength is also determined with a precision of ~ 0.1Gauss.

8.2   Cabibration of alignments

8.2.1   Required alignments and methods

The major sources of systematic errors will be the misalignments of the detector elements which can induce the admixture of the large in-plane polarization into the azimuthal component. Therefore, the alignment is a determining factor of this high precision experiment. E246 required a suppression of such systematic errors only down to the 10^{-3} level; therefore an alignment with a precision of roughly 10^{-3} was good enough and this could be
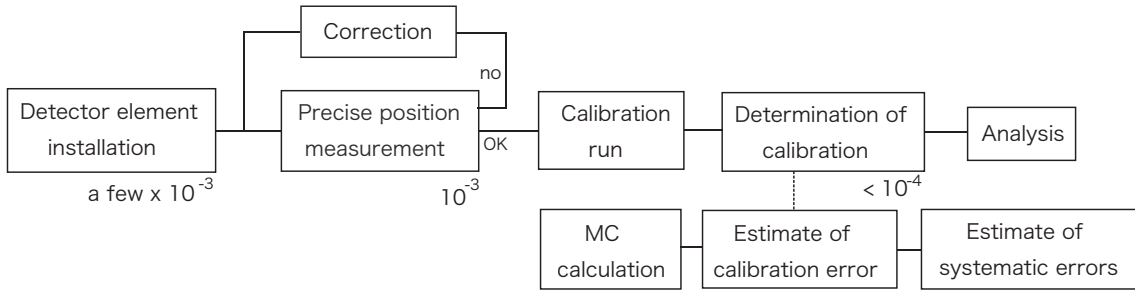
69

Figure 29: General alignment method

attained by actual position measurements. However, this kind of position measurement does not work to achieve an alignment to the 10^{-4} level; thus, we have to rely upon alignments using data. In the following, the step-by-step alignment procedures are described. The most difficult one is the alignment of the magnetic field for its rotation about the z-axis. We will have to employ decay-in-flight pions from $K_{\pi 2}$. The general scheme of alignment is schematically shown in Fig.29.

8.2.2 Primary reference frame

The Toroidal Magnet is the primary reference frame. Each iron core of the magnet was manufactured with an accuracy of about 50μm. After combining the core with a superconducting coil to form one sector, the assembly of the entire system was carefully performed ensuring a rotational symmetry of 30 degrees and uniform gaps. The 12 median planes of the gaps converge to a virtual central axis with an accuracy of 0.3 mm and the difference of diameters in the horizontal and vertical directions is less than 2 mm over a diameter of 4 m. This global symmetry was important in E246 in which the total cw/ccw scheme was adopted for positron asymmetry measurement and in which the kaon stopping had an asymmetric distribution in the target due to beam momentum dispersion. We took advantage of systematics cancellation by means of the global rotational symmetry of the magnet. Now this becomes less important with the introduction of the active polarimeter and with the possibility of symmetrization of the kaon stopping distribution thanks to much higher stopping kaon intensity. Thus, the 12 gaps are regarded as independent coordinate systems. The alignments of the detector elements are done with respect to each gap coordinate.

8.2.3 Tracking system

Only the alignment of the y positions of the chambers in the gap frame and the target (x, y) position in the global frame are relevant. A misalignment of an element would cause an offset in the vector of the outgoing muon momentum. This results primarily in an offset of P_L giving rise to a small y component, namely a spurious P_T component. This is typically 10^{-3}, corresponding to the misalignment, but this spurious P_T is common for fwd and bwd, and hence rather harmless thanks to cancellation. A spurious P_T from P_N, if any, would be troublesome since it is not canceling. However, the tilt of P_N is caused mainly by the existence of edge focusing due to the fringing field. Without the fringing

70
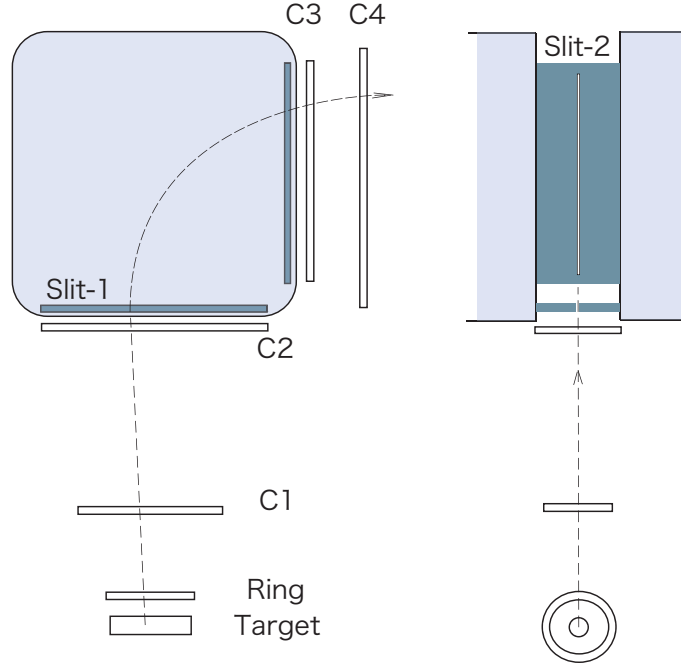
Figure 30: Tracking system alignment

field the effect is higher order and at most 10^{-6}. A very safe assumption of 10% for the edge focusing gives an estimate of $10^{-3} \times 0.1 = 10^{-4}$, which might be critical.

The alignment is done as follows as special calibration runs:

(1) One places two median plane slits at the entrance (just behind C2) and at the exit (just in front of C3) of the gap. The slits are well aligned to the surface of the magnet pole-faces with an accuracy of better than 0.1mm. Then one measures the charged particle tracks (of e.g. $K_{\mu 3}$ or $K_{\pi 2}$) from sufficiently large kaon stopping distribution.

(2) From the centroids of the hit patterns of the C2 and C3 chambers, one obtains zero point calibrations $y_0(r)$ as a function of r for each of those chambers. Since the chamber y resolution is 2mm determined by the anode wire spacing, the width of the slits have to be optimized for this spacing. It is also important that the anode efficiencies should be equal for the corresponding wires in the central regions and the kaon stopping distribution must be uniform in the region of interest.

(3) The selection of median plane events with cuts on C2 and C3 further determines the y calibration $y_0(r(or z))$ of C1, C4 and the target in a straightforward way. The measurement of the 12 gaps thus gives the global alignment $(x_0(z), y_0(z))$ of the target.

8.2.4   CsI(Tl) barrel

The alignment of the CsI(Tl) barrel is performed using the reference frame of the tracking system thus determined. The back-to-back nature of the π^+ and π^0 from $K_{\pi 2}$ is fully used (see Fig.31). For each gap one measures an offset from $180°$ of the back-to-back angle. The 12 azimuthal offset angles $\delta\phi_i$ determine the rotation of the barrel $\Delta\phi$ and parallel shift Δx and Δy in the global (x, y) plane, and the 12 polar offset angles $\delta\theta_i$ determine the parallel shift Δz and the two tilt angles of $\Delta\varphi$ and $\Delta\psi$. For clear selection of $K_{\pi 2}$ events one can use only the events with two photons hitting crystals far from the muon holes as was intensively studied in E246. Once the global alignment of the barrel unit is done, local misalignments of crystal mounting can be checked and corrected partially in terms of the "decay plane rotation" in the first order approximation. Such misalignments are regarded as equivalent to a non-uniform distribution of detector inefficiency and would reflect in the distribution of the decay plane. It is worthwhile to assess various types of systematics that they may induce and determine the necessary corrections.

(1) $\Delta\phi$ admixes P_N, but it is cancelling between fwd and bwd. Thus, it would be harmless.

(2) Δx and Δy induces a P_N admixture when looking at one gap, but the cancellation by the 12 gap summation is effective. Furthermore, the fwd/bwd cancellation additionally suppresses any residual effect. Thus, it is even less significant than (1) and (3).

(3) One relies on the 12 gap cancellation for $\Delta\varphi$ and $\Delta\psi$ which also generate a P_N admixture when looking at one gap. Here, the fwd/bwd cancelling scheme does not work.

   Although these alignments are cancelling by the 12-gap summation and/or fwd-bwd subtraction, it is preferable to perform the above mentioned calibration using a $K_{\pi 2}$ special calibration run.

8.2.5   Active polarimeter and magnetic field

The alignment of a y parallel shift is straightforward just by extending the tracking system. And this shift, even if it remains, does not contribute to a positron asymmetry. Therefore, it is harmless. There are two misalignments to be considered, the rotation about the r axis and the rotation about the z axis. In order to measure those alignments a pure longitudinal polarization P_L can be used. There are two methods to create P_L: one is to take $K_{\mu 2}$ muons by adjusting the magnet field to a higher momentum and the other is to use $K_{\mu 3}$ events integrating all over the π^0 directions.

Rotation of the polarimeter about the r axis, ϵ_r: The longitudinal polarization of stopped muons in the stopper is pointing in the z direction at $t = 0$ and it will start to precess. The L/R asymmetry observed by the active polarimeter shows an oscillation pattern like Fig. 32a without bias. This pattern determines ϵ_r. Although the precession phase is opposite by $180°$ for P_N^{fwd} and P_N^{bwd}, this systematic could be not be removed for the time-integrated asymmetry, but it is rather harmless.
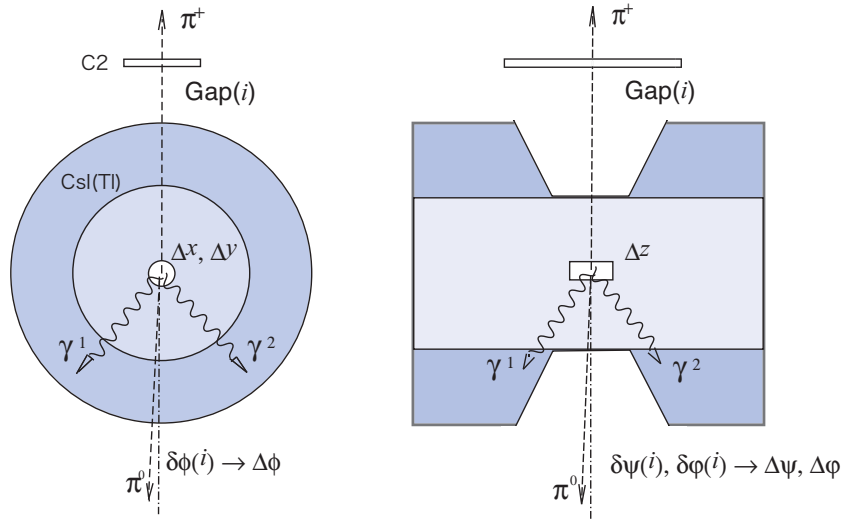
Figure 31: CsI(Tl) alignment

Rotation of the polarimeter about the z axis, ϵ_z: In the same manner, P_L in the stopper shows the precession pattern of Fig. 32b. Since the phase is different by $\pi/2$ between ϵ_r and ϵ_z they can be separated. The prerequisite in these studies is of course a well aligned magnetic field perpendicular to the initial P_L. In this case the precession phase also has a 180° difference for P_N^{fwd} and P_N^{bwd}, but it is cancelling in the time-integrated asymmetry as in the case of ϵ_r.

Rotation of the magnetic field about the r axis, δ_r: There are also two rotation angles relevant for P_N admixture to P_T, namely the rotation **B** about the r axis δ_r and the rotation δ_z about the z axis. The asymmetry pattern is shown in Fig.32c,d. Although the precession phase is same as for ϵ_r, it can be separated because of the bias. Moreover, the fwd/bwd cancellation mechanism works for P_N in this case, making this systematic a rather harmless one.

Monte Carlo simulations concerning the feasibility of the alignment calibrations are now progressing (Fig. 33).

Rotation of the magnetic field about the z axis, δ_z: The precession pattern of P_L is shown in Fig. 32d. Unfortunately there is no way to separate this effect from that of ϵ_z because of the same phase with no bias. Furthermore, there is no cancellation between fwd and bwd for the time-integrated asymmetry. Namely, $<P_N>^{fwd} - <P_N>^{bwd} \neq 0$ making this misalignment most serious. It is therefore necessary to employ a polarization configuration other than P_L. The only possibility to measure δ_z independent of other misalignment is to prepare a pure polarization P_r in the r direction (Fig. 34). However, it is not possible to make this polarization from $K_{\mu3}$ nor $K_{\mu2}$. P_N in the $K_{\mu3}$ decay might be accompanied by P_T with the y component which we are now going to detect.

It is, however, possible to use the muons of $K_{\pi2}$ decay-in-flight for this purpose. The transverse decay of pions in the CM system with a muon emitted in the gap median plane
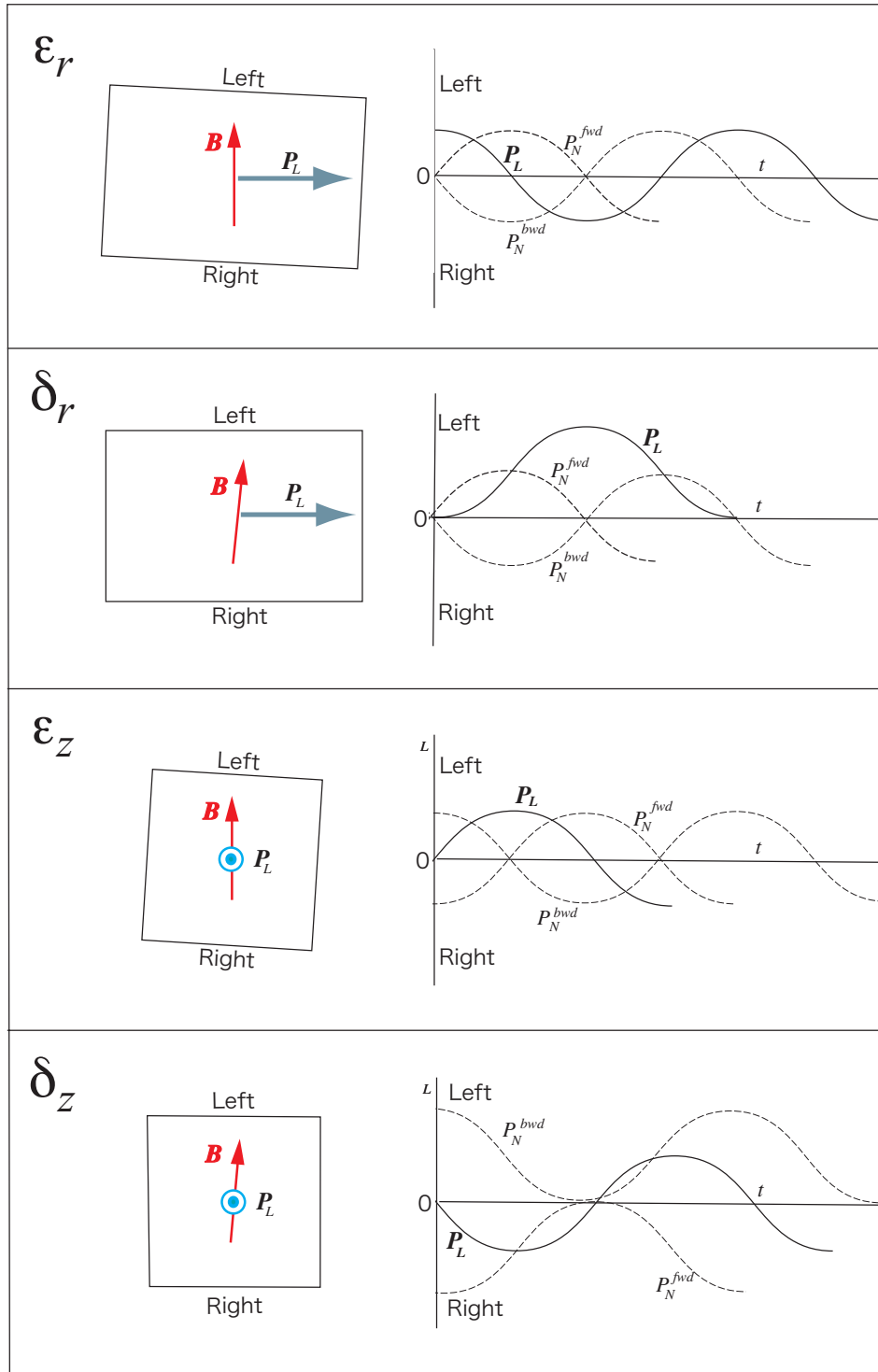
Figure 32: Calibration of polarimeter alignment and magnetic field direction. The longitudinal polarization P_L is utilized. Solid line show the asymmetry observed when the individual misalignment is present. Dotted lines are the spurious asymmetry in the main measurement due to P_N admixture. The time-integrated asymmetry is not fwd/bwd cancelling only for δ_z.
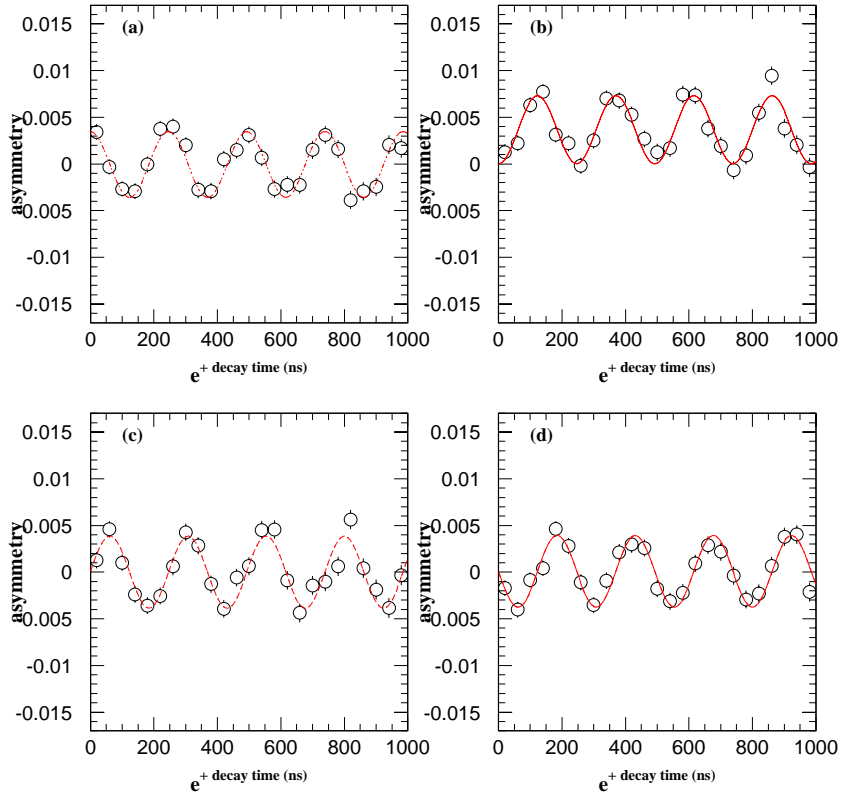
Figure 33: Example of MC studies on alignment calibration. Misalignments of (a) $\epsilon_r = 1°$, (b) $\epsilon_z = 1°$, (c) $\delta_r = 1°$ and (d) $\delta_z = 1°$ were artificially put in the simulation. The asymmetry of normalized positron time spectra are shown fitted with red expected curves.
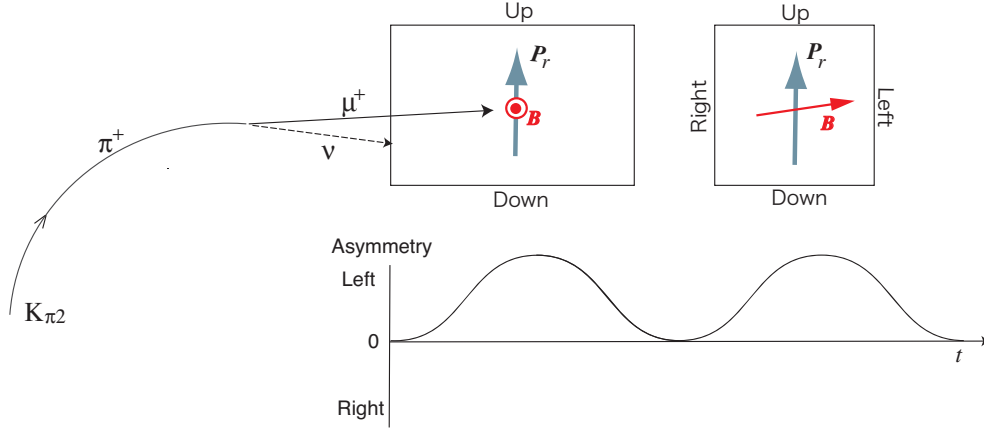
Figure 34: Calibration of magnetic field alignment using $K_{\pi 2}^+$-dif muons. Polarization with a pure radial component is generated in the stopper. The asymmetry measurement for this polarization yields Eq.30.

produces a polarization component of stopped muons in the r direction. The precession pattern of this polarization determines δ_z. For $K_{\pi 2}$ identification we rely again on the energy spectrum E_{π^0} of the π^0 of so-called normal events with two photons hitting the crystals away from the muon hole regions. We will be able to see a clear peak at $E_{\pi^0} = 110$ MeV. For the charged particle energies, one observes only an insignificant change in the momentum from the initial 205 MeV/c of the pions. However, the new high position resolution tracking system should be able to see a kink at the decay vertex, thus enabling the identification of such events (Fig. 34).

In general, the four misalignments are present simultaneously. In order to deduce all the values two $left/right$ asymmetry measurements will be performed using the $K_{\mu 3}$ longitudinal polarization P_L, and the radial polarization from $K_{\pi 2}$ decay-in-flight $P(P_r)$. They should provide;

$$A(P_L) = \epsilon_r \cos \omega t + \delta_r (1 - \cos \omega t) + (\epsilon_z - \delta_z) \sin \omega t$$
$$A(P_r) = -\epsilon_z \cos \omega t + (\epsilon_r - \delta_r) \sin \omega t - \delta_z (1 - \cos \omega t). \tag{30}$$

From fitting, ϵ_r, ϵ_z, δ_r and δ_z are uniquely determined.

8.3 Trigger and data taking

8.3.1 Trigger condition and rate

The event trigger for data taking is not very different from E246. The necessary requirements are:

- Incident beam particle is a kaon. This condition is supplied by the beam Cherenkov counter. A signal (C_K) is generated when the multiplicity of the kaon ring PMT exceeds a certain number. The utility of this trigger condition was established in E246.

Table 23: Reduction of trigger rate compared with E246

Step	Condition	E246 @$10^5 K^+$/s	This proposal@$3 \times 10^6 K^+$/s
(1)	C_K	1.0×10^5	3.0×10^6
(2)	$C_K \cdot Fid$	2.0×10^4	9.0×10^5
(3)	$C_K \cdot Fid \cdot TOF2$	1.2×10^3	6.0×10^4
(4)	$C_K \cdot Fid \cdot TOF2 \cdot Pol$	6.0×10^2	2.4×10^4
(5)	$C_K \cdot Fid \cdot TOF2 \cdot Pol \cdot CsI$	4.8×10^2	1.9×10^4
(6)	$C_K \cdot Fid \cdot TOF2 \cdot Pol \cdot CsI \cdot e^+$	0.5×10^2	$-$
(7)	Step (5)$\otimes K_{\pi 2}$ rejection	$-$	1.0×10^4

- Decay of a stopped kaon in the target by emitting a charged particle. Since the target fiber length is just the length of the kaon stopping distribution, the necessary signal (Fid) is the fiducial counter signal from a charged decay particle after a certain time of kaon decay. This is the same as in E246. (Fid is used for TOF measurement also.)

- Charged particle passing through the spectrometer gap ($TOF2$). This might be redundant in the presence of a signal of the Pol-trigger counter, but it will help purify the trigger.

- Traversal of a muon in the polarimeter is signaled by the polarimeter trigger counter (Pol).

- Detection of at least one photon in the CsI(Tl) calorimeter. The signal CsI is generated when there is an energy deposit of more than 5 MeV in one of the crystals.

In E246, decay positrons were included in the trigger. For an active polarimeter with nearly 4π acceptance, we may not require this condition. The rate reduction in each step of (Eq. 31) is summarized in Table 23 at the expected beam intensity of 3×10^6/s compared with those of E246. The multiple condition of $C_K \cdot Fid \cdot TOF2 \cdot Pol \cdot \gamma$ corresponds to a trigger rate of 1.9×10^4/s. This rate might still be too large to handle even with the new data taking system using "COPPER and KEK-VME". Because the main part (about 3/4) of this rate comes from the $K_{\pi 2}$ background channel, it is necessary to suppress those events. A quick look-up of charged particle momentum using chamber information is effective. The events with a rough-estimated momentum larger than 200 MeV/c e.g. are regarded as $K_{\pi 2}$ and are rejected. The judgment is done semi-hardware-wise in several 100 ns and applied as a kind of second level trigger.

Thus, the trigger condition is expressed as

$$Trigger = C_K \cdot Fid \cdot TOF2 \cdot Pol \cdot \gamma \cdot \bar{K}_{\pi 2}. \tag{31}$$

8.3.2 $K_{\mu 3}$ event rate

The kaon stopping rate in the target is estimated as 9.0×10^5/s for the incident beam intensity of 3×10^6/s. The assumed stopping efficiency of 30% is a conservative estimate compared with that of E246 which was experimentally determined to be 39%, taking into

Table 24: Rate estimates for K^+ beam particles of 3×10^6/s

Condition	Rate /s	Comment
K^+ beam incident	3×10^6	@$I_p = 9\mu$A
K^+ beam stop	9.0×10^5	$\varepsilon_{stop} = 0.30$
$K_{\mu3}$ decay	2.9×10^4	$BR = 0.032$
$K_{\mu3}$ in polarimeter	690	$Acc = 0.024$
$K_{\mu3}$ in pol. with 2γ detection	240	$\varepsilon_{2\gamma} = 0.35$
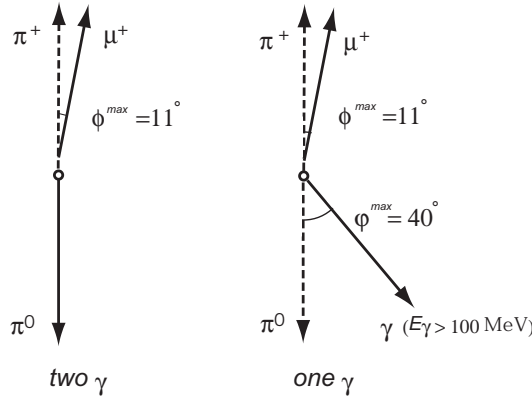
Figure 35: Angular ranges of $K_{\pi2}$-dif back-to-back condition for 2γ events compared with 1γ events.

account the smaller diameter of the target. The $K_{\mu3}$ branching ratio of 3.2% and the μ^+ collection efficiency of 2.4% (the stopping efficiency is 80%) provides the $K_{\mu3}$ μ^+ rate of 690/s. For the CsI(Tl) analysis we will use only the 2γ events with a detection efficiency of 35%. Thus we may expect 240/s $K_{\mu3}$ events with e^+ detection. These parameters are all based on the E246 data and can be regarded as very reliable estimates. The reduction of the rates are summarized in Table 24.

8.4 $K_{\mu3}$ event selection

The event selection procedure is essentially the same as in E246. Good $K_{\mu3}$ events are extracted by removing $K_{\pi2}$, $K_{\pi2}$-dif, K_{e3} and $K_{\mu2}$. Although the trigger condition rejects a large fraction of $K_{\pi2}$ and $K_{\mu2}$, a small fraction is still admixed because the momentum look-up decision in the trigger is performed only very loosely. In contrast to E246 only π^0 events which are detected as two photons will be analyzed since they have better kinematical resolution than the one photon events. This is essential to suppress the $K_{\pi2}$-dif contamination to a lower level than E246. The rejection characteristics in terms of the back-to-back condition is schematically shown in Fig. 35.

The selection of $K_{\mu3}$ events is done in a straightforward way, as in E246. K_{e3} positrons are identified by TOF and rejected. In the tracking analysis μ^+ events in the proper momentum range of less than the $K_{\pi2}$ peak with a good χ^2 value in the track fitting are

Table 25: Summary of $K_{\mu 3}$ event selection

	Parameter	Removed background
μ^+	TOF	K_{e3}
	p (momentum)	$K_{\pi 2}$, $K_{\mu 2}$
	χ^2	$K_{\pi 2}$-dif
π^0	$M_{\gamma\gamma}$	accidentals
	$E_{\gamma\gamma}$	accidentals
	$\theta_{\gamma\gamma}$	accidentals
$K_{\mu 3}$ kinematics	M_{miss}	K^+ decay in flight
	t_K	K^+ decay in flight

accepted. The χ^2 cut is essential to reject the $K_{\pi 2}$-dif background, which was not optimally done in E246. The new tracking system must be powerful in this regard. When combined with the above mentioned kinematical cut, the most dangerous contamination of $K_{\pi 2}$-dif will be suppressed below the level of 10^{-3}. The selection of good π^0s from $K_{\mu 3}$ in the CsI(Tl) analysis is performed applying cuts on (1) two photon invariant mass, $M_{\gamma\gamma}$, (2) two photon energy sum, $E_{\gamma\gamma}$ and (3) two photon opening angle, $\theta_{\gamma\gamma}$. Here, it is intended to remove background associated with accidental hits in the CsI(Tl) by background photons and charged particles. Further rejection of backgrounds will be achieved using a kinematical condition of missing mass, M_{miss}. The rejection of K^+ decay in flight events is also done by this cut as well as the rejection of an early part of the K^+ decay time spectrum. The outline of the event selection is summarized in Table 25.

8.5   Controls of systematics during the run

Data taking will be performed under the trigger condition described above. However, several special runs are required to check the systematics including the calibration runs mentioned elsewhere.

- In order to study the accidental rates and the hit patterns in the CsI(Tl) barrel, a run with a trigger condition without CsI is required. This trigger condition might be a mixed trigger in the main trigger run as in E246. $K_{\mu 2}$ events are selected in the charged particle spectrum. The CsI(Tl) response represents accidental background characteristics of the CsI(Tl) barrel. Although the fraction of $K_{\mu 2}$ is small at the spectrometer magnetic field excitation which is optimum for $K_{\mu 3}$, it is essential to take data at the same field condition. The momentum look-up condition in the trigger is removed. This control run is performed every time when the beam condition becomes different because it might result in a different background pattern in the CsI(Tl).

- For the alignment calibration of the polarimeter and magnetic field, a longitudinal polarization (P_L) measurement is necessary. Since the change of the spectrometer field strength might affect the muon field, it is desirable to perform this measurement at the same field as the main measurement. On the other hand it is necessary to realize a $K_{\mu 2}$ muon stopping distribution in the stopper which should not be much

Table 26: Summary of necessary control runs

Special run	Purpose	Trigger condition	Field strength
$K_{\mu 2}$	CsI accidental hit study	w.o. CsI	0.9T
$K_{\mu 2}$	Pol. alignment	w.o. p-look-up and CsI	≥ 0.9T
$K_{\pi 2} - dif$	Pol. alignment	w.o. p-look-up	0.9 T

different from the $K_{\mu 3}$ muon distribution, or from the total stopper volume. Thus, some measurements are required with an increased magnetic field. The beam rate has to be reduced for such measurements.

- For the alignment calibration $K_{\pi 2}$-dif events are employed. A run with the look-up-momentum condition removed is necessary. The field strength is kept the same but the beam intensity has to be reduced. In order to select those events an additional condition might be added to the CsI(Tl) detection as well as to the kinematic relation.

8.6 Polarimeter analysis

The introduction of the active polarimeter enables a polarization analysis with higher analyzing power than in the case of the passive polarimeter as in E246. We consider two methods of 1) event-by-event analysis and 2) π^0 integral method. The sensitivity is higher for the former but it involves the systematics which are not relevant in the latter. There are two further choices with regards to the pion angular range in the event-by-event analysis. For both 1) and 2) the energy and angle of the decay e^+ are used.

8.6.1 Event-by-event analysis

In this method a decay plane is defined for each event with its normal vector as $\mathbf{n}'_i = \mathbf{p}_{\mu^+} \times \mathbf{p}_{\pi^0}$ which is transported to $\mathbf{n}_i(0)$ in the polarimeter coordinate system. We look for the polarization component along this normal vector $\mathbf{n}^i(0)$. For the events with the π^0 going exactly in the fwd or bwd directions, this $\mathbf{n}^i(0)$ is in the azimuthal direction, ie., in the direction of the magnetic field. In general, it undergoes precession due to the field resulting in a different direction $\mathbf{n}^i(t)$ at the time t of decay. By using the e^+ emission angle $\theta^i_{e^+}(t)$ relative to this normal axis (defined as $\cos \theta^i_{e^+} = \mathbf{n}^i(t) \cdot \mathbf{n}_{e^+}$), the transverse polarization is deduced as

$$P_T = \frac{3}{N} \sum_{i=1}^{N} \frac{\cos \theta^i_{e^+}}{\alpha(E_i)}. \tag{32}$$

Here, $\alpha(E)$ is the energy dependent asymmetry function defined as $\alpha(E) = \frac{D(E)}{C(E)}$, where $C(E)$ and $D(E)$ are the isotropic and anisotropic parts of the Michel spectrum, respectively[10]. Namely, $C(E) = x^2(3 - 2x)$ and $D(E) = x^2(2x - 1)$ with $x = E_{e^+}/E^{max}$. In the present analysis with the use of an active polarimeter we can apply this theoretical

---

[10]This expression is extracted from the evaluation of the average value of $\cos \theta_{e^+}$ for the decay angular distribution function of $W(E, \theta_{e^+}) \sim \{1 + P\alpha(E) \cos \theta_{e^+}\}$

function for $\alpha(E)$ in contrast to the passive polarimeter case of E246 where an empirical value for the energy-integrated α had to be used.

Even though the P_T derives finite contributions from the low energy part ($x < 0.5$), we will use only the higher energy part ($x > 0.5$) which has a positive asymmetry and a large yield fraction. Then the average analyzing power is $< \alpha >= 0.436^{11}$. This value is not directly comparable to the average analyzing power 0.270 in the integral method, since the accepted θ_{e+} regions are different. If we confine the accepted range of θ_{e+} in Eq. 32, the average analyzing power $< \alpha >$ is larger than 0.436 but there is a loss of events. There is an optimum boundary for θ_{e+} to maximize the sensitivity. The main features of this method are summarized below.

- The π^0 direction is not restricted to fwd and bwd regions but all the π^0 are analyzed on an equal footing including the $left$ and $right$ going π^0s yielding an increase in the number of events resulting in a higher sensitivity.

- The $left$ and $right$ events are, however, subject to full precession in the perpendicular field. Not only the angular accuracy of the field map, but also the absolute value of the field strength relevant to the spin precession phase become important. Although the field inaccuracy does not induce the admixture of the P_L and P_N components when subtracted $left$ and $right$, it is preferable to avoid dephasing during the muon lifetime. For tolerable dephasing of 0.1 rad during 2.2μs, field accuracies of 0.5 Gauss are required.

- If we consider the chamber structure which is not optimum for detecting e^+ emission near the $r - z$ plane, the $left$ and $right$ events might be accompanied by relatively large uncertainties in determining E_{e+} and θ_{e+}, resulting also in some additional systematic errors.

These considerations might make it preferable to restrict the π^0 selection to fwd and bwd regions at the expense of some statistical sensitivity.

8.6.2 π^0 integral method

The other method which is less affected by the uncertainty of the magnetic field, if any, and by the non-uniform chamber performance with regard to e^+ emission angle, is the π^0 integral method. This method as in E246 deals with the P_T projected component in the stopper in the azimuthal direction, parallel to the field and perpendicular to the chamber plates. Only the fwd and bwd regions are used in the analysis. The projected P_T is deduced with Eq. 32 as in the event-by-event analysis, but θ_{e+} is measured in the polarimeter coordinate as the angle relative to the azimuthal direction, namely the y direction. The real P_T is obtained by correcting for the attenuation of the projection by calculating the attenuation coefficient $< \cos \theta_T >$ as in E246,

$$P_T = P_T^{proj} / < \cos \theta_T > \tag{33}$$

The sensitivity is slightly inferior to the event-by-event method and the symmetric distributions of the π^0s in both the fwd and bwd regions have to be checked in detail. If the

---

[11]This value is calculated as $< \alpha >= \int_{1/2}^{1} C(E)dx / \int_{1/2}^{1} D(E)dx$.

Figure 36: P_T measurement in the polarimeter. The *fwd-bwd* scheme and *left-right* scheme are shown.

influence of "decay plane rotation" is found to be significant, it would be corrected. The great advantage is, however, that one can perform an analysis without worrying about the spin precession. The optimization of the e^+ angular range to a certain value is also effectively done relative to the chamber plate normal vector.

8.6.3 Sensitivity coefficient

The statistical sensitivity can be estimated from Eq. 32 in which P_T is a weighted average of

$$P_T(E) = 3 < \cos\theta_{e^+} >_E /\alpha(E). \tag{34}$$

Its statistical fluctuation is evaluated as $\delta P_T(E) = 3\sigma_{\cos\theta_{e^+}}/\alpha(E)/\sqrt{n(E)}$ since $\sigma_{<\cos\theta_{e^+}>_E} = \sigma_{\cos\theta_{e^+}}/\sqrt{n(E)}$[12], where $n(E)$ is the number of events in the relevant energy bin. A weighted average from $x = 1/2$ to $x = 1$ yields a one standard deviation error of

$$\delta P_T = 3.73/\sqrt{N} \tag{35}$$

where N is the total number of good events used for the analysis. In the case where only fwd and bwd regions are analyzed, N is about 30% of the total $K_{\mu 3}$ good events with e^+s detected. If we expand the energy region down to $x = 0$, the error becomes slightly smaller and $\delta P_T = 3.68/\sqrt{N}$. For the integral analysis the P_T attenuation degrades Eq. 35 to $\delta P_T = 3.73/\sqrt{N}/< \cos\theta_T >$. Since $< \cos\theta_T >$ values for fwd and bwd should not be much different from those in E246, we take its typical value of 0.75 obtaining $\delta P_T = 4.97/\sqrt{N}$. This sensitivity coefficient is compared to that of E246 which was $\delta P_T = 7.9/\sqrt{N}$[13]. Thus, we see a significant increase in the analyzing power.

---

[12]Here one sees the figure of merit to maximize when angular bound is set.
[13]This statistical error is for the total E246 data including 1γ events for which $< \cos\theta_T >$ is smaller than for 2γ events (~ 0.65).

9 Estimated sensitivity of the experiment

9.1 Statistical error

For a conservative estimate we assume the sensitivity coefficient for the integral analysis taking the fwd and bwd regions of the π^0 events. Several comments are presented for the other parameters.

1. The beam intensity at the K0.8 channel is assumed to be 3×10^6/s. Although it is stated that some beam commissioning period with a low accelerator beam intensity is necessary, our total beam request is 1.0×10^7 s of beam time with this kaon beam intensity. We estimate the sensitivity based on the total number of kaons of 3×10^{13}.

2. The fraction of fwd and bwd regions is 30% of the total good $K_{\mu3}$ events including the $left$ and $right$ regions. It is somewhat difficult to estimate the analysis efficiency as it strongly depends on many details. However, at least for now, we can assume that it would be better than what we attained in E246. Below, we use a conservative estimate of 0.67, the E246 efficiency.

The deduction of the statistical error is summarized in Table 27. Thus, a 13 times better statistical error of $\delta P_T = 1.8 \times 10^{-4}$ will be obtained from a one year (10^7 s) run. Event-by-event analysis of the same data will provide a smaller error of 1.35×10^{-4}. A more ambitious analysis including the $left$ and $right$ regions in the event-by-event analysis should attain the highest sensitivity of $\delta P_T = 0.8 \times 10^{-4}$ although the systematic errors have yet to be investigated carefully in this case.

9.2 Systematic errors

As mentioned before the main sources of systematic errors in E246 must be suppressed substantially at least by one order of magnitude. The following observations are in order.

- The effects of polarimeter misalignments, in particular the field rotation δ_z, are all calibrated using data and will be corrected for. These corrections rely on fitting the data to a theoretical fit function, which is subject to fitting errors. Monte Carlo studies to estimate these errors are in progress. Artificial rotations of the order of several times 10^{-4} are introduced into the rotation parameters ϵ_r, ϵ_z, δ_r and δ_z,

Table 27: Deduction of statistical error

Parameter	Value
Net run time	1.0×10^7 s
Proton beam intensity	9μA on T1 target
K^+ beam intensity	3×10^6/s
Total number of good $K_{\mu3}$	2.4×10^9
Total number of fwd and bwd (N)	7.2×10^8
Sensitivity coefficient	$3.73\sqrt{N}$
δP_T	1.35×10^{-4}

Table 28: Expectation of systematic error suppression

Source	Error of P_T (10^{-4})	Confirmation
δ_z	< 1	MC simulation
δ_r	$\ll 1$	MC simulation
ϵ_z	< 1	MC simulation
ϵ_r	$\ll 1$	MC simulation
θ_z	< 1	MC and data symmetrization
θ_r	$\ll 1$	MC and data symmetrization
θ_{e^+}, E_{e^+} analysis	< 1	MC simulation
Total	$\sim 10^{-4}$	

which are then re-extracted from a fit to the MC data. The discrepancy between the fit value and the input value can be regarded a proper estimate of the systematic error associated with the corrections.

- The influence of decay phase space distortion parameterized by the decay plane angular parameters θ_r and θ_z should be corrected. These corrections are estimated as above, ie., one introduces an artificial asymmetry in, for example, the kaon stopping distribution in the target and fits the data with the theoretical function. If the errors are large, one might use a partial data set of acceptable beam stopping distribution, by discarding some, otherwise, good events.

- There is a new potential source of error which was not present in E246, namely the errors coming from the active polarimeter analysis. Although they are believed to be small, the effects of E_{e^+} and θ_{e^+} ambiguities have to be investigated in a MC study. The ambiguity of the decay plane determination also has to be checked in the case of event-by-event analysis taking into account possible local misalignments of CsI(Tl) modules in the barrel.

Other potential sources such as the misalignments of the tracking elements are regarded as rather harmless since the correction based on the alignment calibration described in Section 8 can be done accurately enough. Although the necessary MC studies are not yet finished we strongly believe that each correction is applied with an uncertainty of less than 10% of the correction values and that the total systematic error can be made as small as 10^{-4}. These expectations are summarized in Table 28.

10 Cost estimate and schedule

10.1 Cost of the experiment

The cost of the proposed experiment can be estimated only with a large uncertainty at the moment. Details of the detector elements have yet to be designed and finalized. Thus, the breakdown of the cost estimate in Table 29 is not based on actual estimates from suppliers but largely relying on our experience in E246 and other experiments except for several items such as the GEM chamber production, for which the estimate is based on a detailed sum. On the average the total sum estimate is regarded only 30 to 40% accurate. Regarding manpower and contingency, they are not included in the table at this moment.

The construction of the K0.8 branch of the K1.1 beamline is included in the table just for reference. This is regarded not to be included in the experiment cost but belongs to the facility construction. The main components are one bending magnet and two quads. Including a vacuum system, collimators, additional radiation shielding and a channel switching mechanism between K1.1 and K0.8, a rough estimate is 50,000 kYen. Regarding the transfer of the superconducting Toroidal Spectrometer system, which amounts to the largest item in the table, we request that it be done as a basic facility equipment of the Hadron Experimental Facility for general use along with SKS.

In conclusion, we quote two different estimates.

1) **Cost of the experiment : 273,000 kYen** [14]

2) **Cost including the spectrometer transfer : 455,000 kYen**

10.2 Funding

The proposed experiment has not yet been funded. After obtaining scientific approval, R&D's of detector elements can be started by applying for budgets of moderate size in each country. The main part of the experiment, however, has to be supported by the J-PARC operation budget.

10.3 Time schedule

The time schedule is of course very dependent on the funding of the experiment. Considering the urgency of the physics of this experiment, however, we would like to realize our experiment in the early stage of Phase 1 of the Hadron Experimental Facility. Once the T1 target is brought into operation, the K0.8 beam can be extracted simultaneously with the K1.8 and K_L beams, i.e., three experiments will be able to run beam-economically. As for the beam intensity under this condition, the current design of the experiment is nearly optimized for that.

Since the performance of the detector is already known and the systematics are well studied we believe that it won't take long a time to start data acquisition once the detector

---

[14]The production of GEM chambers are carried out at MIT. The cost estimate for manpower and for development was done but not included here.

Table 29: Breakdown of cost estimate

Item	Cost (kYen)	Comment
K0.8 branch line	50,000	B3, QQ, collimators etc.
Transfer of SC magnet	25,000	
Transfer of cryogenics	157,000	CES from the company
Muon field magnet	35,000	12 units incl. support etc.
Power supply	3,000	10 kW highly stabilized
Cooling system	4,000	piping etc.
Polarimeter	48,000	incl. MWDC and supports gas system
Target	20,000	
Tracking		
C0	13,000	one set (no manpower included)
C1	20,000	12 sets (no manpower included)
CsI(Tl) readout	25,000	incl. R&D
Trigger system	5,000	
Electronics and DAQ	60,000	KEK-VME, FADC, TDC etc.
Field measurement	15,000	new scanning device
μSR measurements	5,000	stopper material search
Others	20,000	
Total	273,000	

is set up. The preparation and upgrade of the detector need a few years. This will be carried out efficiently with international cooperation. A desired time schedule is shown in Table 30. We plan an engineering run in early 2010 and the main data acquisition runs in 2010 and 2011.

Table 30: Proposed time schedule of the experiment

Year (JFY)	Construction Experiment	Other conditions
2006	1) Detector design	PAC decision
	2) Start of budget application	
	3) Formation of collaboration	
2007	1) Detector element R&D	Completion of the hall
	2) Muon field magnet and mapping	
	3) Construction of C0 prototype	
	4) Modification of CsI(Tl) readout	
2008	1) Transfer of the Toroid and He refrigerator	Start of J-PARC exp. budget
	2) Installation of K1.1 and K0.8 branch	
	3) Production of C0 and C1	
	4) Production of Target and Polarimeter	
2009	1) Setup of the spectrometer	
	2) Field mapping	
	3) Detector setup	
	4) Beam tuning	
2010	1) Engineering run	
	2) Data taking	Full intensity from Acc.?
2011	1) Data taking	
2012	1) Analysis	

11 Manpower and international collaboration

The experiment will be performed by an international collaboration as E246.

- The Canadian group played a very active role in the E246 and the subsequent E470 experiments. They involved Canadian students and were also involved with projects of students from other countries. They are playing a much bigger role in the J-PARC experiment. Currently, there are members from TRIUMF, UBC, Saskatchewan and the University of Montreal involved in this project. Prof. Chary Rangacharyulu is the foreign co-spokesperson of this project and he is actively recruiting collaborators from Canada and the USA. Dr. Jaap Doornbos designed the K0.8 beam for this experiment. The Canadian are planning to take on the following responsibilities for the new experimental upgrade. First, they would approach their granting agencies for some funds to construct the K0.8 beam line portion. Also, they will assume responsibility for the new scintillating target. They will collaborate with MIT and

other groups in the development of the new GEM detectors. They will also actively recruit graduate students to work on this exciting project.

- The MIT group will take the responsibility for the improvement of the charged particle tracking by producing the C0 and C1 chambers. The availability and fabrication of GEM foils is making good progress. A first planar GEM prototype already exists and is working very well. During this next year, a light planar prototype which is applicable to both the STAR and C1 detector layout will be designed and built. The design and construction of a prototype C0 chamber is envisioned to be started in 2007. The studies on the cylindrical prototype C0 chamber will be pursued in parallel with the development of the low mass planar element. The design and construction of the final C0 and C1 chambers are envisioned for 2008. The available manpower of the GEM R&D group at MIT consists of Professor Dr. Richard Milner (Principal Investigator), Assistant-Professor Dr. Bernd Surrow (Group leader GEM R&D), Principal Research Scientist Dr. Douglas Hasell, Research Scientist Dr. Michael Kohl, Mechanical Engineer Jim Kelsey, Electronic Engineer Dr. Miro Plesko, Postdoctoral Associate Dr. Frank Simon, and students.

- Regarding other parts of detector upgrades there is no concrete plan yet about the responsibility distribution. At the moment, however, the University Osaka people are working on the analysis of the polarimeter systematics and they can continue further to construct the active polarimeter. The Tohoku University group will be responsible for the upgrade of CsI(Tl) readout together with the NDA people in Japan. The transfer of the spectrometer, production of a new muon field magnet, installation of the K0.8 branch and the assembly of the total setup will be undertaken under the supervision of KEK staff in the group. The construction of the data taking system including the KEK-VME and COPPER preparation will be done most efficiently also by the KEK participants. The participants from other institutions and universities will be organized into the construction team, as soon as the experiment receives approval.

- Considering the efficiency to start up the R&D's and the detector upgrade, Professor J. Imazato of KEK will play the part of **spokesperson** in the construction phase of the experiment. After getting it started smoothly in a few years, the role of spokesperson will be taken over by a group outside KEK. Professor C. Rangacharyulu from Canada is **co-spokesperson**.

Table 31: International cooperation

Country	Institution	Responsibility
Canada	U.Saskatchewan, UBC, TRIUMF U.Montreal	Target etc.
U.S.A.	MIT, U.South Carolina	Chambers (C0 and C1)
Japan	Osaka U., Tohoku U., NDA, KEK	Polarimeter, CsI-readout, Magnet, etc.

12   Summary

In summary, we propose to perform a high precision measurement of the transverse polarization of muons in the $K_{\mu3}^{+}$ decays, which constitutes a T-odd observable. This observable is one of the few tests of T-invariance and the corresponding CP violation in non-neutral meson sector and is sensitive to direct CP violation. We aim to improve the precision of this measurement by a factor of 20 compared to the best result from our own KEK-PS-E246, and reach a limit of $\delta \sim 10^{-4}$.

It is pointed out that the improved sensitivity will be achieved thanks to the new J-PARC facility beam qualities, namely, the newly designed low-momentum (800 MeV/c) K^{+} beamline along with the upgraded E-246 setup. The major upgrades are:

- A slimmer target of finer segmentation,

- Improved charged particle tracking by additional tracking elements using state-of-the-art GEM detectors,

- vastly improved figure of merit for polarization analysis by employing active polarimeters and new muon field magnets,

- Modern electronics and readout systems to handle the higher event rates, and

- Faster readout of Cs(Tl) calorimeter.

Based on our long experience with the E246 setup, and the experience of our new collaborators with the new GEM technology, we know that the upgrades are very straightforward.

The FSI contributions in the SM descriptions are significantly smaller than the sensitivity of this type of measurement, however several exotic models inspired by Multi-Higgs mechanism *etc.* allow P_T values within the sensitivity attainable to us. Thus, this experiment is likely to find new sources of CP violation, if any of these models are viable. It will certainly constrain the parameter space of the candidate models. In this regard, the sensitivity of this experiment is comparable or superior to that of the proposed new neutron EDM experiment and other rare decay processes. As our proposal spans the parameter space and it is sensitive to exotic interactions to which the neutral meson sectors and purely hadronic interactions do not cover, our experiment complements and supplements the other searches for new physics.

We have put together an international collaboration with a mixture of the E246 group and new younger generation members from various particle and nuclear physics groups to ensure a successful completion of this project. We propose this experiment for the early stage of J-PARC phase 1 in the Hadron Experimental Hall. Our requests are summarized as follows.

90

Beam channel: A low-momentum stopping K^+ beam is requested. We propose the K0.8 channel with a beam momentum of 0.8 GeV/c. This channel will be installed as a branch of the K1.1 channel which is going to be built for the strangeness nuclear physics program. The K^+ beam intensity should be 3×10^6/s at the proton beam intensity of 9μA on the T1 target. The simultaneous operation with the K1.8 and the K_L beams is possible. The beam duty cycle must be larger than 20% while keeping this average K^+ intensity.

Beam time: We request the time shown in the table.

Table 32: **Requested beam time**

Main measurement	net $T = 10^7$s	at $I_p = 9\mu$A
		(or $T \cdot I_p = 90$As)
Control measurements	$T = 3 \times 10^6$ s at $I_p = 9\mu$A	
Beam tuning and engineering runs	100 days	at not very weak I_p

Funding: We request support for detector construction and for the transfer of the SC Toroid system from the KEK-PS to J-PARC from the operations money.

References

[1] in Perspectives on Higgs Physics II, Advanced Series on Directions in High Energy Physics - Vol 17 (1997) p. 376, Ed. G.I. Kane, World Scientific pub.

[2] I.I. Bigi and A.I. Sanda, "CP Violation", Cambridge University Press (2000).

[3] See, for example, Prologue of [2].

[4] E. Blanke *et al.*, Phys. Rev. Lett. **51**, 355 (1983); P.D. Eversheim *et al.* [TRIC collaboration], TRIC proposals at COSY.

[5] J.H. Christensen *et al.*, Phys. Rev. Lett. **13**, 138 (1964).

[6] K. Abe *et al.* [Belle collaboration], Phys. Rev. Lett. **87**, 091802 (2001);

[7] B. Aubert *et al.* [BABAR collaboration], Phys. Rev. Lett. **87**, 091801 (2001).

[8] G. Lüders, Danske Mat. Fys. Medd. **28**, 5 (1954); Annals of Physics **2**, 1 (1957); W. Pauli, Nuovo Cimento **6**, 204 (1957).

[9] e.g. J.M. Drake *et al.*, Phys. Rev. **C49**, 411 (1994) and references therein.

[10] e.g. B.R. Holstein, p.112 in "Weak Interactions in Nuclei", Princeton University Press (1989) and references therein.

[11] S.M. Barr and W.J. Marciano, "Electric Dipole Moments", p.455 in "CP Violation" ed. C. Jarlskog, World Scientific (1999).

[12] P.K. Kabir, Phys. Rev. **D2**, 540 (1970).

[13] A. Angelopoulos *et al.*, CPLEAR collaboration, Phys. Lett. **B444**, 43 (1998).

[14] A. Alavi-Harati *et al.*, KTeV collaboration, Phys. Rev. Lett. **84**, 408 (2000).

[15] L. Wolfenstein, Phys. Rev. Lett. **83**, 911 (1999); J. Ellis and N.E. Mavromatos, Phys. Rept. **320**, 341 (1999).

[16] J.J. Sakurai, Phys. Rev. **109**, 980 (1957).

[17] S.R. Blatt *et al.*, Phys. Rev. **D27**, 1056 (1983).

[18] M. Abe *et al.* [E246 collaboration], Phys. Rev. Lett. **93**, 131601 (2004)

[19] M. Leurer, Phys. Rev. Lett. **62**, 1967 (1989).

[20] E. Golowich and G. Valencia, Phys. Rev. **D40**, 112 (1989).

[21] P. Harris [EDM collaboration], plemiminary result presented at SUSY-2005, Durham, June 2005.

[22] See, for example, "Big-bang cosmology", p.191 in "Review of Particle Physics", Phys, Lette. **B592**, 1 (2004).

[23] A. Sakharov, in "The Early Universe" by E.W. Klb and M.S. Turner, Frontiers in Physics lecture note series, vol.69 (1989), Addison-Weilet pub.

[24] A. Riotto and M. Trodden, Ann. Rev. Nucl. Part. Sci. **49**, 35 (1999).

[25] M. Dine and A. Kusenko, Rev. Mod. Phys. **76**, 1 (2004).

[26] M. Fukugita and T. Yanagida, Phys. Lett. **174**. 45 (1986).

[27] L. Affleck and M. Dine, Nucl. Phys. **B249**, 361 (1985).

[28] M. Graham, Talk given at "Flavor Physics and CP Violation", April 9-12, 2006, Vancouver.

[29] K. Sakashita, Talk given at "KAON 2005 International Workshop" June, 2005, Chicago.

[30] p.640 in "Review of Particle Physics", Phys. Lett. **592**,1 (2004).

[31] R. Garisto and G. Kane, Phys. Rev. **D44**, 2038 (1991).

[32] G. Bélanger and C.Q. Geng, Phys. Rev. **D44**, 2789 (1991).

[33] W.-F. Chang and J.N. Ng, arXiv:hep-ph/0512334 (2005).

[34] M. Fabbrichesi and F. Vissani, Phys. Rev. **D55**, 5334 (1997).

[35] G.-H. Wu and J.N. Ng, Phys. Lett. **B392**, 93 (1997).

[36] M. Kobayashi, T.-T. Lin, and Y. Okada, Prog. Theor. Phys. **95**, 361 (1995).

[37] G.-H. Wu, K. Kiers and J.N. Ng, Phys. Rev. **D56**, 5413 (1997).

[38] A.I. Sanda, Phys. Rev. **D23**, 2647 (1981); N.G. Deshpande, Phys. Rev. **D23**, 2654 (1981); H.-Y. Cheng, Phys, Rev. **D26**, 143 (1982); H.-Y. Cheng, Phys. Rev. **D34**, 1397 (1986); I.I. Bigi and A.I. Sanda, Phys. Rev. Lett. **58**, 1604 (1987); M. Leurer, Phys. Rev. Lett. **62**, 1967 (1989); H.-Y. Cheng, Phys. Rev. **D42**, 2329 (1990).

[39] B.C. Regan *et al.*, Phys. Rev. Lett. **88**, 071805 (2002).

[40] M.V. Romalis *et al.*, Phys. Rev. Lett. **86**, 2505 (2001).

[41] The EDM collaborations, Proposals at ILL in Grenoble and SNS in U.S.A..

[42] T. Soldner *et al.*, Phys. Lett. **B581**, 49 (2004).

[43] R. Huber *et al.*, Phys. Rev. Lett. **90**, 202301 (2003).

[44] N. Danneberg *et al.*, Phys. Rev. Lett. **94**, 021802 (2005).

[45] K. Inami *et al.*, Phys. Lett. **B551**, 16 (2003).

[46] J.-P. Lee, arXiv:hep-ph/0111184 (2001).

[47] N. Cabibbo and A. Maksymowicz, Phys. Lett. **9**, 352 (1964); *ibid* **11**, 360(E) (1964); *ibid* **14**, 72(E) (1966).

[48] S. Eidelman *et al.* [Particle Data Droup], p.618 in "Review of Particle Physics", Phys. Letters **B592**, 1 (2004).

[49] J.M. Baily *et al.*, JPG **4**, 345 (1978).

[50] R. Escribano and E. Masso, Phis. Lett. **395**, 369 (1997).

[51] A.R. Zhitnitkii, Yad. Fiz. **31**, 1014 (1980).

[52] V.P. Efrosinin *et al.*, Phys.Lett. **B493**, 293 (2000).

[53] Weinberg, 3 Higgs doublet model

[54] K. Ikado, Talk given at "Flavor Physics and CP Violation", April 9-12, 2006, Vancouver.

[55] Y. Grossman, Int. J. Mod. Phys. **A19**, 907 (2004); T. Hurth, Rev. Mod. Phys. **75**, 1159 (2003).

[56] Y. Okada, Y. Shimizu, and M. Tanaka. arXiv:hep-pf/9704223.

[57] V.V. Anisimovsky *et al.* [E246 collaboration], Phys. Letters **B562**, 166 (2003).

[58] D.K. Ghosh, X.-G. He, B.H.J. McKeller and J.-Q. Shi, arXiv:hep-ph/0111106.

[59] K. Young *et al.*, Phys. Rev. Lett. **18**, 806 (1967); J.J. Longo, K.K. Ypung and J.A. Helland, Phys. Rev. **181**, 1808 (1969).

[60] J. Sandweiss *et al.*, Phys. Rev. Lett. **30**, 1002 (1973).

[61] W.M. Morse *et al.*, Phys. Rev. **D21**, 1750 (1980).

[62] K.H. Tanaka *et al.*, Nucl. Instrum. Methods Phys, Res. Sect. **A363**, 114 (1995).

[63] J. Imazato *et al.*, Proc. 11th Int. Conf. on Magnet Technology, August 1989, Tsukuba, Japan.

[64] T. Ikeda *et al.*, Nucl. Instr. and Meth. Phys. Res. Sect. **A401**, 243 (1997).

[65] J.A. Macdonald *et al.*, Nucl. Instrum. and Meth. Phys. Res. Sect. **A506**, 60 (2003).

[66] D.V. Dementyev *et al.*, Nucl. Instrum. and Meth. Phys. Res. Sect. **A440**, 15 (2000).

[67] Yu. G. Kudenko *et al.*, Nucl. Instr. and Meth. Phys. Res. Sect. **A411**, 437 (1998).

[68] A.P Ivashkin *et al.*, Nucl. Instrum. and Meth. Phys. Res. Sect. **A394**, 321 (1997).

[69] M.P. Grigor'ev *et al.*, Instrum. Exp. Tech. **41**, 803 (1998).

[70] M. Abe *et al.*, Phys. Rev. Letters **83**, 4253 (1999).

[71] M. Abe *et al.*, Phys. Rev. **D73**, 072005 (2006),

[72] J.Imazato *et al.* AGS Proposal, "Search for T-violation in the $K^+ \to \pi^0 \mu^+ \nu$ Decay using stopped kaons". (1997).

[73] A. Carrol *et al.* AGS Proposal. "Search for T violating muon polarization in $K^+ \to \mu^+ \pi^0 \nu$ decay', (update in 1998).

[74] Y. Asano *et al.*, J-PARC LOI-19 submitted to J-PARC Nuclear and Particle Physics Program Advisory committee (2003).

[75] V. Rykalin, Frascati seminar Oct 26/04.

[76] Y. Kudenko – private communication.

[77] Hamamatsu Photonics K.K., Technical Information SD-28, Oct,2001; Cat.No. KAPD1012J02, April, 2004.

[78] I. Britvitch *et al.*, Nucl. Instrum. and Meth. Phys. Res. Sect. **A535**, 523 (2004).

[79] T. Ikagawa *et al.*, Nucl. Instrum. and Meth. Phys. Res. Sect. **A538**, 640 (2005).

[80] A. Jodidio *et al.*, Phys. Rev. **D34**, 1967 (1986); *ibid* **D37** (E), 237 (1988).

[81] A. Schenck, "Muon Spin Rotation Spectroscopy", p.112, Adam Hilger Ltd (1985),

[82] S. Tanigawa *et al.*, Hyperfine Interactions **17-19**, 235 (1984); **8**, 787 (1981).

[83] R.D. Stambaugh *et al.*, Phys. Rev. Lett. **33**, 568 (1974).

[84] M. Senba, J. Phys. B: At. Mol. Opt. Phys. **31**, 5233 (1998).

[85] J. Doornbos, "An 800 MeV/c separated kaon beam at J-PARC", J-PARC/NP 05-001 (2005).

[86] H. Noumi, "Primary ans Secondary Beam Lines in the Hadron-Beam Line Facility", NP04 (2004), http://www-ps.kek.jp/jhf-np/NP04/presentations/Plenary/NP04-Noumi.pdf.

A Superconducting Toroidal Spectrometer

A.1 Transfer of the Toroidal Spectrometer system

For the proposed experiment we are going to employ the Superconducting Toroidal Spectrometer which has been used for the E246 experiment in the North Hall of KEK-PS. The total system of the magnet and the He refrigerator will be transferred to J-PARC without modification. Because the heat-load to 4.5K amounts to 25 W due to the complicated magnet structure with large surface area, the current cooling scheme using a Claude-cycle cold-box and a medium-size He compressor will be used, although development of a new cryogenic system using a small re-condenser might be within the scope in the future. Hence, the system will be operated further under the regulation of refrigeration rule of high-pressure gas safety law in Japan. The cryogenic system consists of the cold-box, He-gas compressor, two oil separators, a gas buffer tank, pneumatic compressor and a control system. The cold box will be standing by the magnet, the tank outside the building, and the other components will be installed in the cryogenics machine room outside the experimental hall. The facility was designed so as to accommodate this system. One of the features is that this system does not use liquid N_2 also at the magnet pre-cooling stage. Therefore, there is no concern about the strict high-pressure gas regulation in terms of "general gas". The layout of the components is shown in Fig. 37.

In order to move the system from Tsukuba we have to ask for support by the IPNS cryogenics group. The installation and commissioning will be done under their responsibility. As for the operation, however, we will seek a much more sophisticated automated control system than the current control. Routine cooling and steady state operation will be carried out nearly unattended. Without liquid N_2 use and any loss of He gas in the system, the operation will be very reliable.

A.2 Application of the toroidal spectrometer

When the Toroidal Spectrometer is installed at the Hadron Facility, it is possible to study various K^+ decays taking advantage of the versatility of the detector system. At KEK-PS we have performed several exploratory measurements as part of a special calibration run of E246 and also the dedicated E470 measurement as shown in References. Though the data were limited by statistical accuracy due to the low beam intensity, some expertise in K decay physics and tests of Chiral Perturbation Theory inspired models were obtained. The unique features of this spectrometer for universal use can be summarized as follows.

1) As a charged particle analyzer, it has the performance of a sector-dipole spectrometer of 90° bending, although the acceptance is limited. The intrinsic momentum resolution is high.

2) The acceptance for photon detection is as large as 3/4 of 4π with a consequence of high detection efficiency for decays involving π^0 and radiative γ. Although the energy resolution is limited by the presence of the muon holes, one can take advantage of good angular resolution.

3) As a result the spectrometer has relatively large acceptance for multi-particle decays generally, while keeping fairly good kinematical resolution. This is a powerful feature for the spectroscopy of particles with low energy/momentum from K decays at rest.
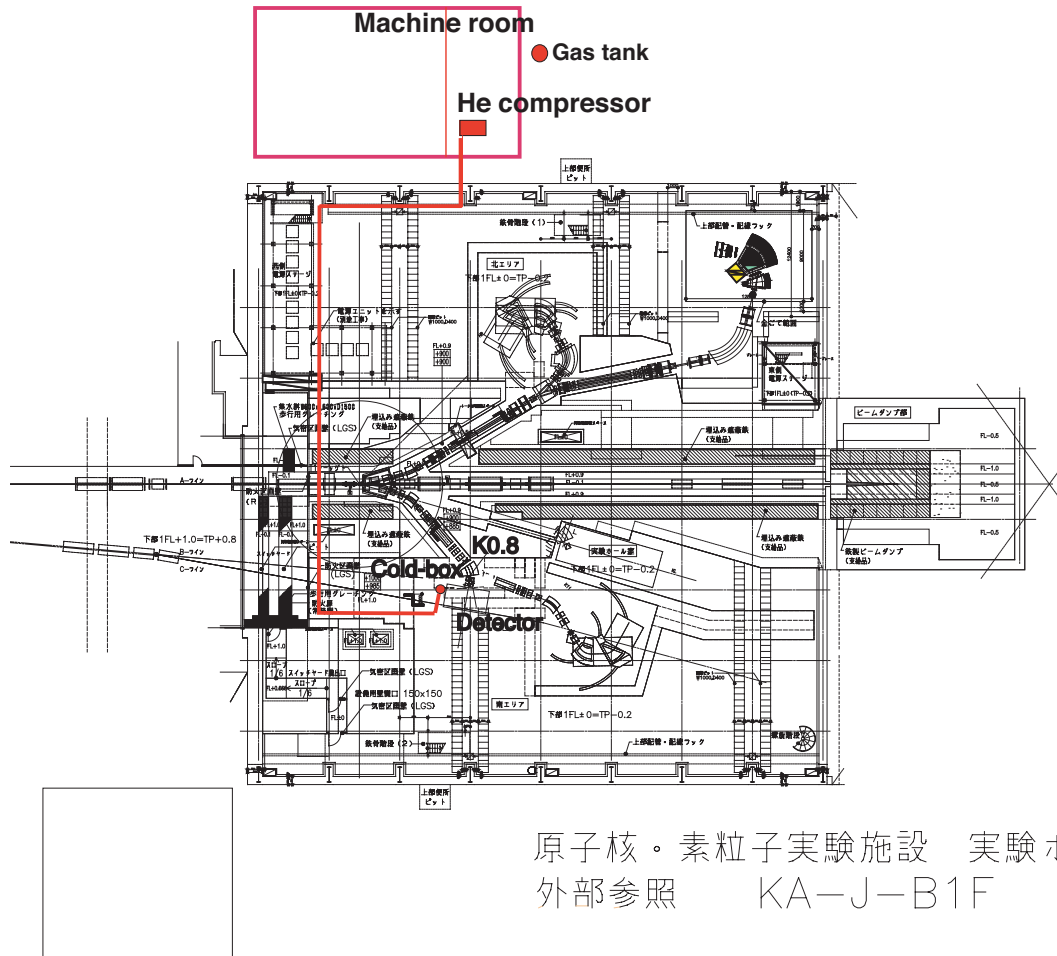
Figure 37: Layout of the superconducting toroidal spectrometer with its cryogenic system in the Hadron Experimental Facility

4) Since the detector symmetry (axial/azimuthal as well as forward/backward symmetry) is well ensured, other experiments than $P_T(K_{\mu3})$ in the quest for symmetry breaking are possible.

By using these advantages it would become possible at J-PARC (1) to explore K decay spectroscopic studies in the mode with smaller branching ratio, which were difficult before, and also (2) to continue previous studies to much higher precision. Among the interesting channels, the following measurements, in particular, are expected to be performed with good statistics.

- Since semileptonic $K^+ \rightarrow \pi^0 l^+ \nu$ (K_{l3}) decay, which simply proceeds via W exchange in the Standard Model, is believed to have only a V−A interaction, exotic interactions, such as scalar and tensor couplings, can be searched for by comparing experimental spectra with the V−A predictions. Disagreement between the experimental results and the calculation directly indicates the existence of exotic interactions beyond the standard model. (see Ref. [1, 2]

- As well as T-violating muon polarization in $K_{\mu 3}$, we will search for another T-violating quantity in the radiative $K^+ \rightarrow \pi^0 l^+ \nu \gamma$ ($K_{l3\gamma}$) decay. Since $K_{l3\gamma}$ is a 4-body decay, it is possible to define T-violating triple correlation such as $\vec{p_\gamma} \cdot (\vec{p_l} \times \vec{p_\pi})$ using 3 independent momentum vectors in the final state. The SM radiative correction due to the electromagnetic final state interaction lead to imaginary form factor parts, predicting a relatively large asymmetry value of $A \sim 10^{-4}$. (See Ref. [7])

- The π-π scattering length can be determined from the $K^+ \rightarrow \pi^+ \pi^0 \pi^0$ and $K^+ \rightarrow \pi^0 \pi^0 l^+ \nu$ decays. An anomaly in the $\pi^0 \pi^0$ invariant mass distribution in the region around $2M_+$ should be observable, where M_+ is the charged pion mass. This anomaly can be interpreted as an effect mainly due to the final state charge exchange scattering process $\pi^+ \pi^- \rightarrow \pi^0 \pi^0$. By fitting the invariant mass spectra, we can determine $a_0 - a_2$, the difference between the S-wave $\pi\pi$ scattering lengths in the isospin $I = 0$ and $I = 2$ states. (See Ref. [6])

- Semi-leptonic and non-leptonic radiative decays, such as $K^+ \rightarrow \pi^+ \pi^0 \gamma$ ($K_{\pi 2\gamma}$), $K_{l3\gamma}$, and $K^+ \rightarrow \pi^+ \gamma \gamma$ ($K_{\pi^+ \gamma\gamma}$), offer a good testing ground for hadron structure models making use of low-energy effective Lagrangian's inspired by Chiral Perturbation Theory (ChPT). The validity of ChPT will be strictly checked by comparing experimental spectra with the ChPT predictions. (See Ref. [5])

References

[1] S. Shimizu *et al.*, Phys. Lett. **B495** 33 (2000).

[2] A.S. Levchenko *et al.*, Phys. At. Nucl. **65**, 2232 (2002).

[3] K. Horie *et al.*, Phys. Lett. **B513**, 31 (2001).

[4] Y.-H. Shin *et al.*, Eur. Phys. J. **C12**, 627. (2000)

[5] M.A. Aliev *et al.*, Phys. Lett. **B554**, 7 (2003).

[6] S. Shimizu *et al.*, Phys. Rev. **D70**, 037101 (2004).

[7] S. Shimizu *et al.*, Phys. Lett. **B633**, 190 (2006).

B Production of GEM chambers C0 and C1

B.1 GEM detector

As outlined in the previous sections, two types of new tracking elements are essential to achieve the goal of a systematic error suppression to $< 10^{-4}$. One element (C0) will be a cylindrical chamber surrounding the target bundle at a small radius of 10 cm. The other element (C1) is proposed to cover the muon holes of the CsI calorimeter and will thus give additional tracking information between the target and the bending magnet. While this provides redundant information for regular tracks, it will allow us to identify kinked tracks from $K_{\pi 2}^+$-dif events and help to determine the kink angle.

The new tracking elements are required to be highly efficient even for minimum ionizing particles, to be capable of running in a high rate environment, to be hard against irradiation (aging), to provide a spatial resolution of better than 0.1 mm, to present low material, and to be producible at low cost. All of these requirements are ideally fulfilled by the concept of Gas-Electron Multiplier (GEM) detectors introduced in 1997 [1]. In the following its principle is briefly described.

Limits in the granularity and rate capability of the MWPC led to the development of micro-pattern gas detectors, beginning with the introduction of the micro-strip gas chamber (MSGC) in 1988. Based on the same principle as the MWPC, the use of photolithographic techniques allowed much finer structures and consequently higher granularity and higher rate capability due to fast positive ion collection. The reduction of performance of MSGCs under sustained irradiation (aging) and damaging discharges induced for example by heavily ionizing particles triggered new developments in the area of micro-pattern gas detectors. One of these is GEM, which consists of a thin metal-clad insulation foil (typically double-sided 5 μm copper on 50 μm kapton) perforated by a regular dense hole pattern [1]. The holes in the foils typically have a double conical shape with an inner diameter of ∼50 μm, an outer diameter of ∼70 μm and a pitch of 140 μm. A voltage difference between the two metal-clad sides of the foils leads to high electric fields in the holes. This field is used to achieve electron multiplication of the charge deposited by the passage of an ionizing particle in the detector gas. The signal is read out on a separate readout surface. Charge transfer from the GEM to the readout is ensured by an electric field. This method has the advantage of a fast (electron only) signal due to fast positive ion collection on the GEM foils and improved discharge tolerance due to a separation of the readout and amplification stage. This separation also allows flexibility in the choice of readout geometries. Improved stability and higher gains in heavily ionizing environments is reached by cascading several GEM foils to achieve the desired gain. Figure 38 displays a schematic view of a single and a double GEM detector.

GEM technology is now widely employed by current and future experiments in nuclear and particle physics. The first experiment to use GEM detectors extensively was the COMPASS experiment at CERN [2], in which a triple GEM design was chosen. A spatial resolution of ∼70 μm, efficiencies in excess of 95% and a time resolution of ∼12 ns are reached in high-rate data taking [3], while at low intensities a resolution of ∼50 μm is reached. In four years of operation no electronics channel was lost. The COMPASS design also shows that GEM detectors can be built with a small material budget, an important feature for precise tracking systems. The overall thickness of the COMPASS GEM is less than 0.75% of a radiation length, with a central area with a thickness of
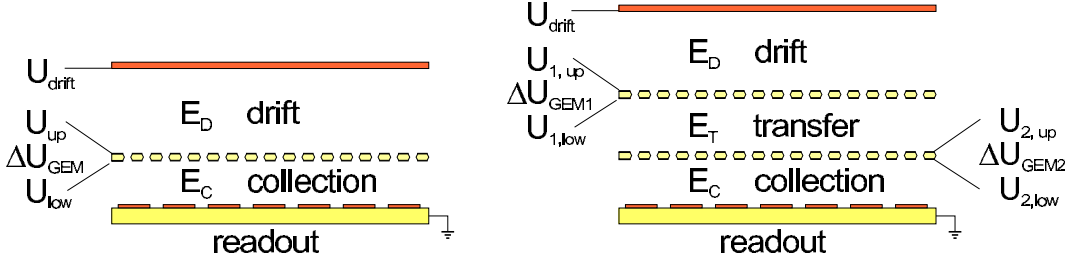
Figure 38: Schematic view of a single (left) and double (right) GEM detector.

~0.5% of a radiation length. A large fraction of that thickness is due to the multiple 5 μm copper layers. A recent study has shown that the detector material can be significantly reduced without affecting the performance by using copper layers of 1 μm instead [4]. More material can be saved if the requirement for rigidity is lower.

B.2   C1 chamber

It is proposed to cover the muon holes of the CsI calorimeter (see Fig. 12) with planar GEM detectors. Individual light-weight double or triple-GEM planar detectors are considered for the design of the new C1 element. The area to be covered for each of the 12 gaps is ~15×45 cm^2. The radial distance of the C1 element will be at ~ 100 cm from the beam axis. The geometry of the CsI muon holes allows for a two-dimensional readout on the sides of the active rectangular regions in the shadow region of the CsI crystals. The existing MIT prototype (presented in the section on R&D below) is already quite close to the design requirements. An important aspect is the light-weight construction with a minimized material budget in the active area. The material budget of the COMPASS design which was mostly adopted for the MIT prototype amounts to 0.7% X_0, however it also offers a lot of potential to significantly reduce the material. The COMPASS chambers are very rigid objects due to the use of fiber glass planes. Such a rigidity is however not required, in particular the active area can be made with very thin carrying and gas-sealing foils. The required resolution of 0.1 mm is easily achievable by adopting the readout pattern of the MIT prototype with a 635 μm pitch for the stereo strip readout and the use of the same DAQ technology based on APV25 chips. Besides using much thinner layers of copper (1 μm instead of 5 μm), the material budget can be further reduced by choosing the double-GEM design instead of three GEM layers. The third GEM layer has mainly the effect of reducing the discharge probability, while enough gain can already be achieved with two GEM layers. Due to the relatively large distance of the C1 element from the target and the subsequently lower density of ionizing particles compared to the region very close to the target, the discharge probability may already be at a tolerable level for a double-GEM element. The C1 material budget for a light double GEM can therefore be reduced to 0.11% of a radiation length. With a 635 μm pitch readout pattern the number of channels amounts to (15 cm + 45 cm) / 635 μm $\simeq$ 1000 per C1 element. Table 9 summarizes the properties of the proposed C1 element.

B.3 C0 chamber

As stated in the previous sections, it is is proposed to develop and build a cylindrical chamber C0 based on GEM technology to surround the target inside the CsI calorimeter. The new C0 chamber will replace the previous C1 chamber of the E246 setup. The main information provided by C0 will be the determination of the vertex position along the target z axis. The vertex information along with the information from the other tracking elements will serve to identify $K^+_{\pi 2}$-dif events. Since the pion decay rate decreases exponentially with increasing distance from the target, the kink locations for the pion decay in flight are predominantly close to the target. Hence, the location (or radius) of the C0 chamber has to be as small as possible. On the other hand, the possible size of any existing beam halo, and a minimum bending radius for the GEM and readout foils for safe operation and easy handling set a lower limit on the radius. Moreover, the use of the C0 chamber as a charged particle veto for the CsI prefers the gap between the C0 and the calorimeter to be as small as possible. For the proposed chamber a radius of 10 cm appears to be an appropriate choice.

To our knowledge, only two projects have so far used GEM technology for cylindrical tracking chambers with curved foils. One chamber (TACTIC) is designed at TRIUMF, Canada, for the measurement of heavy charged recoil fragments in nuclear astrophysics experiments [5]. Another experiment (BoNuS) recently used a GEM-based radial time projection chamber (RTPC) in a solenoidal magnetic field along with the CLAS/Hall B detector at the Thomas Jefferson National Accelerator Facility, USA, to measure spectator protons at very low momenta [6]. At CERN, a cylindrical GEM prototype is being developed for a future NA49 upgrade [7]. While TACTIC is a ionization chamber with a single GEM layer for charge amplification and segmented single anode strip readout, the BoNuS RTPC is a cylindrical triple-GEM chamber with 2D pad readout. The large drift volume of the RTCP enables full reconstruction of the curved tracks in the solenoidal field through radial time projection. Although this detector has been used to track heavily ionizing low-energy protons, it is in principle capable of measuring minimum ionizing particles.

In contrast to the above two examples, the proposed C0 GEM chamber has to meet different requirements. Like the BoNuS chamber it has to be capable of efficient detection of minimum ionizing tracks. The absence of a magnetic field in the target region keeps the tracks very straight and in the radial direction, hence only the (z, ϕ) coordinates of the trajectory crossing through the cylinder surface at a certain radius are of interest. Subsequently, the drift volume can be kept small, which is beneficial for the resulting position and timing resolution of the device.

The most important aspect is the material budget requirement of the C0 chamber. While the particles detected with TACTIC and BoNuS undergo no further tracking and thus do not have to leave the annular chamber, this is not the case for the proposed C0 element. Here, the cylindrical surface including all GEM and readout foils and carrying materials have to be as thin as possible in order to allow the charged particle, mainly the μ^+ from $K^+_{\mu 3}$, to be tracked through the magnet and to reach the muon polarimeter at the focal plane. This requirement also implies that all readout electronics and support structures have to be restricted to the end caps. In order to further reduce the material around the target we propose to use helium as the counting gas and to consider a common

helium-filled volume with fiber target cylinder in the active region. The cylinder will cover the full 2π azimuthal acceptance without blind regions. As such, the individual foil layers will be glued seamlessly to individual cylinders with defined radii that are assembled later in the process.

The readout strips need to be two-dimensional with readout electronics at the end-caps only. This will be achieved by employing spiraling strips in a double layer and opposite helicity of the spiral in each layer. With a spiral phase rotation of $180°$ between the two end-caps it is ensured that all left and right-handed spirals intersect with each other exactly once to give a unique (z, ϕ) information on the cylinder surface. For a cylinder length of $l = 30$ cm and a radius of $r = 10$ cm, the length of the strips will amount to $s = \sqrt{l^2 + (2\pi r/2)^2} \simeq 45$ cm. As such, the crossing angle between strips will be close to $90°$, resulting in a longitudinal position resolution $\sqrt{2}$ times the resolution across the strip orientation. With the same pitch of 635 μm as for the C1 chamber and a resolution of 50-70 μm perpendicular to the strip orientation, a z resolution of better than 0.1 mm can be established. The readout at the cylinder end-caps will be using flexible transient circuit boards to transport and bundle the signal channels to planar circuit boards hosting the readout electronics. The readout of the proposed C0 element will consist of a total of 2 layers $\times (2\pi \cdot 10\text{cm})/(\sqrt{2} \cdot 635\mu\text{m}) \simeq 1400$ channels. Table 8 summarizes the properties of the proposed C0 chamber.

B.4   R&D at MIT

MIT has recently established a GEM laboratory to perform R&D on GEM detectors in the framework of the planned tracking upgrade of the STAR detector at RHIC. We propose to utilize and extend the present R&D activities at MIT with the goal to develop and build the C0 and C1 tracking elements for the proposed experiment. Such a strategy of combining the R&D efforts to enable the application of the same technology in two different experiments, namely at RHIC and at J-PARC, has the great benefit of synergistic effects where expertise and effectiveness can be enhanced.

A prerequisite for mass production of triple GEM tracking detectors is the availability of GEM foils. So far, the only source for these devices has been the CERN-EST-DEM photolithographic workshop. However, their capacity is limited and unable to meet the increasing worldwide demand for GEM foils. To address this problem a collaboration with the Plymouth, MA based company Tech-Etch, Inc. has been formed and a SBIR proposal (Small Business Innovation Research) has been formulated. The goal of the recently approved SBIR proposal by Tech-Etch in collaboration with BNL, MIT and Yale is to develop the technology at Tech-Etch for commercial production of GEM foils which meet the requirement of use in nuclear and particle physics and astrophysics research besides long-term medical imaging and homeland security applications. The focus of Phase I of the SBIR proposal is to determine the role of materials, process and post-process handling. Meanwhile, GEM foils are routinely produced by Tech-Etch. Several prototype chambers have been assembled and are currently being tested using GEM foils by Tech-Etch.

To evaluate GEM foils produced by Tech-Etch and perform research and development work for the STAR GEM tracker a GEM laboratory has been established at MIT and Yale University. An optical scanner was developed to measure the parameters of the foils and to test them for defects [8]. A triple-GEM detector prototype based on 10 cm $\times$ 10 cm GEM
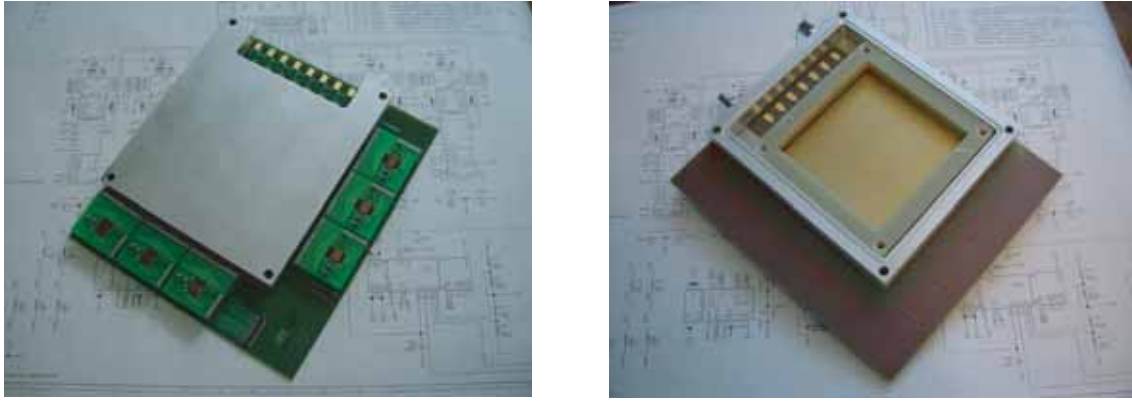
Figure 39: Bottom (left) and top (right) view of the prototype triple-GEM chambers. The location of the sensitive detector volume can be clearly seen on the right side with the location of three inner G10 carrier frames. No GEM foils have yet been glued onto those frames. The location of groups of three readout hybrids can be clearly seen on the left side.

foils has been developed and was tested with foils made at CERN. The prototype has a two dimensional projective strip readout with 635 μm pitch laser-etched onto a printed circuit board, and a gas-tight body made out of aluminum and plastic. The GEM foils are stretched and glued onto frames that guarantee the correct distance between the foils. The high voltage on the foils is provided via a resistor network. The detector is operated with a gas mixture of Ar:CO$_2$ 70:30.

Figure 39 shows a bottom and top view of the prototype triple-GEM chambers. Those chambers have been designed within the R&E laboratory. The location of the sensitive detector volume can be clearly seen on the right side of Fig. 39 with the location of three inner G10 carrier frames. No GEM foils have yet been glued onto those frames. The sensitive GEM foil area amounts to 10×10 cm^2. The bottom of this sensitive volume consists of orthogonal readout strips with a readout pitch of 635 μm. The charge induced on each individual strip is read out by a APV25-S1 readout chip which is glued and bonded onto separate readout hybrids. Each hybrid reads out 64 readout strips providing a total of 192 readout channels for each orthogonal direction (X/Y). The location of groups of three readout hybrids can be clearly seen on the left photograph in Fig. 39.

An exploded view of the triple-GEM chamber design is shown in Fig. 40. Each chamber consists of a 2D readout board which is based on a conventional printed circuit board. The 2D readout strip structure is glued on one side onto each 2D readout board. The actual triple-GEM chamber is then built up on top of this strip readout structure. The figure is the schematic view of the chamber as shown on the right side in Fig. 39. The connection of each readout strip to the back side which is shown on the left side in Fig. 39 is provided through VIAS connections. Those are then connected to individual readout hybrids combining 64 readout strips onto one readout hybrid.

A readout system based on NIM and CAMAC electronics connected to a standard PC has been set up to read out groups of channels. The detector was irradiated in different positions with a collimated ^{55}Fe source emitting 5.9 keV X-rays to determine the relative gain variations over the active area. The quality of the X-ray spectrum is used as an
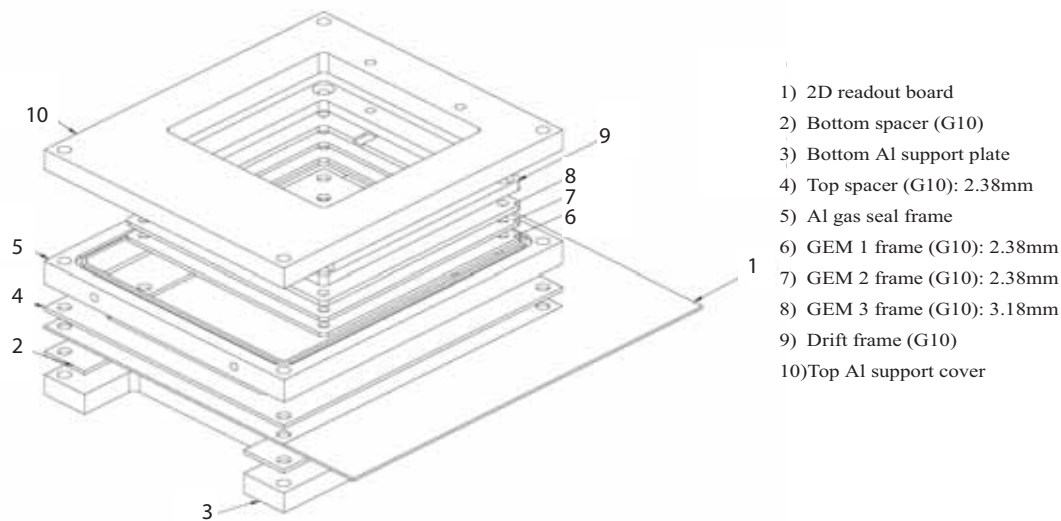
Figure 40: Exploded view of a prototype triple-GEM chamber indicating the location of various chamber elements.

1) 2D readout board
2) Bottom spacer (G10)
3) Bottom Al support plate
4) Top spacer (G10): 2.38mm
5) Al gas seal frame
6) GEM 1 frame (G10): 2.38mm
7) GEM 2 frame (G10): 2.38mm
8) GEM 3 frame (G10): 3.18mm
9) Drift frame (G10)
10) Top Al support cover

indicator of the overall detector quality. Figure 41 shows a spectrum recorded with the CERN foil based triple GEM prototype. The quality of the spectrum and the energy resolution is comparable to that obtained with the COMPASS triple GEM detectors [2].
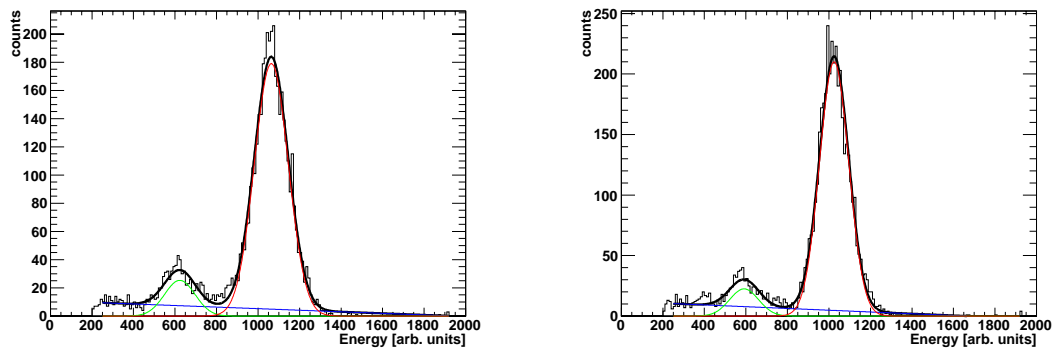

Figure 41: ^{55}Fe spectrum recorded with a triple GEM prototype based on CERN foils for top (left) and bottom (right) strip readout. The full-energy photo peak and the argon escape peak are cleanly separated. The spectrum is fitted with two Gaussians and a linear background. The energy resolution of the photo peak is ∼20%, given by the FWHM of the peak.

A collaboration between Tech-Etch, MIT, Yale and BNL has been established to work on the optimization of the GEM foils produced by Tech-Etch. Foils produced under a variety of conditions using different materials will be tested at the institutions to determine their properties, thus identifying optimal conditions and materials for the final product.

In parallel, research and development will be done to develop a low mass detector

prototype that can be used in beam tests which meets the requirements of a minimized material budget for both the STAR Forward GEM Tracker (FGT) arrangement and the C1 tracking element in the proposed experiment. While the C1 element and the GEM trackers for STAR are both planar detectors and have many common requirements. the development of the C0 chamber will significantly extend the R&D activities at the MIT GEM lab.

B.5   Readout system

The readout system for both the intermediate and forward tracking systems at STAR are based on the APV25-S1 readout chip. For the prototype the same APV25-S1 based system has been adopted. The following section describes the design of a complete APV25-S1 chip readout system as part of the triple-GEM prototype setup.

Data from the 2D triple-GEM detectors are read out by the APV25-S1 readout system which consists of the following components:

- Signal Boards
- APV Module
- GEM Control Unit

A sketch of the APV25-S1 chip readout system is shown in Figure 42. Each signal board is fabricated from FR4 as a regular double sided 62 mil PC (Printed Circuits) board which has a 2 mil thick Kapton foil glued on top which in turn is covered by 5 μm thick and 20 mil wide sensor strips on the bottom and 5 μm thick and 5 mil wide sensor strips on the top side. The kapton material between the top strips is removed by laser etching to uncover the bottom strips which are then gold plated. The signal strips have a 12.5 mil pitch. The top strips are perpendicular to the bottom strips to form a two-dimensional readout board. Each signal strip is connected to the bottom side of the signal board through VIAS connections and to 25 mil pitch SAMTEC connectors. Those provide the connections to the APV module. There are two sets of SAMTEC connectors, one for the X and one for the Y direction. The signal board also has two sets of an integrated bus system as part of the communication and data collection between the APV module and GEM control unit.

The APV module in the prototype version has an on-board glued APV25-S1 chip which is fabricated using a submicron process (0.250 micron) and is connected to 68 sensor channels. There is one set of APV modules for the X-direction and a separate set for the Y-Dimension. In the prototype version of the APV modules, each APV module is connected to 68 channels. In the final version each APV module will be connected to 128 channels and will have an ADC and a FIFO on board. The length of the data acquisition path will be less then 5 mm, which will guarantee minimum pickup noise. In our case, the APV25-S1 chip is operated with a clock frequency of 40 MHz and read out at 20 MHz. The APV25-S1 chip is set up using the I2C Philips Standard. Calibration pulses can be generated directly onboard to feed each channel.

The GEM Control Unit is the main control system for the 2D GEM readout electronics which controls all ADC, FIFO, and Data formatting and keeps communication between APV25 Modules and DAQ system. A Xilinx CPLD is the heart of each GEM Control Unit. This Xilinx component is fabricated in very deep submicron process (0.095 micron).
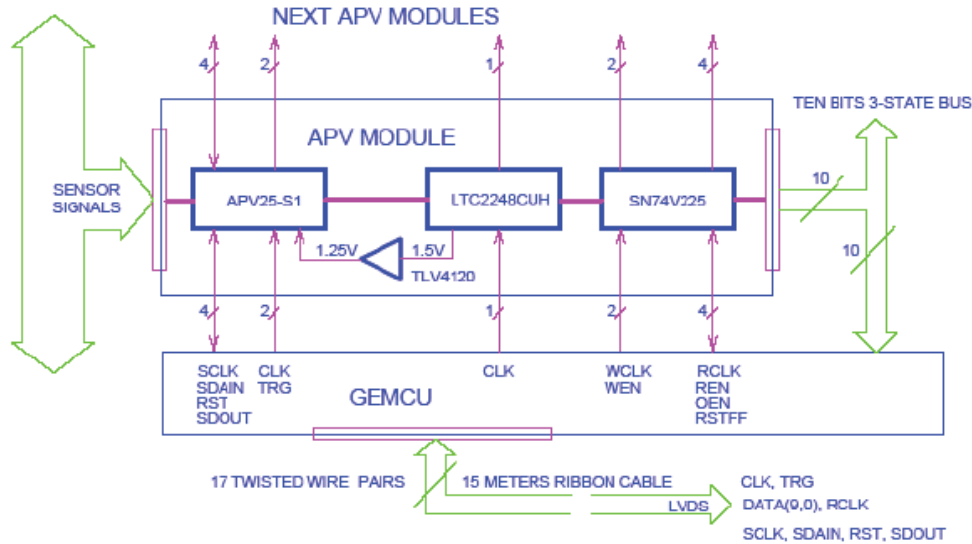
Figure 42: Sketch of the APV25 chip readout system.

In radiation tests which were carried out at Bates Linear Accelerator Laboratory, it was found that radiation hardness of the Xilinx CPLD component is beyond 1MRad. The advantage of the Xilinx CPLD is based on its flexibility for re-programming it to any desired configuration. Each GEM Control Unit contains for each APV25-S1 an ADC and a FIFO, where the ADC is continuously running and converting incoming signals from the APV25-S1. Upon a positive trigger decision, the data are then converted and written in parallel into all FIFOs and then these data are sent out in sequence in LVDS standard to the DAQ system. These actions are controlled by the Xilinx CPLD device which is programmed in VHDL language. The GEM Control Unit is connected with the outside environment only through one twenty wire pair flat ribbon cable. Each GEM Control Unit has all required voltage regulators on board. The power distribution requires therefore only one +4V power supply using one wire pair.

The signal board, APV25 module and GEM control unit form one compact unit without cables and wires. All connections are realized through PC board printed layer connections. This guarantees that this system will have very low noise.

References

[1] F. Sauli, Nucl. Instr. and Meth. **A386** (1997) 531

[2] C. Altunbas et al., Nucl. Instr. and Meth. **A490** (2002) 177

[3] B. Ketzer et al., Nucl. Instr. and Meth. **A535** (2004) 314

[4] A. Bondar et al., Nucl. Instr. and Meth. **A556** (2006) 495

[5] http://tactic.triumf.ca/

[6] http://www.jlab.org/%7Ehcf/bonus/

[7] http://gdd.web.cern.ch/GDD/

[8] U. Becker et al., Nucl. Instr. and Meth. **A556** (2006) 527